

# Optimal Estimation Method retrievals with IASI, AMSU and MHS measurements

Final Report

Version 5.2



*Prepared by*

*RAL Space*

*Remote Sensing Group*

*Harwell Oxford*

*Chilton, OX11 0QX*

*United Kingdom*

*Eumetsat Contract  
EUM/CO/13/460000125  
2/THH*

*2015-01-29*



RAL Space  
STFC Rutherford Appleton Laboratory  
Harwell Oxford  
Chilton, OX11 0QX, United Kingdom

Document:	Final Report
Customer Ref:	ITT 13/207194
RAL Space Ref:	SSTD1569
2015-01-29	Page 1 of 120

## CONTENTS

Acronyms Used in this Document.....	5
Document Revision History.....	6
1 Overview.....	7
1.1 The ATOVS instrument suite.....	8
1.2 AMSU-A.....	8
1.2.1 Technical description and spectral characteristics.....	8
1.2.2 Scanning geometry.....	9
1.2.3 Instrument calibration.....	10
1.3 MHS.....	10
1.3.1 Technical description and spectral characteristics.....	10
1.3.2 Scanning geometry.....	11
1.3.3 Instrument calibration.....	12
2 Algorithm Technical Description and Methodology.....	13
2.1 Operational IASI processor at Eumetsat.....	13
2.2 Background term of the cost function, $\mathbf{x} - \mathbf{x}_a \mathbf{T} \mathbf{S} \mathbf{x} - \mathbf{1}(\mathbf{x} - \mathbf{x}_a)$ .....	13
2.3 Observation term of the cost function, $\mathbf{F} \mathbf{x} - \mathbf{y} \mathbf{T} \mathbf{S} \mathbf{y} - \mathbf{1} \mathbf{F} \mathbf{x} - \mathbf{y}$ .....	14
2.4 Bias correction.....	15
2.5 Implementation of the OEM at RAL.....	16
3 Task 1: Definition of the Measurement Covariance for the MW Channels.....	21
3.1 AMSU-A/B and IASI Observation Errors from ATOVS processing at the UK MetOffice.....	22
3.1.1 Background.....	22
3.1.2 Errors assumed in the Met Office operational 4D-Var system.....	22
3.1.3 Estimated IASI Errors from the Met Office operational 4D-Var system.....	24
3.2 Measurement Errors for AMSU and MHS processing from the literature.....	27
Atkinson 2001.....	27

Houshangpour 2005 .....	29
Jimenez 2005 .....	30
Li 2000.....	31
McKague 2001 .....	33
McKague 2003 .....	35
Mitra 2010 .....	35
Olsen 2008.....	37
John 2008.....	38
Rosenkranz 2001.....	39
Susskind 1998 .....	40
Susskind 2003 .....	40
Vangasse 1996 .....	41
Wu 2001.....	42
Eyre 1989 .....	43
Chou 2004.....	44
3.3 Measurement Error Estimates for AMSU and MHS from COMPARISON to FORWARD SIMULATIONS .....	47
3.4 Estimating the Cross-Correlations of the Measurement Errors of AMSU/MHS .....	54
3.4.1 Hollingsworth/Loennberg Method .....	54
3.4.2 Background Error Method .....	54
3.4.3 Desroziers Method.....	55
3.4.4 Comparison of Hollingsworth, Desroziers, etc. vs. RAL and MetOffice Measurement Errors	58
4 Tasks 2 & 3: OEM(MWIR/Metop-B) over ocean, clear-sky and Land, clear-sky.....	59
4.1 Derivation of bias correction and observational error covariance for AMSU+MHS, BASED on IASI retrievals.....	59
4.2 IASI OEM retrievals (IR and MWIR): Results .....	64
5 Task 4: OEM (MWIR/Metop-B) over land, clear-sky, with variable emissivities .....	70

5.1	Addition of land surface emissivity to state vector .....	70
5.2	OEM retrievals of MWIR and statistical analysis .....	75
5.2.1	Overview of Simulations .....	75
5.2.2	Comparisons of Observed and Simulated spectra using different emissivity atlases .....	76
5.2.3	Example retrievals with Emissivity Included .....	79
5.2.4	Retrieval of IR bias correction scale factors .....	80
5.2.5	Impact of emissivity retrieval on Temperature and Humidity .....	89
6	Task 5: OEM(MWIR/Metop-B) in partial or full cloudy IFOVs .....	91
6.1	McNally-Watts Method (WMC) .....	91
6.2	Retrieval of Cloud in the OEM .....	94
6.3	Comparison of Cloud Measures .....	95
6.4	OEM retrievals (MWIR) w/ clouds and statistical analysis .....	101
7	Task 6: Retrievals with one or more missing AMSU channels .....	113
7.1	Linear Simulations .....	114
7.2	Global Retrievals .....	114
7.3	Comparison of Metop-A and Metop-B Retrievals .....	115
8	Conclusions .....	117
8.1	Summary and Conclusions .....	117
8.2	Suggestions for Further Work .....	118
9	References .....	120

## ACRONYMS USED IN THIS DOCUMENT

AMSU	Advanced Microwave Sounding Unit
AK	Averaging Kernel
BADC	British Atmospheric Data Centre
CFI	Customer Furnished Item
ECMWF	European Centre for Medium Range Weather Forecast
EO	Earth Observation
ESD	Estimated standard deviation (sqrt-diagonals of OEM solution covariance)
IASI	Infrared Atmospheric Sounding Interferometer
IR	(mid-) Infra-Red
ITT	Invitation to Tender
MHS	Microwave Humidity Sounder
MW	Microwave
NWP	Numerical Weather Prediction
OEM	Optimal Estimation Method
RAL	Rutherford Appleton Laboratory
RSG	Remote Sensing Group
RTTOV	Radiative Transfer for TOVS
SoW	Statement of Work
STFC	Science and Technology Facilities Council

## DOCUMENT REVISION HISTORY

Revision No.	Description	Date
V1.0	Completion of Task 1	12 Feb 2014
V2.0	Completion of Task 2	7 April 2014
V3.0	Completion of Task 3+4	11 July 2014
V4.0	Completion Task 5	7 November 2014
v5.0	Draft final report	27 January 2015

## 1 OVERVIEW

This report describes results from the Eumetsat study “Optimal Estimation Method retrievals with IASI, AMSU and MHS measurements”. The objectives of the study are to specify a configuration to make joint use of IASI, AMSU and MHS measurements in retrievals based on the optimal estimation method (OEM). The study characterises the added value of using MW and IR radiances in synergy for the retrievals of water vapour and temperature in cloud-free scenes with the OEM in comparison to using IASI radiances only, and will also explore the potential of the method for cloudy scenes. Furthermore, the study shall characterise the impact of the loss of one or more AMSU channels.

The work was performed by the Remote Sensing Group (RSG) at STFC’s Rutherford Appleton Laboratory (RAL Space), with consultancy support from Dr William Bell of the UK Met Office, who brings specific expertise in the exploitation of AMSU and MHS measurements.

The work is based on extending the existing Eumetsat IASI OEM, a version of which has been implemented at RAL (using their own in house tools). The scheme has extended to include AMSU and MHS observations and evaluated by comparing the retrieved temperature and humidity profiles against ECMWF analyses, and against the operational configuration. Retrievals are also assessed via standard diagnostics, such as fit residuals (in measurement space) and the gain of information quantified via diagnostics such as information content, degrees of freedom for signal and the averaging kernels (AKs).

The study is divided into six main tasks:

- Task 1: Definition of the measurement covariance matrix for the MW channels
- Task 2 OEM(MWIR/Metop-B) over ocean, clear-sky
- Task 3: OEM(MWIR/Metop-B) over land, clear-sky, with fixed emissivities
- Task 4: OEM(MWIR/Metop-B) over land, clear-sky with variable emissivities
- Task 5: OEM(MWIR/Metop-B) in partial or full cloudy IFOVs
- Task 6: Retrievals with one or more missing AMSU channels

This report is complemented by a Annex, which contains a comprehensive collection of plots characterising the performance of the retrievals.

## 1.1 THE ATOVS INSTRUMENT SUITE

The ATOVS (Advanced TIROS (Television and Infrared Observational Satellite) Operational Vertical Sounder) is a sounding instrument package first flown on the NOAA-KLM (-15, -16, -17) satellite series. It is composed of the Advanced Microwave Sounding Units A and B (AMSU-A, AMSU-B) and is complemented by the High Resolution InfraRed Sounder (HIRS/3).

For Metop and the NOAA-18 and -19 satellite series, the AMSU-B sounder has been replaced by the Microwave Humidity Sounder (MHS), and the infrared sounder has been upgraded to HIRS/4.

Although not considered formally part of the ATOVS package, the Advanced Very High Resolution Radiometer (AVHRR/3) is an imager also flying on Metop and on NOAA-18 and -19, which supports the ATOVS Level 1b processing.

A detailed account of the ATOVS instruments technical characteristics is given in the NOAA KLM user guide<sup>1</sup>, but we will give in the next sections the basic information necessary for product understanding and usage.

## 1.2 AMSU-A

### 1.2.1 TECHNICAL DESCRIPTION AND SPECTRAL CHARACTERISTICS

The AMSU-A is a fifteen-channel microwave radiometer that is used for measuring global atmospheric temperature profiles and providing information on atmospheric water in all of its forms.

AMSU-A measures in 15 spectral bands, summarised in the table below, where the temperature sounding mainly exploits the oxygen band at 50 GHz.

Hardware for the two lowest frequencies is located in one module (AMSU-A2) and that for the remaining thirteen frequencies in the second module (AMSU-A1). This arrangement puts the two lower atmospheric moisture viewing channels into one module and the oxygen absorption channels into a second common module, in order to ensure commonality of viewing angle independent of any module and/or spacecraft misalignment due to structural or thermal distortions. The AMSU-A2 module has a single antenna assembly, providing data for channels 1 and 2. AMSU-A1 has two separate antenna assemblies: AMSU-A11 provides data for channels 6, 7 and 9-15, and AMSU-A12 provides data for channels 3, 4, 5 and 8.

The following table summarises the spectral characteristics of AMSU-A.

<sup>1</sup> NOAA KLM User's Guide. URL: <http://www2.ncdc.noaa.gov/docs/klm>

Channel	Channel frequency (GHz)	No. of pass bands	Nominal bandwidth (MHz)	Temperature sensitivity (K)	Calibration accuracy (K)	<a href="#">Polarisation angles</a>
AMSU-A2						
1	23.8	1	270	0.30	<2.0	90- $\theta$
2	31.4	1	180	0.30	<2.0	90- $\theta$
AMSU-A1						
3	50.3	1	180	0.40	<1.5	90- $\theta$
4	52.8	1	400	0.25	<1.5	90- $\theta$
5	53.59 $\pm$ 0.115	2	170	0.25	<1.5	$\theta$
6	54.40	1	400	0.25	<1.5	$\theta$
7	54.94	1	400	0.25	<1.5	90- $\theta$
8	55.50	1	330	0.25	<1.5	$\theta$
9	F <sub>LO</sub> = 57.290344	1	330	0.25	<1.5	$\theta$
10	F <sub>LO</sub> $\pm$ 0 .217	2	78	0.40	<1.5	$\theta$
11	F <sub>LO</sub> $\pm$ 0 .3222 $\pm$ 0 .048	4	36	0.40	<1.5	$\theta$
12	F <sub>LO</sub> $\pm$ 0 .3222 $\pm$ 0 .022	4	16	0.60	<1.5	$\theta$
13	F <sub>LO</sub> $\pm$ 0 .3222 $\pm$ 0 .010	4	8	0.80	<1.5	$\theta$
14	F <sub>LO</sub> $\pm$ 0 .3222 $\pm$ 0 .0045	4	3	1.20	<1.5	$\theta$
15	89.0	1	<6000	0.50	<2.0	90- $\theta$

The polarisation angle is defined as the angle from horizontal polarisation (electric field vector parallel to the satellite track) where  $\theta$  is the scan angle from nadir.  $\theta$  indicates horizontal polarisation and 90- $\theta$  indicates vertical polarisation.

**Table 4.1: Spectral characteristics of AMSU-A**

Each antenna assembly contains a warm calibration target with a different number of Platinum Resistance Thermometers (PRTs), five for the AMSU-A1 modules and seven for the AMSU-2 module.

### 1.2.2 SCANNING GEOMETRY

AMSU-A is an across-track scanning system with a scan range of  $\pm 48.33^\circ$  with respect to the nadir direction. The instantaneous field of view (IFOV) of each channel is approximately 57.6 milliradians ( $3.3^\circ$ ) leading to a circular instantaneous field of view size close to 47.63 km at nadir and a swath width of  $\pm 1026.31$  km (sampling time of 200.0 ms) for a nominal altitude of 833 km. The sampling angular interval is close to 58.18 milliradians ( $3.3333^\circ$ ). The distance between two consecutive scans is approximately equal to 52.69 km.

There are 30 Earth views, two views of the internal warm target, and two views of cold space per scan line for each channel. Each scan takes 8.0 seconds to complete.

The following table summarises the scanning characteristics.

Characteristics	Value	Unit
Scan direction	West to East (northbound)	-
Scan type	Step	-
Scan rate	8	s
Sampling interval (duration)	200	ms
Sampling interval	3.3333	deg
Pixels/scan	30	-
Swath	±48.33	deg
Swath width	±1026.31	km
IFOV	3.3	deg
IFOV type	Circular	-
IFOV size (nadir)	47.63	km
IFOV size (edge) - across track	146.89	km
IFOV size (edge) - along track	78.79	Km
Scan separation (adjacent scan lines)	52.69	Km

**Table 4.2: Scanning characteristics of AMSU-A**

### 1.2.3 INSTRUMENT CALIBRATION

During each in-orbit scan line, the AMSU-A views three different types of targets:

- 30 Earth views (pixels)
- 2 views of the internal warm target (~300 K)
- 2 views of cold space (~2.73 K)

The accuracy of the warm calibration load brightness temperature is better than  $\pm 0.2$  K.

The cold space views, together with the internal warm target views and PRT measurements, are used during the ground processing to calibrate the AMSU-A radiances.

## 1.3 MHS

### 1.3.1 TECHNICAL DESCRIPTION AND SPECTRAL CHARACTERISTICS

MHS is a five-channel microwave radiometer, which complements the Advanced Microwave Sounding Unit-A (AMSU-A) channels. In some MHS description documents, MHS channels may be numbered as a continuation of the AMSU-A channels: 16, 17, 18, 19 and 20.

It is planned to derive from these frequencies humidity profiles and cloud liquid water content. Additionally, the instrument's sensitivity to large water droplets in precipitating clouds can provide a qualitative estimate of precipitation rates.

It is technically similar to the AMSU-B instrument, except for channel 20, where the AMSU-B side-band at 176.31 GHz is missing.

The following table summarises the spectral characteristics of MHS.

Channel	Central frequency (GHz)	Bandwidth (MHz)	Temperature sensitivity (K)	Calibration accuracy (K)	Polarisation
H1	89.0	±1400	1.0	1.0	V
H2	157.0	±1400	1.0	1.0	V
H3	183.311±1.00	±250	1.0	1.0	H
H4	183.311±1.00	±500	1.0	1.0	H
H5	190.311	±1100	1.0	1.0	V

**Table 4.5: Spectral characteristics of MHS**

### 1.3.2 SCANNING GEOMETRY

MHS is an across-track scanning system with a scan range of  $\pm 49.44^\circ$  with respect to the nadir direction. The IFOV of each channel is approximately 19.2 milliradians ( $1.1^\circ$ ) leading to a circular instantaneous field of view size close to 15.88 km at nadir for a nominal altitude of 833 km. Each scan takes 2.667 seconds to complete.

The scan of the MHS instrument is synchronised with the AMSU-A scan, i.e. there are three scans of MHS for each scan of AMSU-A.

There are 90 Earth samples per scan and per channel for a swath width of  $\pm 1077.68$  km (sampling time of 19.0 ms). The sampling angular interval is close to 19.39 milliradians ( $1.1111^\circ$ ), which is slightly larger than that of AMSU-B ( $1.1000^\circ$ ). The distance between two consecutive scans is approximately equal to 17.56 km.

The following table summarises the scanning characteristics.

Characteristics	Value	Unit
Scan direction	West to East (northbound)	-
Scan type	continuous	-
Scan rate	2.667	s
Sampling interval (duration)	18.52	ms
Sampling interval	1.1111	Deg
Pixels/scan	90	-
Swath	±49.44	Deg
Swath width	±1077.68	km
IFOV	1.1	deg
IFOV type	circular	-
IFOV size (nadir)	15.88	km
IFOV size (edge) - across track	52.83	km
IFOV size (edge) - along track	27.10	km
Scan separation	17.56	km

**Table 4.6: Scanning characteristics of MHS**

### 1.3.3 INSTRUMENT CALIBRATION

The MHS instrument calibration is based upon the measurement of cold space and of an on-board black body target. This calibration sequence is performed once every 2.667 seconds for each scan line. During one scan, MHS observes

- 90 Earth views (pixels)
- 4 views of the internal warm target (~300 K)
- 4 views of cold space (2.73 K)

The warm target contains five platinum resistance thermometers (PRTs), as opposed to the seven PRTs for the older NOAA AMSU-B instrument.

The cold space views, together with the internal warm target views and PRT measurements, are used during the ground processing to calibrate the MHS radiances.

## 2 ALGORITHM TECHNICAL DESCRIPTION AND METHODOLOGY

### 2.1 OPERATIONAL IASI PROCESSOR AT EUMETSAT

As an implementation of an OEM retrieval, the operational IASI processor seeks to find the state vector,  $\mathbf{x}$ , which minimise the cost function

$$J = (\mathbf{x} - \mathbf{x}_a)^T \mathbf{S}_a^{-1} (\mathbf{x} - \mathbf{x}_a) + (\mathbf{F}(\mathbf{x}) - \mathbf{y})^T \mathbf{S}_y^{-1} (\mathbf{F}(\mathbf{x}) - \mathbf{y})$$

Where

- $\mathbf{x}$  is a vector containing the parameters to be retrieved.  $\mathbf{x}_a$  describes the *a priori* estimate of the state
- $\mathbf{S}_a$  is the *a priori* covariance matrix (representing the assumed errors on the *a priori* estimate).
- $\mathbf{F}(\mathbf{x})$  is a forward model which predicts the observed radiances given the estimated state.
- $\mathbf{y}$  is the vector of measurements.
- $\mathbf{S}_y$  is the measurement covariance (representing the assumed errors on the measurements).

The operational OEM scheme for IASI has the following characteristics:

- The state vector contains profiles of atmospheric water vapour, temperature and ozone, together with the surface skin temperature. The profiles are represented in terms of principle components (see below).
- The forward model is RTTOV (version 10.2).
- IASI measurements are reconstructed from L1B observations using a principle component based method which also filters some instrument artefacts.

The scheme has been specified to RAL, via a set of files (CFIs) which define each term in OE cost function, together with the first guess state to be used for the retrieval (which is based on a linear regression to the observations [Ref:6] . This information is sufficient to allow the performance of the operational retrieval to be reproduced at RAL, using its own code.

The files were described in a technical note which is summarised below. Generally the configuration files are in hdf5 format. Files containing global measurements from IASI, AMSU and MHS, together with necessary auxiliary data, have been provided for 3 days (17 April, 17 July, 17 October 2013).

### 2.2 BACKGROUND TERM OF THE COST FUNCTION, $(\mathbf{x} - \mathbf{x}_a)^T \mathbf{S}_x^{-1} (\mathbf{x} - \mathbf{x}_a)$

The state-vector  $\mathbf{x} \in R^n$  represents the quantities to be retrieved: temperature profile (T), water vapour profile (W), ozone profile (O) and surface skin temperature (Ts). The profiles are represented as principal component (PC) scores of the deviation with respect to the a-priori. The number of principal component scores used for each of the three types of profiles are  $n_T = 28, n_W = 18, n_O = 10$ . The total number of state-vector elements is  $n = n_T + n_W + n_O + 1$ .  $\mathbf{S}_x$  is diagonal matrix. The elements on the diagonal can be extracted from the file COF\_STV as summarised below:

State-vector component	Dimension	Unit (of corresponding PCs)	Diagonal of Sx
$x_T$	$n_T$	K	/COF_STV/T_covariance
$x_W$	$n_W$	ln(ppmv)	/COF_STV/W_covariance
$x_O$	$n_O$	ln(ppmv)	/COF_STV/O_covariance
$x_{Ts}$	1	K	$9K^2$

As the PC scores used in the state-vector representation of the profiles are based on deviations from an a-priori profile given at the 101 fixed pressure levels RTTOV grid, the a-priori  $x_a$  in this representation is zero (except of course for the last element corresponding to Ts). The principal components required to expand the PC scores into profiles represented at 101 pressure levels are also contained in the file COF\_STV.

### 2.3 OBSERVATION TERM OF THE COST FUNCTION, $(F(x) - y)^T S_y^{-1} (F(x) - y)$

The IASI observations are represented as a subset of reconstructed IASI L1C radiances with the unit  $mW/m^2/sr/cm^{-1}$ . The channel selection (consisting of  $m = 139$  channels) and the observation error covariance matrix,  $S_y$  (unit:  $(mW/m^2/sr/cm^{-1})^2$ ), are provided in COF\_SY. Note that the channel selection is provided with an assumed IASI channel numbering from 0 to 8460.

The forward model  $F: R^n \rightarrow R^m$  is composed of two functions: the state-vector representation function  $X: R^n \rightarrow R^N$  and the RTTOV 10.2 implemented function  $f: R^N \rightarrow R^m$ . Here,  $N = 304$ , corresponding to the atmospheric temperature in K, the atmospheric water vapour concentration in ppmv and the atmospheric ozone concentration in ppmv, all at 101 fixed pressure levels each as well as the surface skin temperature. The state-vector representation function is computed individually for each component. For T we have  $X_T = X_T^a + E_T x_T$ , where  $E_T \in R^{N_T \times n_T}$  are the  $n_T$  leading principal components found in the dataset /COF\_STV/T\_eigenvectors and  $X_T^a$  is the a priori temperature profile in K at 101 levels which will be provided for each individual field of view. This is similar for W and O, except that the principal components are based on ln(ppmv) such that we get  $X_W = \exp(\ln(X_W^a) + E_W x_W)$  and  $X_O = \exp(\ln(X_O^a) + E_O x_O)$ , where  $X_W^a$  and  $X_O^a$  are the a priori water vapour and ozone concentrations in ppmv at 101 levels.

The reconstructed radiances,  $y$ , are obtained from the IASI L1C PC scores provided in the PRP files using the eigenvector files IASI\_EV?\_xx\_M02 (applicable to both Metop-A and B). To suppress instrument artefacts this is followed by a projection onto the forward model subspace as defined by the first 62 vectors in IASI\_EV1\_1C\_M02\_FS.hdf5 and the first 77 vectors in IASI\_EV2\_1C\_M02\_FS.hdf5 (no channels from Band 3 enter the retrievals). The format of the eigenvector files and how to compute reconstructed radiances is described in detail in [Ref:1] [Ref:2]

## 2.4 BIAS CORRECTION

IASI observations are corrected for bias (defined by Eumetsat in a CFI) using two vectors,  $\mathbf{b}_0$  and  $\mathbf{b}_1$ , which define a fixed bias spectrum and a scan dependent term. The measurement used in the retrieval,  $\mathbf{y}$ , is then given by

$$\mathbf{y} = \mathbf{y}'' - \mathbf{b}_0 - \mathbf{b}_1 (\sec(\theta) - \mu_0)$$

**Equation 1**

Where  $\mathbf{y}''$  is the double-filtered measurement vector (described in the previous section);  $\theta$  is the satellite zenith angle (at the ground) and  $\mu_0$  is a constant.

## 2.5 IMPLEMENTATION OF THE OEM AT RAL

Using the CFIs provided by Eumetsat, the OEM retrieval has been implemented at RAL.

The code has been extended so that observations from IASI and MHS are also ingested and simulated by the FM (again using RTTOV 10.2). Coefficient files used are as follows:

- `rttov7pred54L/rtcoef_metop_1_amsua.dat`: Creation date 16 May 2013.
- `rttov7pred54L/rtcoef_metop_1_mhs.dat`: Creation date 16 May 2013
- `rttov7pred101L/tcoef_metop_2_iasi.bin`: Creation date 28 March 2013

As indicated by the directory names, the MW coefficients are only defined on 54 levels, whereas the IASI coefficients are provided on 101 levels (the same as the levels on which the state principle components are provided). The code forms the state vector on the 101 levels and then linearly interpolates in pressure to the MW grid, before calling RTTOV for AMSU and MHS.

Note that, although separate files are provided, there are no differences (other than the platform ID) between the AMSU or MHS coefficients for metop-1 (i.e. Metop-B) and metop-2 (Metop-A). IASI coefficients are only provided for metop-2 (Metop-A).

Output (for IASI only) from the RAL implementation and the Eumetsat scheme have been compared for the 117 valid observations (out of 120 possible) in the first scan line of measurements from IASI file ID:

`IASI_1C_M01_20130417224800Z_20130417225055Z_N_C_20130418001733Z`

Results are compared in the following figures:

- Figure 2-1 shows the Eumetsat simulated (based on the first-guess state) brightness temperatures (top left) and the difference between these and those from the RAL implementation (top-right). The figure also shows the modelled surface emissivity (from RTTOV) from Eumetsat (bottom left) and the difference from the RAL version (bottom right).
- Figure 2-2 shows the cost function at initial guess for each scene.
- Figure 2-3 shows for the first of these scenes a comparison between the weighting functions for each element in the state vector. Note the state vector is expressed in terms of principle components of the physical profile variables.

In general differences found are sufficiently small to conclude that the RAL implementation should reproduce the performance of the Eumetsat scheme.

Results from iterative retrievals are compared in tasks 2 and 3, reported below.

Retrieval diagnostics for the first scene from the above IASI file, from the RAL scheme are illustrated in Figure 2-4. These are linear diagnostics based on the weighting functions estimated for the first guess state. Estimated solution errors shows are the square-root diagonal elements of the solution covariance:

$$S_x = (S_a^{-1} + K^T S_y^{-1} K)^{-1}$$

Averaging kernels show the sensitivity of the retrieved profiles to perturbations of the true state. In this case:

$$A = (S_a^{-1} + K^T S_y^{-1} K)^{-1} K^T S_y^{-1} K'$$

Where  $\mathbf{K}$  is the weighting function matrix (containing the derivatives of the forward model with respect to each element of the state vector).  $\mathbf{K}'$  is the derivative of the forward model with respect to perturbations on the 101 RTTOV model levels. The figure shows  $\mathbf{A}' = \mathbf{U} \mathbf{A}$ , the projection of  $\mathbf{A}$  from the state vector (principal component) representation onto the model vertical grid.  $\mathbf{U}$  is the matrix which contains the principal component basis vectors.

The degrees of freedom for signal (DOFS) are also indicated for each species in the title above each averaging kernel. Ozone and water vapour errors and averaging kernels are shown relative to the initial guess state. Note the ozone averaging kernels for lower levels exhibit a large apparent sensitivity to ozone in the stratosphere, partly due to this relative representation (mixing ratios in the stratosphere are much larger than those in the lower troposphere).

One difference between the RAL and Eumetsat OEM implementation is the non-linear iteration and convergence approach: The RAL non-linear retrieval code uses the Marquardt-Levenberg update scheme (to improve convergence). It determines convergence based on change in cost function between iterations: If the change in cost is smaller than 1 then a retrieval is considered to have potentially converged. At this point, a purely Newtonian iteration is performed (i.e. without using the Marquardt-Levenberg term). If again the cost changes by less than 1 then the retrieval is considered to have converged. For these retrievals, the initial Marquardt-Levenberg term is set to be negligible. The term will only contribute significantly if updates to the state result in degraded cost. In practise, almost all retrievals converge directly in 2-3 iterations. So, almost all retrievals are the result of effectively pure Newtonian iteration. It is therefore unlikely that any significant differences between the RAL and Eumetsat ODV results are caused by this difference in iteration/convergence approach, but it may be expected that results will not be exactly identical.

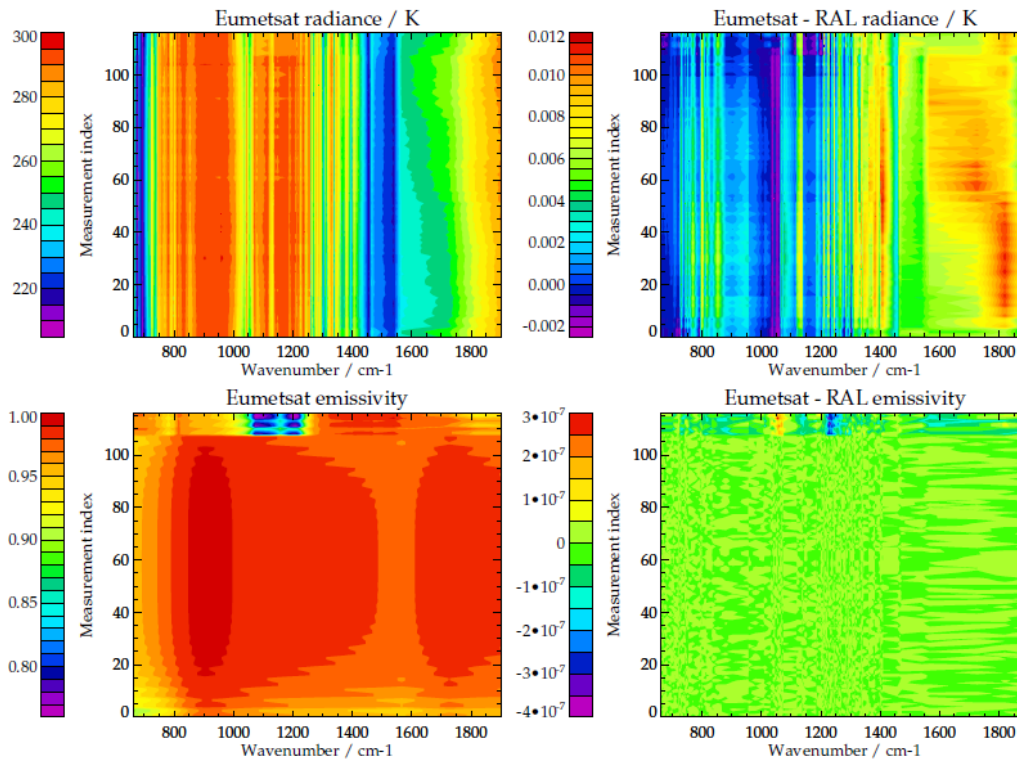


Figure 2-1: Comparison between simulated measurements (top panels) and modelled surface emissivity from the Eumetsat and RAL implementation of the IR OEM.

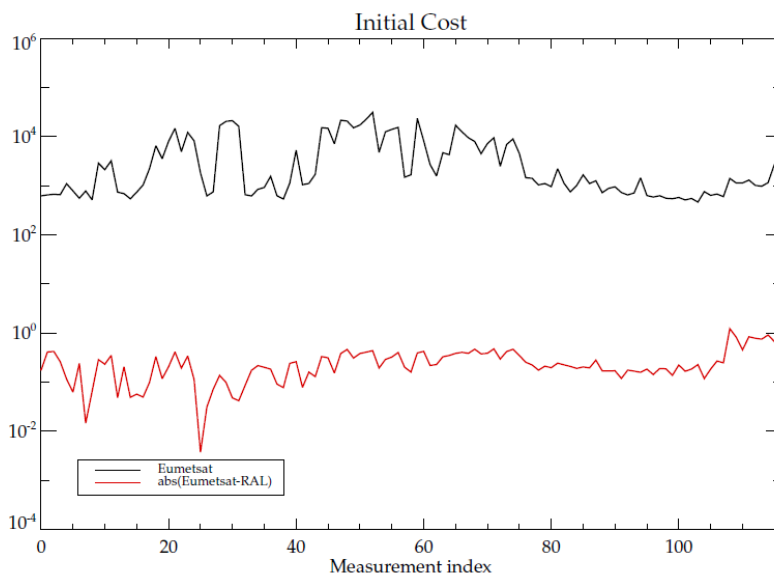


Figure 2-2: Comparison between initial cost-function values from the Eumetsat and RAL implementation of the IR OEM.

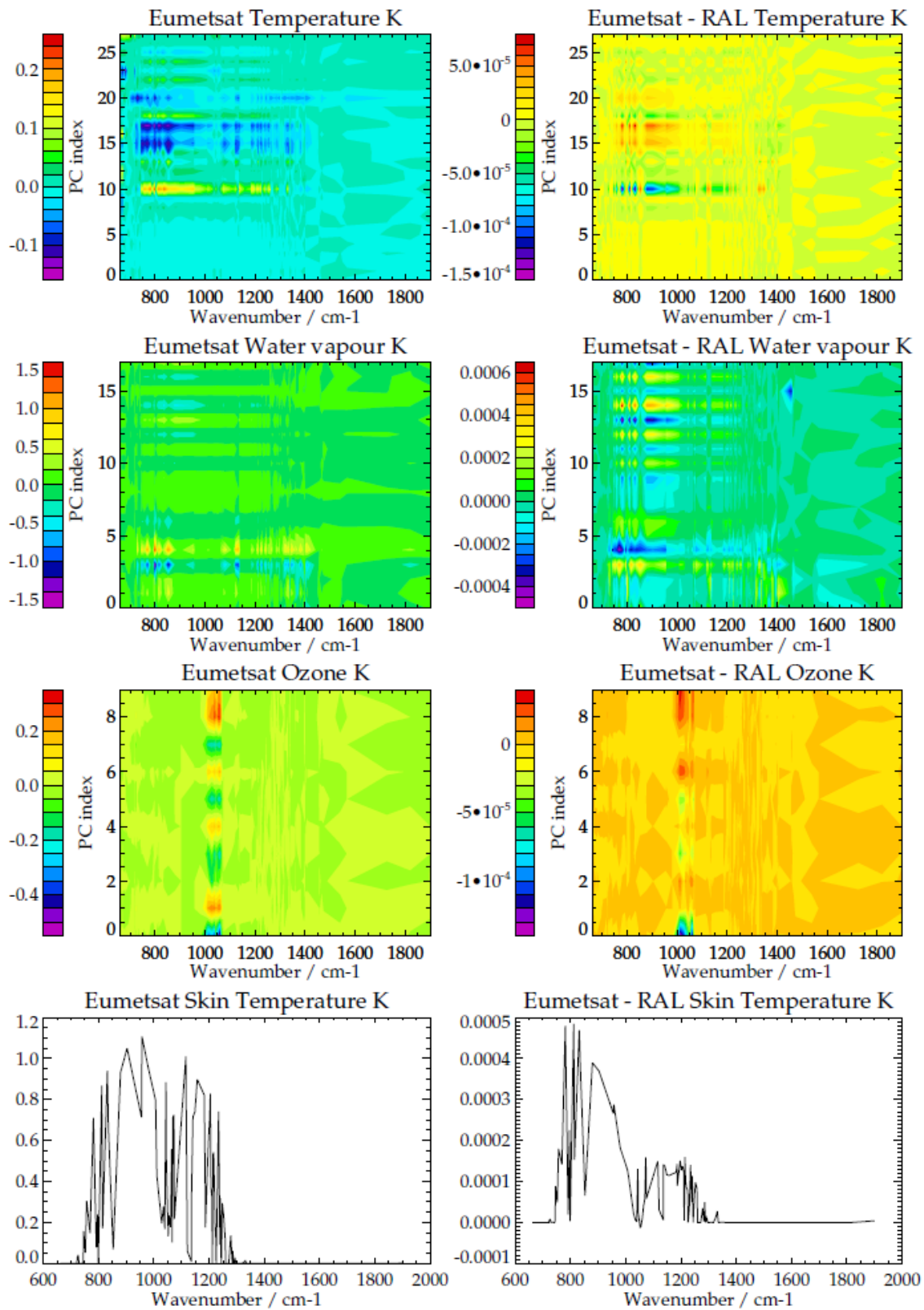


Figure 2-3: Comparison between weighting functions from the Eumetsat and RAL implementation of the IR OEM.

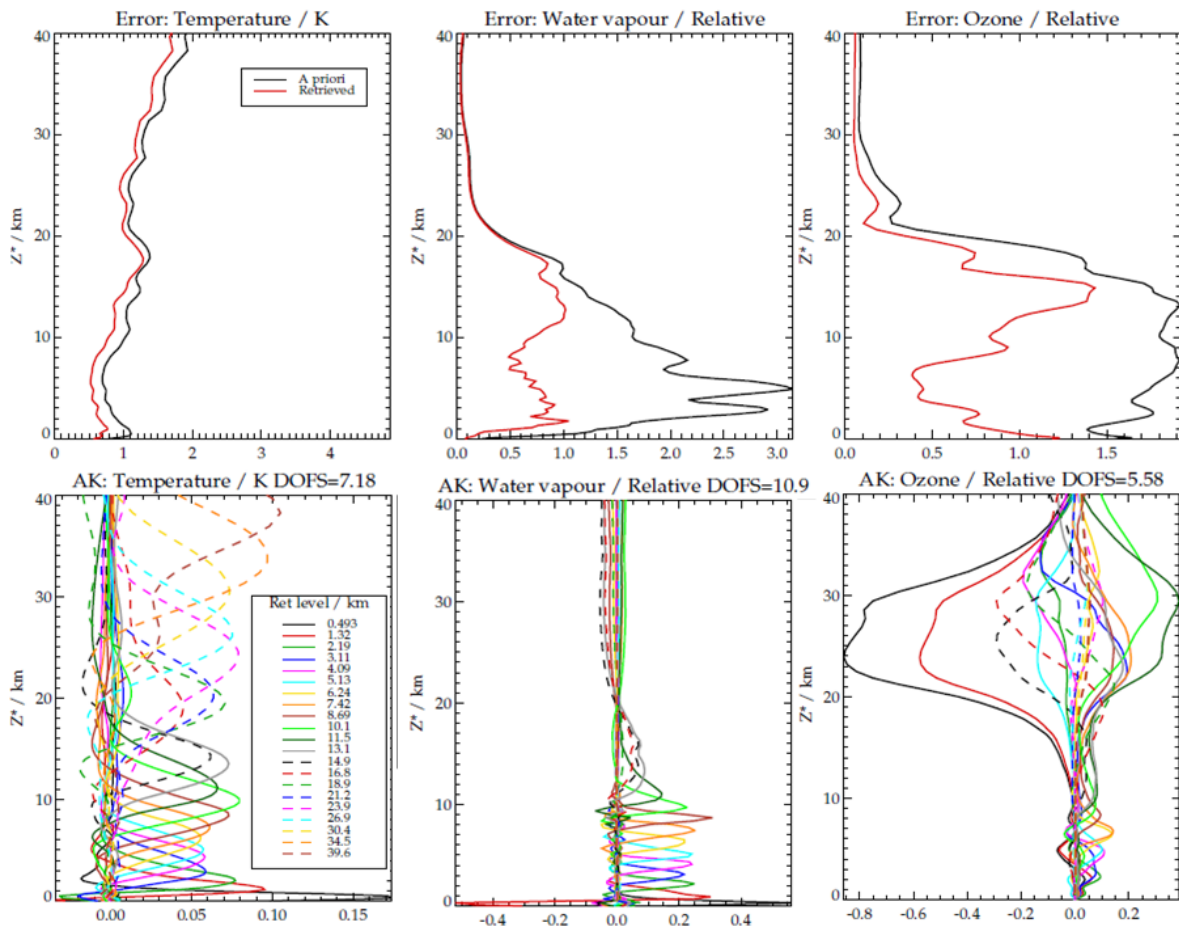


Figure 2-4: Retrieval diagnostics from the RAL scheme. Top panels show estimated solution and *a priori* errors. Bottom panels show averaging kernels for a subset of the 101 levels.

### 3 TASK 1: DEFINITION OF THE MEASUREMENT COVARIANCE FOR THE MW CHANNELS

This task covers the definition of the measurement error covariance matrices ( $S_y$ ) for the microwave (MW) instruments AMSU and MHS. It comprises 3 sub tasks:

- A description of the measurement errors used in the Met Office operational assimilation of AMSU and MHS observations. This work has benefitted from the involvement as a consultant to this study of Bill Bell of the Met Office
- A brief literature review of retrievals of water vapour and temperature from AMSU and MHS data, focusing on the treatment of measurement errors in the earlier works.
- Statistical comparisons to observations of radiances simulated based on the retrievals first guess atmospheric and surface state.

The work conducted here has provided a firm overview of errors used in the community, including in NWP at the Met Office and at ECMWF. However, subsequent to this task it was decided to define the MW measurement covariance using statistics (derived in the study) of the difference between measurements and observations simulated using the IR-only OEM output. This work particular work is discussed in section 4.1, below.

### 3.1 AMSU-A/B AND IASI OBSERVATION ERRORS FROM ATOVS PROCESSING AT THE UK METOFFICE

The following section describes the measurement errors for the AMSU-A/B instruments as used by the UK MetOffice for their operational ATOVS processing. The content of this section was provided by Dr William Bell and Peter Weston from the UK MetOffice. It reports the measurement errors, with a mention of the methods used in deriving their values.

#### 3.1.1 BACKGROUND

The assumed observation errors ( $\mathbf{R}$  in the notation of Ide,  $\mathbf{S}_y$  in the notation of Rogers) determine the weight given to the observations in the operational 4D-Var analysis.

In principle these estimates take account of several error sources in the observations:

- *Random instrument error*, for example resulting from the non-zero noise equivalent brightness temperatures (NE $\Delta$ T) associated with each measurement.
- *Forward model errors*, due to inaccuracies in the radiative transfer modelling. These may arise from errors in the underlying spectroscopy, or in the fast parameterisations used in the radiative transfer models. Strictly these errors are more likely to be manifested as a local bias in the forward calculations, but taken over large ensembles of states, are assumed to be part of the random observation error and included in  $\mathbf{R}$ .
- *Representativeness errors*, resulting from scale mis-match between observation horizontal scales (typically ~45-100 km for MW observations, 15-40km for IR observations) and the scales represented by the background, or *prior*, estimate of the state ( $\mathbf{x}_B$ ) which is typically significantly larger. Horizontal scale mis-match can also give rise to inter-channel correlations (as can forward model errors). These inter-channel correlations are sometimes dealt with using a diagonal  $\mathbf{R}$ , with inflation of the diagonal amplitudes to down-weight the observations.

In practice it is the *relative weights* of observations, determined by  $\mathbf{R}$ , and the background information (defined by the background error covariance matrix  $\mathbf{B}$ ) that determine the analysis state. Hence, sub-optimality in the estimation of  $\mathbf{B}$  can be compensated for by adjustment of the observation error covariances.

As will be shown, the assumed observation errors for the ATOVS channels are inflated relative to (i) the objectively estimated errors, from the diagnostic described by Desroziers (2005)<sup>2</sup>; and (ii) the known NE $\Delta$ T, which is believed to be the dominant contribution to the ATOVS observation errors, certainly for AMSU-A channels 6-13 (54.4 GHz — 57.29 GHz)

#### 3.1.2 ERRORS ASSUMED IN THE MET OFFICE OPERATIONAL 4D-VAR SYSTEM

<sup>2</sup> See Bormann and Bauer (2010) for the application to ATOVS, Weston *et al* (2014) for application to IASI.

Figure 3-1 below shows the observation errors diagnosed for the ATOVS channels used in operations during 2012 (Met Office now additionally assimilates MetOp-B radiances)

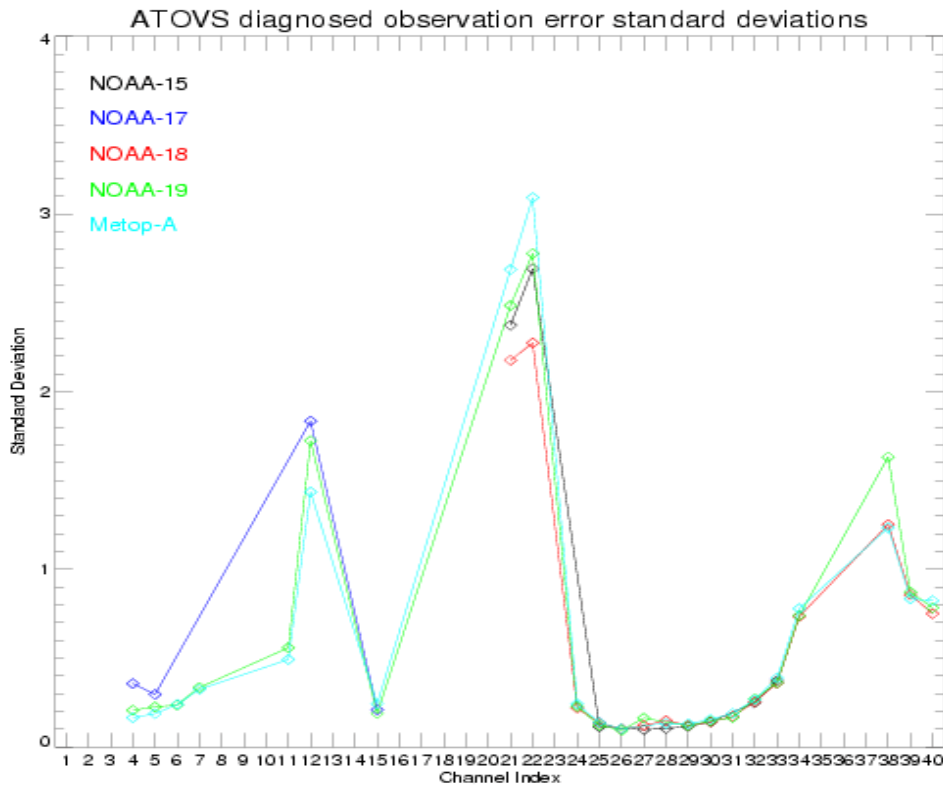


Figure 3-1: Observation errors diagnosed for the NOAA-15,-17,-18,-19 and Met Op-A using the Desroziers method. Results are shown for HIRS (channels 1-15) and AMSU-A (channels 21-35) and MHS / AMSUB (channels 36-40).

These estimates will include representativeness errors for the Met Office 4D-Var (N216 analysis and N512 background resolutions). These errors of representativeness affect the humidity sensitive channels most (HIRs channels 11 and 12, and AMSU-B / MHS channels 3,4,5)

For the key tropospheric temperature sounding channels, for which the radiometric performance is most critical, the diagnosed errors are in the range 0.10-0.13K for channels 6-9. These values are close to the effective NE $\Delta$ T for these channels, noting that the process of remapping the AMSU-A channels to the HIRS grid in a pre-processing step at the Met Office results in a 30% reduction in the effective noise of the AMSU-A observations, taking these channels from ~0.20K (unmapped) to ~0.13 K (mapped). Diagnosed errors get progressively larger for higher peaking channels (9-14) reflecting the decreasing bandwidth for these channels, and consequently higher NE $\Delta$ T.

Figure 3-2 compares the mean observation errors diagnosed for the instruments shown above, together with the assumed observation errors in 4D-Var. Figure 2 shows that assumed observation

errors are, for all ATOVS channels, inflated, relative to the diagnosed values. This inflation is derived in an *ad-hoc* manner by running full assimilation experiments and optimising forecast impact. This doubtlessly permits (small) sub-optimality in the assimilation system, but is to date the only practical way of dealing with: (i) uncertainties in the estimate of  $\mathbf{B}$  and (ii) the effects of inter-channel correlations.

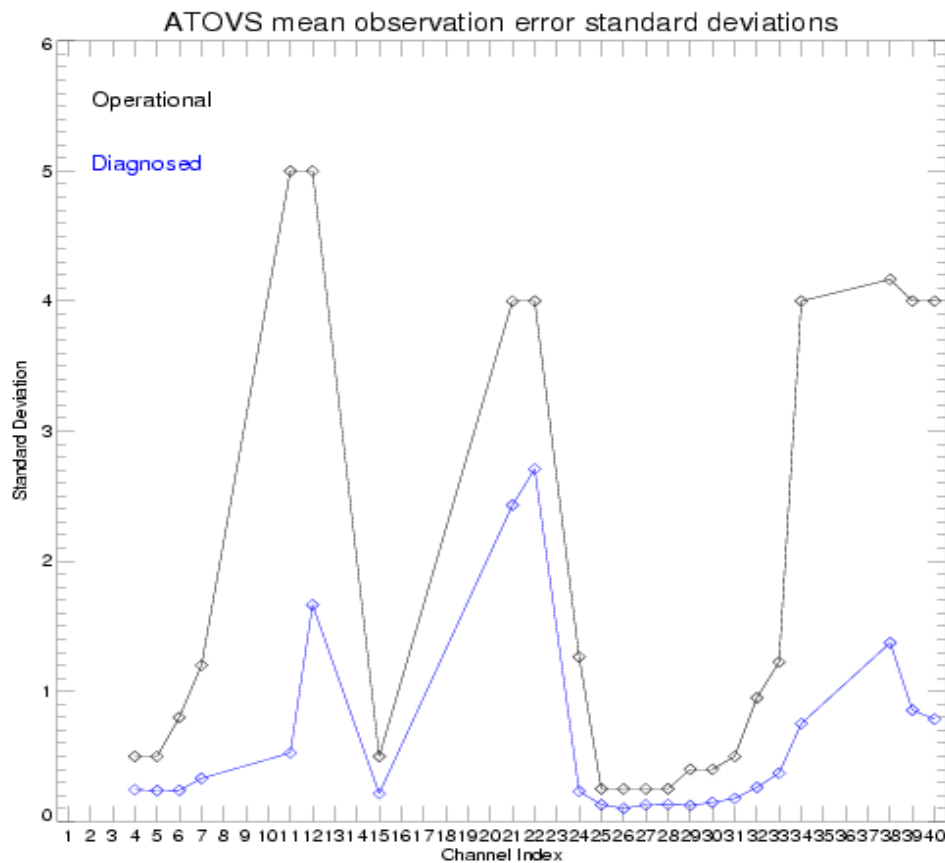


Figure 3-2: Mean diagnosed observation errors (blue) and assumed observation errors (black) in the Met Office operational 4D-Var assimilation system.

### 3.1.3 ESTIMATED IASI ERRORS FROM THE MET OFFICE OPERATIONAL 4D-VAR SYSTEM

The diagonal elements of the R matrix are shown for MetOp-A IASI, for both operationally used, and diagnosed errors in Figure 3-3 below. Also shown is the instrument noise ( $NE\Delta T$ ) for comparison.

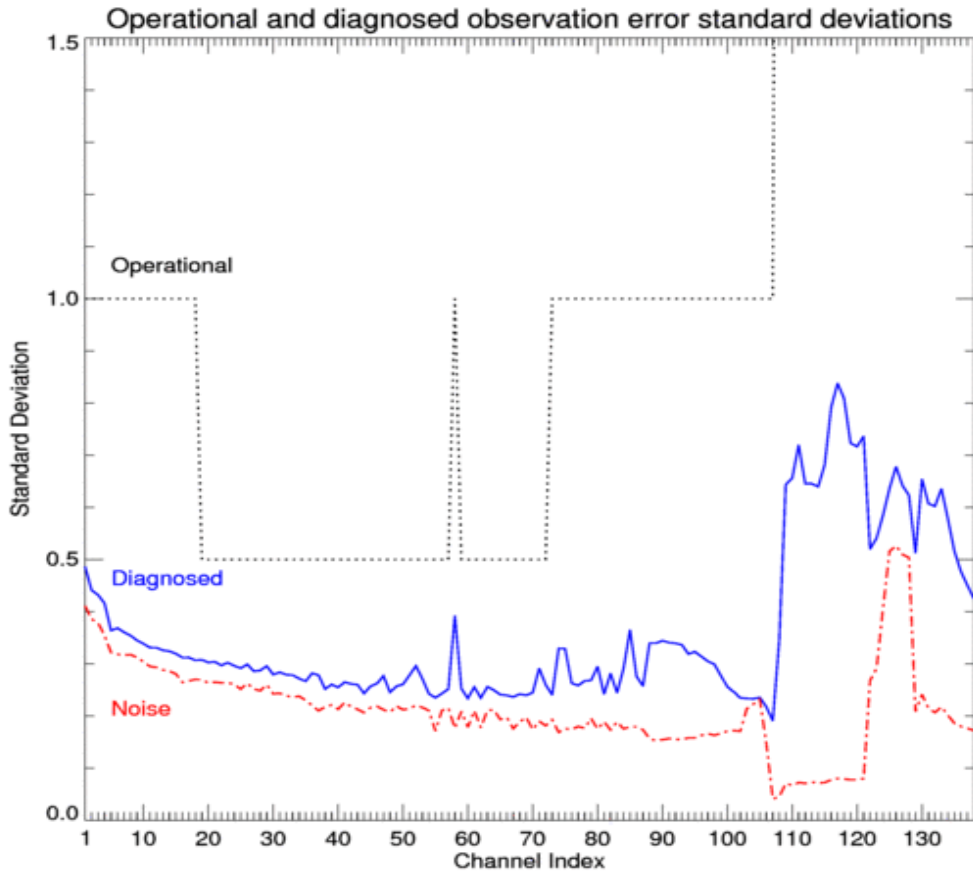


Figure 3-3: Mean diagnosed observation errors (blue) and assumed observation errors (black dashed) for IASI in the Met Office operational 4D-Var assimilation system. Also shown is the instrument noise (red).

The inter-channel diagnosed correlations for IASI are shown in Figure 3-4 below. Larger correlations are diagnosed for the water vapour sounding channels (channels 110-137) and for the lower peaking temperature sounding channels (90-110). The inter-channel correlations get progressively weaker for the higher peaking temperature sounding channels.

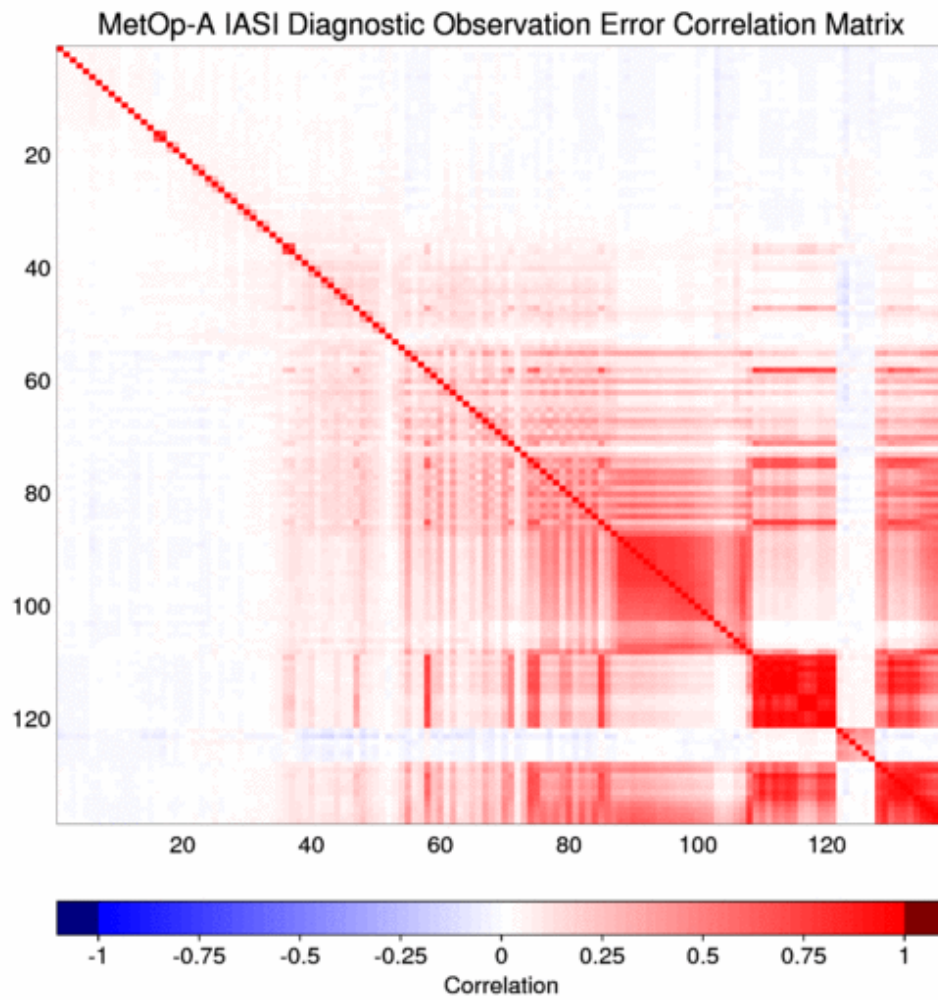


Figure 3-4: Diagnosed inter-channel correlation errors for IASI.

### 3.2 MEASUREMENT ERRORS FOR AMSU AND MHS PROCESSING FROM THE LITERATURE

There are different types of retrieval algorithms used for the processing of AMSU/MHS (and other instruments of the TOVS observation suite). They can generally be broken down into three different categories

- Linear regression algorithms
- Physical algorithms including those based on the OEM method to be employed in this study
- Neural network algorithms

We focus this review on how the measurement errors for AMSU and MHS have been treated by the authors of papers from all three categories of retrieval schemes.

A small number of publications also report on instrument effects encountered when working with AMSU / MHS data. These include the correction of asymmetries in the antenna pattern as a function of spectral channel, or corrections for a channel-dependant deterioration of the noise equivalent brightness temperature NEBT over time (not all channels are affected to the same extent). We also list some of these findings in the current section, as they will apply to this study.

The publications most relevant to the Optimal Estimation technique are those by Rosenkranz2001 and Susskind2003, who both use OEM. Chou2004 also gives a thorough analysis of observation errors for AMSU. A summary of selected articles is provided below.

---

#### ATKINSON 2001

N. C. Atkinson, CALIBRATION, MONITORING AND VALIDATION OF AMSU-B, Adv. Space Res. Vol. 28, No. 1. pp. 117-126, 2001

#### ABSTRACT

*The first flight models of the Advanced Microwave Sounding Unit (AMSU) were launched on the NOAA-15 satellite in 1998. This paper reviews the performance of AMSU-B to date, with particular reference to the problems experienced due to radio-frequency interference. It shows that a bias correction scheme developed by the Met Office and NOAA/NESDIS generally works well, though regular updates are necessary to keep track of long-term bias changes. The prospects for future AMSU-B flight models are discussed. The paper also outlines the aircraft-based campaigns that took place during 1999 for the purpose of validating those aspects of water-vapour measurement and spectroscopy that are important for AMSU.*

This paper presents an in-depth analysis of instrument effects that impact the data quality of AMSU-B. The researcher from the UK Met Office draws on a long experience of using AMSU-B data in NWP, based on which they have compiled an assessment of, in the first place, channel dependant biases over the current mission lifetime. They have also performed airborne campaign with a simulator radiometer which, although not used to validate AMSU-B measurements directly, were used to improve the radiative transfer model and to measure sea surface emissivity.

Soon after launch it was discovered that AMSU-B is susceptible to radio-frequency (RF) interference from the satellite data transmitters. This resulted in large scan-dependent biases in several channels.

The problem was compounded by intermittent faults in the transmitter antennas, resulting in erratic changes in the AMSU-B biases. However, in late September 1999 the spacecraft was re-configured to use two backup transmitters, and the primary transmitters were turned off. This greatly improved the quality of the AMSU-B data. Although biases still exist, they can be characterised by special tests in which each active transmitter in turn is turned off for brief periods.

The paper also discusses the monitoring of other critical instrument parameters, such as channel noise (NEAT) and instrument temperature.

Three different methods for determining biases are presented. The primary method of determining AMSU-B biases has been to use bi-monthly 'trending tests'. In this test each of the active transmitters (currently STX-2 and SARR) is turned off for periods of 30 seconds. By measuring the step-changes in Earth-view signal, an absolute measurement of bias associated with each transmitter is obtained. Other methods are comparison of a mean brightness temperature over a orbit with global mean brightness temperatures, and a comparison with NWP model statistics.

The conclusion is that AMSU-B channels 17, 19 and 20 are especially affected by biases up to 40K, but after September 1999 the main interfering transmitter has been switched off, and the biases have consequentially become much smaller.

The three methods of quantifying AMSU-B bias all indicate that scan-dependent bias drifts of up to 1K per month can occur, particularly for channel 19. Therefore periodic updates are necessary to the bias correction tables. With these updates the worst case accuracy should be +/-0.3K for channel 16, +/-1K for channels 17 and 18 and +/-2K for channels 19 and 20. The tables in the header of the NESDIS 1B data sets can be several weeks out of date; therefore it is recommended that up-to-date information should be available on the internet. It is intended that the Met Office web site will contain a link to the latest bias correction file ([www.metoffice.gov.uk](http://www.metoffice.gov.uk))

The summary of the analysis of other instrument parameters is that:

- A seasonal variation of instrument temperature can be seen, with corresponding minor variations in gain and offset. There is no evidence of any long-term warming (which might have been expected if the surface mirrors had started to deteriorate).
- There has been a gradual slight fall in gain for channels 18 20, and a slight increase in NEAT. NEAT values are still well within specification, with the exception of channel 18 which is now at the upper limit of its specification. The NEAT specifications are <1 .OK for channels 16, 17 and 19, <1 . I K for channel 18 and <1.2K for channel 20.
- Channel 16 NEAT shows some rapid variations towards the end of the period, though this is not thought to be a cause for concern at present. A slight anomaly is apparent for channel 17 early in 1999; NEAT also falls slightly for the other channels at this time, as the instrument temperature shows a rapid decrease.
- The rapid rise in NEAT for all channels at the start of the period is probably associated with the thermal stabilisation of the instrument in the period immediately following its initial turn-on.

Table 1. AMSU-B Channel Characteristics

Channel	Centre Frequency (GHz)	Lower Passband (GHz)	Upper Passband (GHz)	Polarisation Angle <sup>†</sup> (deg)	NEAT spec. (K)	Frequency Stability spec. (MHz)	Absolute accuracy spec. (K)
16	89.0	87.6–88.6	89.4–90.4	90–0	≤1.0	±100	≤1K
17	150.0	148.6–149.6	150.4–151.4	90–0	≤1.0	±100	≤1K
18	183.31±1.00	182.06–182.56	184.06–184.56	90–0	≤1.1	±50	≤1K
19	183.31±3.00	179.81–180.81	185.81–186.81	90–0	≤1.0	±70	≤1K
20	183.31±5.00	175.31–177.31	189.31–191.31	90–0	≤1.2	±70	≤1K

<sup>†</sup> The polarisation angle is defined as the angle from horizontal polarisation; 0 is the scan angle from nadir.

Table 2. AMSU-B Scan and Beam-shape Characteristics

Scan time	2.667 sec
Scan type	Continuous
Number of Earth samples per scan	90
Number of calibration samples per scan	4 space; 4 target
Integration time	0.018 sec
Time between samples	0.019 sec
Angular distance between samples	1.10°
Half-power beam width (full-width)	1.10°±0.11°
Main beam efficiency <sup>†</sup>	≥95%

<sup>†</sup> The main beam is defined as 2.5 times the half-power beam width

Figure 3-5: Characterisation of AMSU-B channels after Atkinson 2001.

HOUSHANGPOUR 2005

A. Houshangpour, V. O. John, and S. A. Buehler, Retrieval of upper tropospheric water vapor and upper tropospheric humidity from AMSU radiances, *Atmos. Chem. Phys.*, 5, 2019–2028, 2005

*Abstract.* A regression method was developed to retrieve upper tropospheric water vapor (UTWV in kg/m<sup>2</sup>) and upper tropospheric humidity (UTH in %RH) from radiances measured by the Advanced Microwave Sounding Unit (AMSU). In contrast to other UTH retrieval methods, UTH is defined as the average relative humidity between 500 and 200 hPa, not as a Jacobian weighted average, which has the advantage that the UTH altitude does not depend on the atmospheric conditions. The method uses AMSU channels 6–10, 18, and 19, and should achieve an accuracy of 0.48 kg/m<sup>2</sup> for UTWV and 6.3%RH for UTH, according to a test against an independent synthetic data set. This performance was confirmed for northern mid-latitudes by a comparison against radiosonde data from station Lindenberg in Germany, which yielded errors of 0.23 kg/m<sup>2</sup> for UTWV and 6.1%RH for UTH.

This paper uses a regression scheme to calculate upper tropospheric humidity from the clear sky brightness temperatures of channels with strong water vapour absorption. A simple radiance-to-UTH relationship was first derived by Soden and Bretherton (1993), indicating that the clear sky brightness temperature measured at a strong water vapour absorption line is proportional to the natural logarithm of the dividend of UTH over the cosine of the satellite viewing angle. Their method provides a high computational speed in transforming brightness temperature to relative humidity by eliminating a full retrieval. The method developed is a combination of regression techniques and a simple physical model of the observing system, one could call it a regression on a physical basis.

Assuming a model atmosphere, upper tropospheric temperature parameters could be approximated by linear combinations of AMSU-A temperature channel radiances (AMSU-A channels 6–10). The retrieval of upper tropospheric water vapour was facilitated by transforming the corresponding water vapour channel radiances (AMSU-B channels 18 and 19) to a fixed atmospheric temperature profile using upper tropospheric temperature information. It was shown that UTH is then an exponential function of the transformed brightness temperature under consideration. This exponential relationship could be easily linearised by taking logs. The original UTH model incorporating upper tropospheric water vapour as an explicit variable provides an excellent UTH retrieval when involving true values. However, it turned out to be sensitive to UTH retrieval errors.

This paper doesn't however report on these retrieval errors and how they would depend on the measurement errors in the AMSU radiances, so there is no direct relevance to our study.

---

#### JIMENEZ 2005

C. Jimenez, P. Eriksson, V. O. John, and S. A. Buehler, A practical demonstration on AMSU retrieval precision for upper tropospheric humidity by a non-linear multi-channel regression method, *Atmos. Chem. Phys.*, 5, 451–459, 2005

*Abstract. A neural network algorithm inverting selected channels from the Advance Microwave Sounding Unit instruments AMSU-A and AMSU-B was applied to retrieve layer averaged relative humidity. The neural network was trained with a global synthetic dataset representing clear-sky conditions. A precision of around 6% was obtained when retrieving global simulated radiances, the precision deteriorated less than 1% when real mid-latitude AMSU radiances were inverted and compared with co-located data from a radiosonde station. The 6% precision outperforms by 1% the reported precision estimate from a linear single-channel regression between radiance and weighting function averaged relative humidity, the more traditional approach to exploit AMSU data. Added advantages are not only a better precision; the AMSU-B humidity information is more optimally exploited by including temperature information from AMSU-A channels; and the layer averaged humidity is a more physical quantity than the weighted humidity, for comparison with other datasets. The training dataset proved adequate for inverting real radiances from a mid-latitude site, but it is limited by not considering the impact of clouds or surface emissivity changes, and further work is needed in this direction for further validation of the precision estimates.*

The authors present a neural network retrieval approach to retrieve humidity from selected channels of AMSU-A and AMSU-B. Temperature data from AMSU-A are used to accurately retrieve humidity from AMSU-B channels. This paper contains a good literature review of past humidity measurements for AMSU. These include Rosenkranz 2001 (iterative minimum variance algorithm), Greenwald and Christopher 2002 (simplified relationship between UTH and brightness temperature derived for infrared data, but no detailed description of the retrieval processor), Buehler and John 2005 (same relationship as Greenwald and Christopher, but for AMSU-B and with a detailed description of precision).

Some examples of weighting functions are given, but unfortunately no specific account of the treatment of measurement errors are supplied. The authors use a set of synthetic spectra and ECMWF model profiles to train their neural network algorithm. We presume that AMSU measurement errors are applied to the synthetic spectra, but the magnitude of the measurement errors is not given.

The authors also perform some traditional retrievals of AMSU profiles over a radiosonde launch site at Lindenberg (Germany) to validate how their neural network algorithm fares with real measurements. The validation is successful, but no details of the traditional retrieval results which could be of interest to our study are given.

---

## LI 2000

Li, Jun, Walter W. Wolf, W. Paul Menzel, Wenjian Zhang, Hung-Lung Huang, Thomas H. Achtor, 2000: Global Soundings of the Atmosphere from ATOVS Measurements: The Algorithm and Validation. *J. Appl. Meteor.*, 39, 1248-1268.

### ABSTRACT

*The International Advanced Television and Infrared Observation Satellite Operational Vertical Sounder (ATOVS) Processing Package (IAPP) has been developed to retrieve the atmospheric temperature profile, moisture profile, atmospheric total ozone, and other parameters in both clear and cloudy atmospheres from the ATOVS measurements. The algorithm that retrieves these parameters contains four steps: 1) cloud detection and removal, 2) bias adjustment for ATOVS measurements, 3) regression retrieval processes, and 4) a nonlinear iterative physical retrieval. Nine (3 x 3) adjacent High-Resolution Infrared Sounder (HIRS)/3 spot observations, together with Advanced Microwave Sounding Unit-A observations remapped to the HIRS/3 resolution, are used to retrieve the temperature profile, moisture profile, surface skin temperature, total atmospheric ozone and microwave surface emissivity, and so on. ATOVS profile retrieval results are evaluated by root-mean-square differences with respect to radiosonde observation profiles. The accuracy of the retrieval is about 2.0 K for the temperature at 1-km vertical resolution and 3.0–6.0 K for the dewpoint temperature at 2-km vertical resolution in this study. The IAPP is now available to users worldwide for processing the real-time ATOVS data.*

The authors present a comprehensive analysis software for ATOVS data, including AMSU-A and AMSU-B, but also the infrared instrument HIRS. HIRS data are used in the first two of four steps for cloud detection and parametrisation, and the removal of HIRS observation biases. A regression solution for the parameters to be retrieved is then found. The results of this first regression retrieval are then used as the first guess for a physical retrieval. It is a non-linear, iterative physical retrieval of the atmospheric temperature profile, moisture profile, atmospheric total ozone, surface skin temperature and microwave surface emissivity through solving the radiative transfer equation (RTE).

The paper present a full characterisation of AMSU-A and AMSU-B channels, including their spectral performance. They also tabulate a bias correction for each of the AMSU channels. A summary if their instrument characterisation is included below.

TABLE 1. AMSU-A channel characteristics.

Channel No.	Center frequency	No. of pass bands	Bandwidth (MHz)	Center frequency stability (MHz)	Temperature sensitivity (K) NEΔT	Calibration accuracy (K)	Angle θp
1	23 800 MHz	1	270	10	0.3	2.0	V
2	31 400 MHz	1	180	10	0.3	2.0	V
3	50 300 MHz	1	180	10	0.4	1.5	V
4	52 800 MHz	1	400	5	0.25	1.5	V
5	53 596 ± 115 MHz	2	170	5	0.25	1.5	H
6	54 400 MHz	1	400	5	0.25	1.5	H
7	54 940 MHz	1	400	5	0.25	1.5	V
8	55 500 MHz	1	330	10	0.25	1.5	H
9	57 290.344 MHz = f <sub>LO</sub>	1	330	0.5	0.25	1.5	H
10	f <sub>LO</sub> ± 217 MHz	2	78	0.5	0.4	1.5	H
11	f <sub>LO</sub> ± 322.2 ± 48 MHz	4	36	1.2	0.4	1.5	H
12	f <sub>LO</sub> ± 322.2 ± 22 MHz	4	16	1.2	0.6	1.5	H
13	f <sub>LO</sub> ± 322.2 ± 10 MHz	4	8	0.5	0.80	1.5	H
14	f <sub>LO</sub> ± 322.2 ± 4.5 MHz	4	3	0.5	1.20	1.5	H
15	89.0 GHz	1	6 000	50	0.5	2.0	V

Figure 3-6: AMSU-A channel characterisation after Li2000

TABLE 4. The coefficients for HIRS/3 and AMSU-A bias adjustment.

HIRS/3 channel index	Slope (a)	Intercept (b)	AMSU-A channel index	Slope (a)	Intercept (b)
1	0.8174493	43.99188	1*	1.000000	0.000000
2	0.8523166	33.75825	2*	1.000000	0.000000
3	0.8648131	30.56179	3*	1.000000	0.000000
4	1.0282290	-5.48383	4	1.020023	-7.771476
5	0.9877007	3.67346	5	1.021792	-6.488478
6	0.9748163	6.59699	6	1.007780	-1.506610
7	0.9582583	10.52518	7	1.039344	-8.765779
8	0.9191831	22.30155	8	0.938334	13.424830
9*	1.0000000	0.00000	9	0.941926	12.654100
10	0.9327897	18.65043	10	0.932548	14.924470
11	0.8976258	25.74048	11	0.918347	18.666970
12	0.9241955	18.96372	12	0.880986	28.549870
13	0.9596393	9.64674	13	0.754574	60.506610
14	0.9852950	3.13180	14	0.682403	81.671510
15	0.9839523	2.04826	15*	1.000000	0.000000
16	0.9921560	0.15154			
17	0.9578910	11.42773			
18	0.9329234	16.59371			
19	0.9020007	24.08484			

\* Bias adjustment is not applicable for those channels.

Figure 3-7: Bias adjustment coefficients for the AMSU-A channels after Li2000

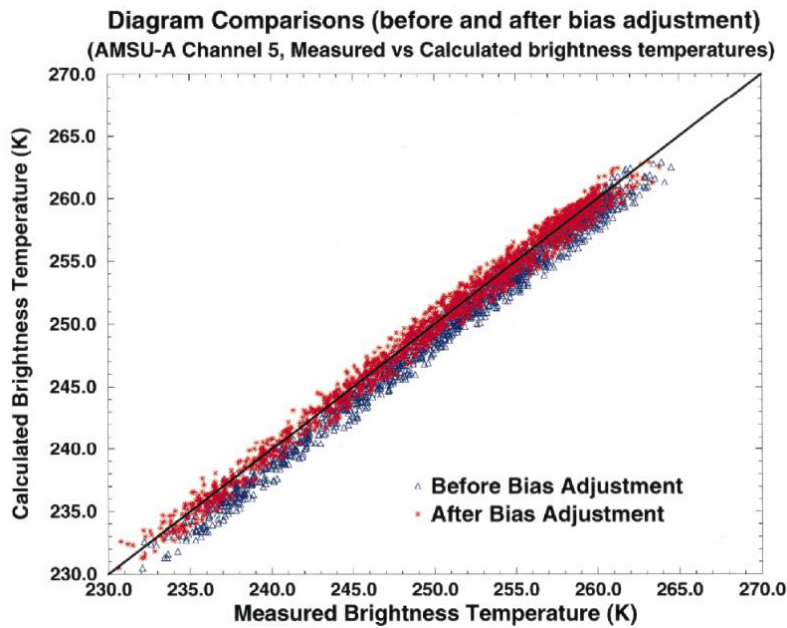


Figure 3-8: Result of bias correction for AMSU channels using the coefficients from the Table above (Li2000)

#### MCKAGUE 2001

McKague, Darren S., R. J. Engelen, J. M. Forsythe, S.Q. Kidder, and T. H. Vonder Haar, 2001: An Optimal-Estimation Algorithm for Water Vapor Profiling using AMSU. Proc. of 11th Conf. On Sat. Meteor. and Ocean, 633-636.

This is the algorithm description paper leading up to McKague2003, an optimal estimation retrieval scheme for humidity profiling of AMSU-A and AMSU-B data. This paper is based on simulated measurements only, although it also lists measurement errors for the AMSU-A and AMSU-B instruments. In fact it gives more details about the algorithm setup than the follow up paper McKague2003 which deals with real measurements.

The algorithm presented here simultaneously retrieves temperature profiles, water vapour profiles and surface emissivities, which is shown here to lead to more accurate water vapour retrievals.

The measurement errors (or observational errors) used by the authors are random errors based on the NEBT of the AMSU channels listed in their first Table. They didn't specify any errors on the forward model, arguably because this is a simulation study only. The error on the a priori profiles are listed in their second Table. The third table specifies the improvement in water vapour profile retrieval from adding temperature, and then temperature and surface emissivity to the state vector (i.e. the vector containing all retrieved parameters).

Importantly, the authors are treating all AMSU channels as uncorrelated, which may be overly simplistic.

	Channel	Frequency (GHz)	NEDT (K)
AMSU-A	1	23.8	0.3
	2	31.4	0.3
	3	50.3	0.4
	4	52.8	0.25
	5	53.596 ± .115	0.25
	6	54.4	0.25
	7	54.94	0.25
	8	55.5	0.25
	9	57.290344 = $f_0$	0.25
	10	$f_0 \pm .217$	0.4
	11	$f_0 \pm .3222 \pm .048$	0.4
	12	$f_0 \pm .3222 \pm .022$	0.6
	13	$f_0 \pm .3222 \pm .010$	0.8
	14	$f_0 \pm .3222 \pm .0045$	1.2
	15	89.0	0.5
AMSU-B	1	89.0	0.8
	2	150.0	0.8
	3	183.31 ± 1.0	0.8
	4	183.31 ± 3.0	0.8
	5	183.31 ± 7.0	0.8

Figure 3-9: Channel specifications after McKague2001. The observation errors in their simulation study is pure random noise based on the NEBT in this table

Parameter	Std. Deviation	Source
Water Vapor Mixing Ratio	0.0005-2.1 g/kg (see figure 2)	English (1999)
Temperature	3.0 K	Nutter et al. (1999)
Emissivity	.01	2 m/s wind speed and 3.0 K surface temperature uncertainty

Figure 3-10: A priori errors used in the optimal estimation retrieval in McKague2001.

Data	Retrieval Type	Mean RMS Error (g/kg)	Mean Abs. Bias (g/kg)	Max. Abs. Bias (g/kg)
AMSU-B	Water Vapor Only	.33	.08	.20
	Water Vapor + Temperature	.28	.06	.19
	Vapor + Temp + Emissivity	.23	.03	.08
AMSU-B and AMSU-A	Water Vapor Only	.37	.10	.32
	Vapor + Temperature	.25	.03	.11
	Vapor + Temp + Emissivity	.18	.02	.06

Figure 3-11: This table illustrates the improvements in water vapour profile retrievals when adding temperature and surface emissivity to the retrieval state vector.

MCKAGUE 2003

McKague, Darren S., and A. S. Jones. "A passive microwave optimal-estimation algorithm for near real-time water vapor profiling." Proceedings of the 11th Conference on Satellite Meteorology and Oceanography. 2003.

In this proceedings paper the authors describe a classical optimal estimation retrieval setup according to Rodgers. A variety of parameters can be retrieved including profiles of water vapour mixing ratio, joint water vapour and temperature profiles (including surface temperature), and water vapour and temperature profiles along with microwave ave surface emissivities. The authors give a table with instrument parameters for AMSU-A and AMSU-B as used in their retrieval setup. This includes a column of NEBT for each channel of AMSU-A and AMSU-B.

Most interestingly, the NEBT values for AMSU-B have been updated (i.e. Increased from 0.8K to 2K) in this work as compared to a previous publication by the same authors (see McKague2001). The channel specification for AMSU-A are unchanged.

Similar to their previous work, there is no forward model error explicitly considered, and the AMSU channels are treated as uncorrelated. AMSU-B measurements have been averaged to the scale of AMSU-A observations before being input to the retrieval algorithm. The authors perform a retrieval based real measurements and compare it to a reference retrieval scheme (The algorithm was tested on simulations in past work). The comparison to the existing scheme is good, and the authors claim that their scheme is fast enough to run in real time.

	Channel	Frequency (GHz)	NEDT (K)
AMSU-A	1	23.8	0.3
	2	31.4	0.3
	3	50.3	0.4
	4	52.8	0.25
	5	53.596 ± . 115	0.25
	6	54.4	0.25
	7	54.94	0.25
	8	55.5	0.25
	9	57.290344 = f <sub>0</sub>	0.25
	10	f <sub>0</sub> ± . 217	0.4
	11	f <sub>0</sub> ± . 3222 ± .048	0.4
	12	F <sub>0</sub> ± . 3222 ± .022	0.6
	13	f <sub>0</sub> ± . 3222 ± . 010	0.8
	14	F <sub>0</sub> ± . 3222 ± .0045	1.2
	15	89.0	0.5
AMSU-B	1	89.0	2.0
	2	150.0	2.0
	3	183.31 ± 1.0	2.0
	4	183.31 ± 3.0	2.0
	5	183.31 ± 7.0	2.0

Figure 3-12: AMSU channel characterisation in McKague 2003. Note that the AMSU-B channel NEBTs have been increased from McKague2001.

MITRA 2010

MITRA, A. K.; KUNDU, P. K.; SHARMA, A. K. y ROY BHOWMIK, S. K.. A neural network approach for temperature retrieval from AMSU-A measurements onboard NOAA-15 and NOAA-16 satellites and a case study during Gonu cyclone. *Atmosfera* [online]. 2010, vol.23, n.3, pp. 225-239. ISSN 0187-6236.

#### ABSTRACT

*A neural network (NN) technique is used to obtain vertical profiles of temperature from NOAA-15 and 16 Advanced Microwave Sounding Unit-A (AMSU-A) measurements over the Indian region. The corresponding global analysis data generated by National Center for Environmental Prediction (NCEP) and AMSU-A data from July 2006 to April 2007 are used to build the NN training data-sets and the independent dataset of May 2007 to July 2007 divided randomly into two independent dataset for training (land) and testing (ocean). NOAA-15 and 16 satellite data has been obtained in the form of level 1b (instrument counts, navigation and calibration information appended) format and pre-processed by ATOVS (Advanced TIROS Operational Vertical Sounder) and AVHRR (Advanced Very High Resolution Radiometer) Processing Package (AAPP). The root mean square (RMS) error of temperature profile retrieved with the NN is compared with the errors from the International Advanced TOVS (ATOVS) Processing Package (IAPP). The over all results based on the analysis of the training and independent datasets show that the quality of retrievals with NN provide better results over the land and comparable over the ocean. The RMS errors of NN are found to be less than 3 deg C at the surface, 0.9 deg to 2.2 deg between 700 and 300 hPa and less than 2 deg C between 300 and 100 hPa. It has also been observed that the NN technique can yield remarkably better results than IAPP at the low levels and at about 200-hPa level. Finally, the network based AMSU-A 54.94-GHz (Channel-7) brightness temperature (maximum  $T_b$ ) and its warm core anomaly near the center of the cyclone has been used for the analysis of Gonu cyclone formed over Arabian Sea during 31 May to 7 June 2007. Further, the anomalies are related to the intensification of the cyclone. It has been found that the single channel AMSU-A temperature anomaly at 200 hPa can be a good indicator of the intensity of tropical cyclone. Therefore it may be stated that optimized NN can be easily applied to AMSU-A retrieval operationally and it can also offer substantial opportunities for improvement in tropical cyclone studies.*

This is another paper on a neural network type of retrieval algorithm for AMSU-A temperature measurements solely. It is one of the most recent papers on AMSU processing. The authors claim that their neural network approach yields better results over land, and comparable results over ocean than the operational processor. They have tested their retrieval in a case study of cyclone over the Arabian see.

The authors mention a temperature anomaly in AMSU-A channel 7 (54.94 GHz), which changes as a function of cyclone intensity, making this channel useful for the detection of cyclone strength. This could be something to keep in mind should we encompass problems in the temperature retrievals from this channel.

The results of the neural network retrievals are compared to the IAPP processor, described in Li2000. The neural network is said to be superior to the physical retrieval in many cases because it doesn't depend on a forward model and its related error, and neither does it depend on the surface properties. The physical retrieval however is more generally applicable, and will also perform in extreme atmospheric conditions.

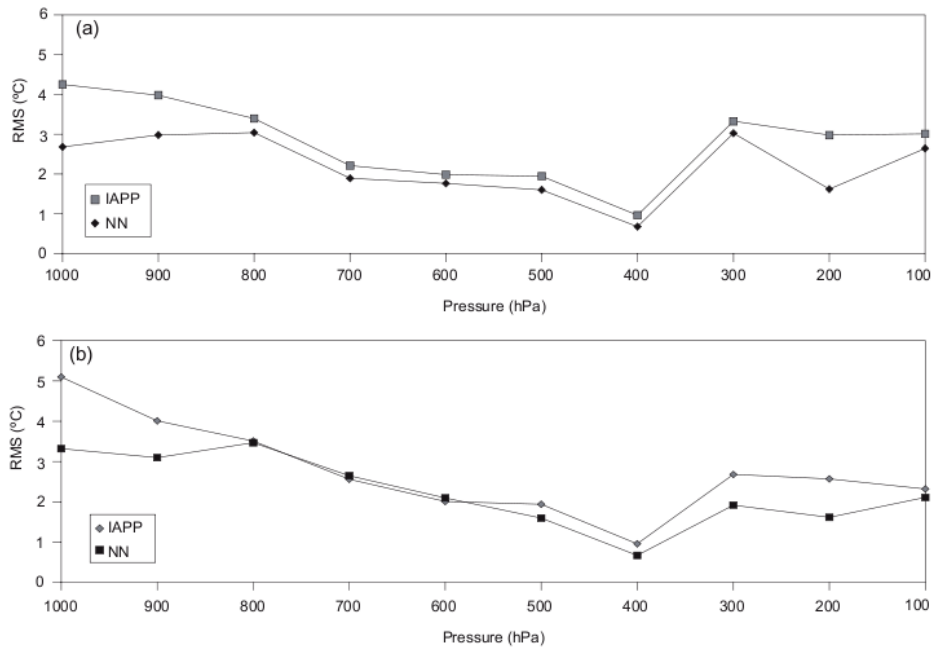


Fig. 2. The RMS errors retrieval of neural network and IAPP. (a) Over the land and (b) over the ocean, both for the months of May 2007 to July 2007.

**Figure 3-13: Table 1: RMS errors of Mitra2010 vs the IAPP processor of Li2000 (this is an OEM algorithm). The reference is the NCEP database**

OLSEN 2008

E. T. Olsen, , S.-Y. Lee, , J. Susskind, J. Blaisdell, L. Iredel, AIRS/AMSU/HSB Version 5 Modification of Algorithm to Account for Increased NeDT in AMSU Channel 4 , JPL Technical Report, Version 1.1.1., February 2008, California Institute of Technology

*Abstract*

*The AIRS Science Team Version 5 AIRS/AMSU retrieval algorithm includes use of observations of AMSU-A channel 4. This channel had an instrumental NEDT of 0.14K at launch. AMSU-A channel 4 NEDT remained stable at this value until August 2007, at which time the channel noise began to increase. The Goddard DAAC operational AIRS/AMSU Version 5 retrieval algorithm assumes the at-launch value for AMSU-A channel 4 NEDT. As channel 4 noise increased from this value, the performance of the Version 5 retrieval algorithm began to degrade, both in terms of the percentage of acceptable retrievals as well as the accuracy of the accepted retrievals.*

This is an internal note from the AIRS Science Team at JPL documenting a modification in their V5 data analysis algorithm which corrects for the increase in noise (Tsys) of the AMSU channel No. 4. The launch NEDT of 0.14K for channel 4 remained stable until 20078, from which it degenerated sharply.

The correction was done by using linear regression to estimate the channel 4 radiance from the radiances of the other channels. The thus corrected channel 4 radiances were used as normal in the operational AMSU processor. It's deemed possible to use linear regression to infer one channel from others because the information content is spread over all channels.

The authors don't provide an updated measurement error for the affected channel, rather do they

modify the measurements themselves so that they are compatible again with the original measurement noise definition. This is done by the application of so called microwave tuning coefficients (documented separately in the AIRS Science Team ATBD). They claim to have chosen this approach so as to have minimal disturbance to the existing algorithm (for backward compatibility). For the purpose of our own study, we should make sure that we are using an up to date version of AMSU level1b data.

One other interesting point is that antenna pattern distortions affect the channels in different manners."It can be seen that the antenna pattern distortion makes the observed values of AMSU-A channel 4 colder than they should be by values ranging from about 1.2K near nadir to values greater than 2.0K at large satellite zenith angles. Similar antenna pattern distortions are observed in the other AMSU-A channels."

The team conclude that: "AMSU channel 4 is indeed providing very little information about surface and atmospheric conditions not already contained in the remaining AMSU-A observations." They use channel 4 mainly for cloud clearing of measurements.

---

#### JOHN 2008

Viju Oommen John, Retrieval of Atmospheric Parameters from AMSU, Seminar at Institute of Environmental Physics, University of Bremen, 2008

This is not a peer reviewed publication, but rather the internet published slides from an institute seminar given at Uni Bremen. It is however of interest to include this work in our review, because the authors present the full error correlation matrix for temperature used in their Optimal Estimation retrieval of AMSU data. We have not found this in any Optimal Estimation retrieval paper published in the peer reviewed literature. They mention that they also have a covariance matrix for water vapour, but this one is not shown in the presentation.

The presentation also includes their averaging kernels for temperature and water vapour, as well as retrieval results for various scenarios. The scenarios are of increasing complexity. They consist of simple retrievals of water vapour profiles, and then look at the impact of temperature on the humidity profiles. Simple retrievals of temperature are complemented with joint retrievals of water vapour, and then water vapour and surface emissivity in a similar fashion as is planned for our own study. There are also some results of simulations without cloud filtering, and with a purely diagonal error covariance matrix. Because this is just a presentation, the text on the interpretation of the results is minimal and not always conclusive.

The conclusions of the authors from their OEM retrieval of atmospheric parameters from AMSU are summarised as follows:

- Atmospheric parameters can be retrieved from AMSU data using Optimal Estimation Method (OEM)
- Good knowledge of temperature (simultaneous retrieval) is necessary for the retrieval of water vapour
- Emissivity should be retrieved along with temperature
- Full covariance matrix should be used for better retrieval
- Clouds do not make significant changes in the retrieval of temperature

## ROSENKRANZ 2001

Philip W. Rosenkranz, Retrieval of Temperature and Moisture Profiles From AMSU-A and AMSU-B Measurements, IEEE TRANSACTIONS ON GEOSCIENCE AND REMOTE SENSING, VOL. 39, NO. 11, pp2429, NOVEMBER 2001

*Abstract—The NOAA-15 weather satellite carries the Advanced Microwave Sounding Units-A and -B (AMSU-A, AMSU-B) which measure thermal emission from an atmospheric oxygen band, two water lines, and several window frequencies. An iterated minimum-variance algorithm retrieves profiles of temperature and humidity in the atmosphere from this data. Relative humidity is converted into absolute humidity with use of the retrieved temperature profile. Two important issues in the retrieval problem are modelling of the surface and clouds. An a priori surface emissivity is computed on the basis of a preliminary classification, and the surface brightness spectrum is subsequently adjusted simultaneously with the moisture profile retrieval. Cloud liquid water is constrained by a condensation model that uses an extended definition of relative humidity as a parameter.*

The authors present a complex combined algorithm to retrieve water vapour profiles, temperature profiles and surface parameters from AMSU-A and AMSU-B data. Apart from the radiative transfer model, they also use a surface brightness model and an atmospheric moisture and condensation model which provide an improved first guess for the Optimal Estimation retrieval of atmospheric profiles.

The data processing algorithm is iterative in itself, and the bare-bone structure can be broken down into the following 5 steps:

- 1) Based on location and month, choose an a priori temperature profile. At present the a priori relative humidity is global. Also calculate the geomagnetic field, which has a minor effect on the transmittance of channel 14.
- 2) Using location or other criteria, classify the surface as discussed in Section II-B. Compute an a priori surface brightness temperature for this class. This will depend on surface temperature.
- 3) Test for convergence of channels 1, 2, 3, 15, and 17–20 brightness temperatures. If not converged, update the humidity profile and the surface brightness temperature spectrum using these channels.
- 4) Test for convergence of channels 4–14. If not converged, update the temperature profile using these channels.
- 5) Return to step 2 if convergence did not occur in step 4; else to step 3 if convergence did not occur in step 3; else exit.

Because of the contamination of AMSU-B spectra by spurious signals from other emitters, the AMSU-B analysis was restricted to a test period during which these interfering signal had been temporarily switched off. Furthermore, to compensate for the higher ground-pixel resolution of the high frequency channels, the AMSU-B measurements have been averaged to match the corresponding AMSU-A footprint.

The measurement errors are given by the authors in their Table 1 (labelled “Sensitivity”). The error

covariance matrix is not given, but there is a short mention in the text that indicates the presence of non-zero off-diagonal elements, namely: "A priori statistics are required for the parameters that characterize the state of the system. However, statistical correlations between temperature and relative humidity are not allowed to influence the retrieved profiles. Temperature is retrieved from the oxygen-band channels 4–14 and moisture and surface parameters from the water-vapor and window channels. Hence only radiative-transfer influences (e.g., water-vapor continuum absorption and surface emissivity in the oxygen band) link different parameters in the retrieval."

---

#### SUSSKIND 1998

J. Susskind, C. Barnett and J. Blaisdell, DETERMINATION OF ATMOSPHERIC AND SURFACE PARAMETERS FROM SIMULATED AIRS/AMSU/HSB SOUNDING DATA: RETRIEVAL AND CLOUD CLEARING METHODOLOGY, *Adv. Space Res.*, Vol. 21, No. 3, pp. 369-384, 1998

#### ABSTRACT

*New state of the art methodology is described to analyze AIRS/AMSU/HSB data in the presence of multiple cloud formations. The methodology forms the basis for the AIRS Science Team algorithm which will be used to analyze AIRS/AMSU/HSB data on EOS PM 1. The cloud clearing methodology requires no knowledge of the spectral properties of the clouds. The basic retrieval methodology is general and extracts the maximum information from the radiances, consistent with the channel noise covariance matrix. The retrieval methodology minimizes the dependence of the solution on the first guess field and does not require modelling or knowledge of the first guess error characteristics. Results are shown for AIRS Science Team simulation studies with multiple cloud formations. These simulation studies imply that temperature soundings can be produced under partial cloud cover with RMS errors better than 1°K in 1 km thick layers from the surface to 700 mb, 1 km layers from 700 mb to 300 mb, 3 km layers from 300 mb to 30 mb, and 5 km layers from 30 mb to 1 mb, and moisture profiles can be obtained with an accuracy of about 10% absolute errors in 1 km layers from the surface to 200 mb.*

This is the initial publication describing the AIRS Science Team algorithm for the analysis of AMSU data (see e.g. Olsen2008 for updates of the same algorithm). The paper discusses the influence of clouds on the channel error covariance matrix, which plays an important role in the Optimal Estimation retrievals.

The cloud clearing algorithm used in this paper is based on the approach to correct the radiance in a given pixel to correct for the effects of cloud, and then perform a retrieval with a radiative transfer model that doesn't have to try to simulate the radiative properties of clouds. This means that the measurement error covariance matrix used in this paper is comprised of two terms: An instrumental error part depending on the channel noise temperatures, and a second part related to the cloud clearing errors. No explicit numbers are given for the error covariance matrix however, so we probably can't use this as a reference for our own study.

---

#### SUSSKIND 2003

Joel Susskind, Christopher D. Barnet, and John M. Blaisdell, Retrieval of Atmospheric and Surface Parameters From AIRS/AMSU/HSB Data in the Presence of Clouds, *IEEE TRANSACTIONS ON GEOSCIENCE AND REMOTE SENSING*, VOL. 41, NO. 2, FEBRUARY 2003

### Abstract

*New state-of-the-art methodology is described to analyze the Atmospheric Infrared Sounder/Advanced Microwave Sounding Unit/Humidity Sounder for Brazil (AIRS/AMSU/HSB) data in the presence of multiple cloud formations. The methodology forms the basis for the AIRS Science Team algorithm, which will be used to analyze AIRS/AMSU/HSB data on the Earth Observing System Aqua platform. The cloud-clearing methodology requires no knowledge of the spectral properties of the clouds. The basic retrieval methodology is general and extracts the maximum information from the radiances, consistent with the channel noise covariance matrix. The retrieval methodology minimizes the dependence of the solution on the first-guess field and the first-guess error characteristics. Results are shown for AIRS Science Team simulation studies with multiple cloud formations. These simulation studies imply that clear column radiances can be reconstructed under partial cloud cover with an accuracy comparable to single spot channel noise in the temperature and water vapor sounding regions; temperature soundings can be produced under partial cloud cover with RMS errors on the order of, or better than, 1 K in 1-km-thick layers from the surface to 700 mb, 1-km layers from 700–300 mb, 3-km layers from 300–30 mb, and 5-km layers from 30–1 mb; and moisture profiles can be obtained with an accuracy better than 20% absolute errors in 1-km layers from the surface to nearly 200 mb.*

The authors present a retrieval scheme for the analysis of AIRS, AMSU-A and HSB (which is said to be similar to AMSU-B). This paper is a refinement of the methodology first described in Susskind1998.

These simulation studies imply that clear column radiances can be reconstructed under partial cloud cover with an accuracy comparable to single spot channel noise in the temperature and water vapour sounding regions; temperature soundings can be produced under partial cloud cover with RMS errors on the order of, or better than, 1 K in 1-km-thick layers from the surface to 700 mb, 1-km layers from 700-300 mb, 3-km layers from 300-30 mb, and 5-km layers from 30-1 mb; and moisture profiles can be obtained with an accuracy better than 20% absolute errors in 1-km layers from the surface to nearly 200 mb.

Most importantly for the purpose of our study, they present a cloud clearing algorithm that is said to work well for the combined analysis of IARS/AMSUX data. No spectral knowledge of cloud parameters are required. There is however not much information on the treatment of AMSU measurements (i.e. Sy) found in this paper either.

---

### VANGASSE 1996

P. Vangasse, J. Charlton and M. Jarrett , CHARACTERISATION OF THE ADVANCED MICROWAVE SOUNDING UNIT, AMSU-B , Adv.Space Res. Vol. 17, No. 1, pp. (1)75-(1)78, 1996.

### ABSTRACT

*The Advanced Microwave Sounding Unit, AMSU-B, is a five channel microwave radiometer to be flown later this decade on the series of polar orbiting spacecraft NOAA-K, L and M . It will provide global data in support of synoptic weather forecasting by sounding the water vapour content of the atmosphere from the 'window' channels at 89 and 150 GHz to the strong resonance line at 183.3 GHz. It has a scan period of 22/3 seconds and provides 90 earth view pixels each of nominal beam width 1.1 degrees during earth scan. The key radiometric requirements of the instrument are to provide a temperature sensitivity of 1 to 1.2K depending on channel, a linearity within 0.3 of the temperature sensitivity and a beam efficiency of 95%. This paper describes the design of the AMSU-B, the ground based buy-off tests and results obtained for the Proto-Flight Model (PFM), Flight 2 (FM2)*

and Flight 3 (FM3) Models in the context of these requirements. The Engineering Model testing is described in reference /1/.

This paper gives a comprehensive overview of the instrument specification of AMSU-B. This includes the individual channel noise temperatures (NEBT), but also the channel linearity, as well as results from antenna pattern measurements. Thermal tests were performed at DRA Farnborough by the UK Met Office, and antenna measurements were done at Queen Mary College, London. The numbers presented here are a useful reference for the determination of the measurement error covariance matrix, be it for the thermal noise error component only.

The values of NEBT for AMSU-B channels are similar to those presented in McKague2001, however McKague et. al. Have escalated their numbers in a subsequent publication McKague2003, so some reservations will have to apply here.

**TABLE 2** Measured temperature sensitivities, worst case

SPECIFICATION:	CHANNEL $\Delta T$ (K)				
	16	17	18	19	20
RESULTS: PFM	0.42	0.88	1.14	0.77	0.7
FM2	0.41	0.82	0.83	0.75	0.8
FM3	0.44	0.56	0.94	0.88	0.84

**LINEARITY**

**Figure 3-14: Pre-flight AMSU-B channel noise temperatures by Vangasse1996**

**WU 2001**

X. Wu, L. Lavanat, F. Zhang, M. Ran and P. Brunel, RETRIEVING ATMOSPHERIC TEMPERATURES FROM NOAA-15 ATOVS MEASUREMENTS, ACTA METEOROLOGICA SINICA, Vol. 15, No. 4, 2001

The authors describe an iterative, non-linear retrieval system based on a Optimal Estimation algorithm for the analysis of ATOVS data. The authors are based at the National Satellite Meteorological Centre in China. The NSMC are running their own pre-processing of ATOVS data with the AAPP package, with some unspecified adaptations “according to the local situation”. The AAPP was updated with the latest corrections for IARS and AMSU. The forward model used is RTTOV.

The authors point out that due to the overlapping weighting functions the acquisition of realistic first guess profiles is important for the quality of the retrieval. In the presented work, the first guess profiles are derived from a 10 day rolling average based on the Chinese regional NWP HLAFS (High-resolution Limited Area Forecasting System). The retrieval algorithm itself is classical OEM approach after Rodger.

The paper includes tabulation errors of RTTOV calculations and observations for a ten day period between 21 and 30 August 1999 for NOAA-15 over land. The errors are calculated at 40 levels and 40 ATOVS channels (channels 21-35 are the 15 AMSU-A channels, channels 36-40 are the 5 AMSU-B channels). These give a more comprehensive picture of the real noise performance of the ATOVS channels than pure NEBT numbers.

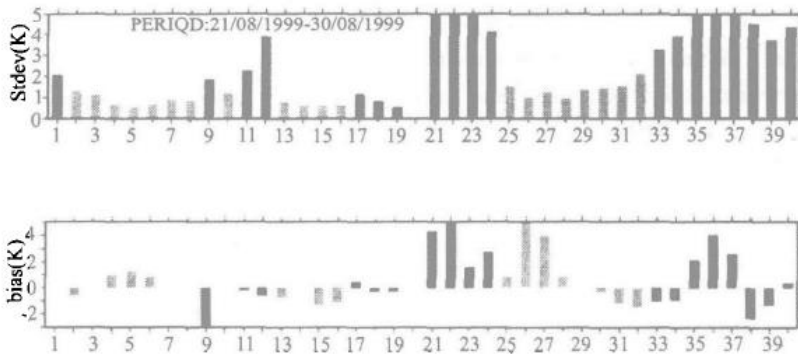


Fig. 2. RTTOV brightness temperature deviations for 40 channels of NOAA15 over land. 40 ATOVS channels are indicated in the X axis.

**Figure 3-15: Errors of RTTOV calculations vs. observations for a 10 day period in August 1999. These "real life" errors could be more indicative of measurement errors than pure NEBT values.**

EYRE 1989

Eyre, J. R., 1989: Inversion of cloudy satellite sounding radiances by nonlinear optimal estimation. I: Theory and simulation for TOVS. Quart. J. Roy. Meteor. Soc., 115, 1001–1026

This two-part Publication (Part II is on application to real TOVS data) gives the first characterisation of MSU (and HIRS) channel noise performance used to calculate the error covariance matrix, and also a set of state vector variances used to calculate the a priori covariance matrix. Numbers are for the original MSU, not the advanced AMSU.

TABLE 1. DATA USED TO CONSTRUCT THE MEASUREMENT ERROR COVARIANCE

Channel	Radiometric error, $\epsilon^r$ (HIRS in $mW m^{-2} sr^{-1} (cm^{-2})^{-1}$ ) (MSU in K)	Forward model error, $\epsilon^m$ , in brightness temperature (K)
HIRS-1	0.62	0.2
-2	0.13	0.2
-3	0.11	0.2
-4	0.068	0.2
-5	0.048	0.2
-6	0.056	0.2
-7	0.040	0.2
-8	0.019	0.2
-9	0.023	0.2
-10	0.026	0.2
-11	0.040	0.2
-12	0.030	0.2
-13	0.0010	0.2
-14	0.00092	0.2
-15	0.00080	0.2
-16	0.00055	0.2
-17	0.00063	0.2
-18	0.00037	0.2
-19	0.00020	0.2
MSU-1	0.17	0.2
-2	0.15	0.2
-3	0.18	0.2
-4	0.18	0.2

**Figure 3-16: Radiometric and forward model errors for the computation of the observation error covariance matrix after Eyre1989.**

## CHOU 2004

HIEN-BEN CHOU and HUEI-PING HUANG, A new procedure for estimating observation errors in AMSU data and its application to retrieval, Q. J. R. Meteorol. Soc. (2004), 130, pp. 79–101

**SUMMARY**

*An accurate estimate of observation errors is crucial to the retrieval of atmospheric profiles from satellite data using a variational method. In practice, observation errors, both systematic and random, are often estimated from the difference between satellite observations and simulated satellite observations obtained from a radiative-transfer operator with a 12 h forecast as its input. Observation errors estimated by this approach may be contaminated by errors in the 12 h forecast. This work describes a practical way to eliminate the 12 h forecast error and improve the estimate of the observation error in the Advanced Microwave Sounding Unit (AMSU) data. Following the philosophy of the National Meteorological Center (NMC) method (that derives the statistics of forecast error from the differences between pairs of forecasts at disparate ranges valid at the same time), in this study the pairs of forecasts at different ranges in the NMC method are first converted to brightness temperatures in the AMSU channels by a radiative-transfer operator. The 12 h forecast errors are then determined from the representations of these forecasts in radiance space spanned by the AMSU channels. Since most AMSU channels have beam position-dependent systematic observation errors, the procedure further takes into account this dependence by performing the statistics separately for sub-groups of data in each AMSU channel with different beam positions. In a case-study, after eliminating the 12 h forecast error obtained by this procedure from the total estimated observation error, the remaining random error of the satellite observation is shown to be smaller than the background error (provided by 12 h forecasts of a numerical weather-prediction model) in most of the AMSU temperature sounding channels. Using the error-corrected AMSU data in these channels, a retrieval experiment using a one-dimensional variational scheme shows an improvement of 0.2–0.4 K over the background error in the retrieved temperature profiles above 780 hPa.*

The authors from the Central Weather Bureau in Taipei are using a 1D variational approach to retrieve atmospheric profiles from ATOVS data. The variational method has recently become widely used for retrieving atmospheric profiles from satellite data and for assimilating satellite data into numerical weather prediction systems (the meteorology background of the authors clearly shows here). In the variational approach, the ratio between background error and observation error crucially determines the weight given to the observations.

In general, the results of retrieval or data assimilation, by a variational method or any other optimization approach, improve with more accurate estimates of the observation and background errors. Eyre (1989) showed that the results of retrieval are more strongly affected by the change in the inter-level correlation of the background-error matrix than that in the observation error. However, in his simulation study it is assumed that the observation has no bias. As the observation error includes random and systematic components, it is necessary to remove the systematic error and obtain an accurate estimate of the random error for the use in retrieval.

In previous studies (Eyre 1992; English et al. 2000), the differences between observations and simulated observations calculated from a radiative-transfer model with short-range forecast profiles as inputs are used to construct the statistics of observation error. In such a procedure, the error in the short-term NWP forecast would inevitably contaminate the estimate of the observation error. The focus of this paper is the quantification and mitigation of this contamination.

The background-error covariance matrix  $B$  was constructed from statistics of the differences between analyses and 12 h forecasts (valid at the same time). The statistics of the differences between observation and simulated observation are used to remove the systematic component (bias) of satellite observation error and to construct the  $E$  matrix.

The authors go one step beyond other publications in that they calculate the measurement errors not only for each channel, but also for each antenna angle in the across-track scan individually. This results in a large number of results, especially since they also give tables for the slopes and intercepts for the channel bias corrections, again tabulated by channel and antenna beam position.

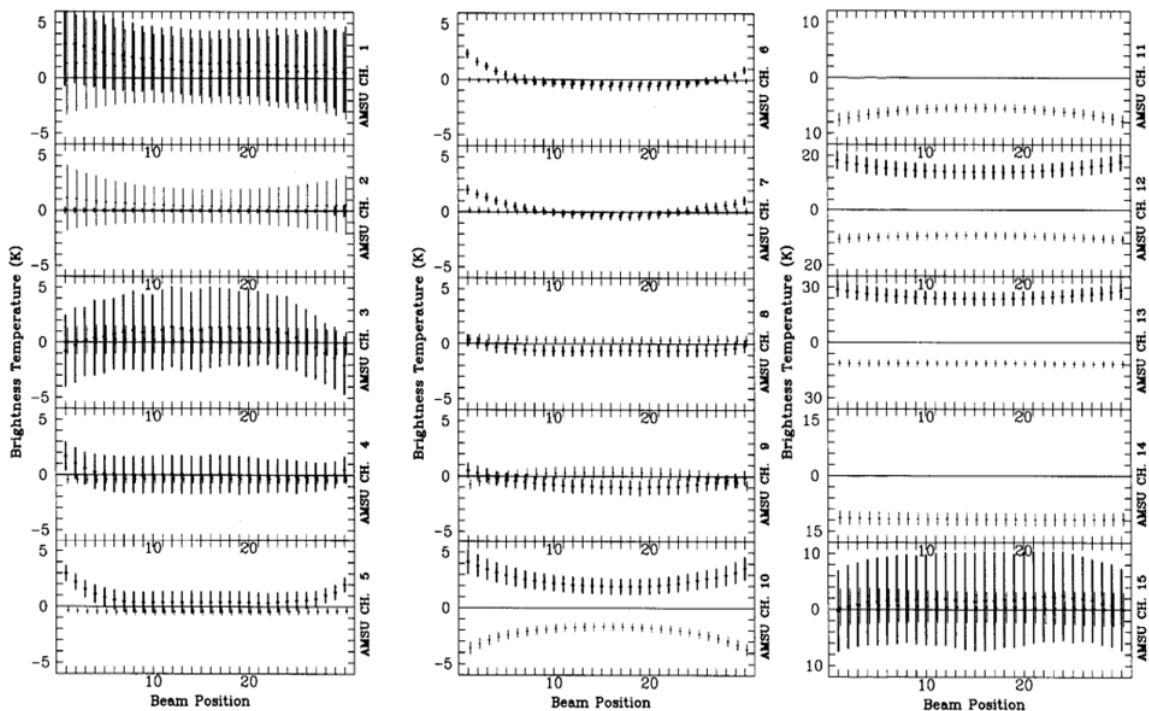


Figure 3-17: The estimated observation errors (thick lines) and 12 h forecast errors (thin lines) in radiance space in the AMSU channels. The short horizontal bar represents the systematic error, the length of the vertical stick the random error. The beam position is indicated in the abscissa.

TABLE 3. STANDARD DEVIATION OF ERROR (K) IN MEASUREMENTS AND RADIATIVE-TRANSFER MODEL USED IN THIS WORK

Beam position	AMSU channel									
	4	5	6	7	8	9	10	12	13	
1	0.91	0.41	0.12	0.06	0.04	0.18	0.52	1.36	2.27	
2	1.02	0.41	0.09	0.06	0.04	0.14	0.48	1.32	2.19	
3	1.08	0.45	0.10	0.06	0.05	0.12	0.46	1.30	2.14	
4	1.18	0.50	0.11	0.07	0.06	0.11	0.44	1.29	2.10	
5	1.23	0.54	0.12	0.08	0.08	0.10	0.42	1.25	2.03	
6	1.23	0.57	0.13	0.08	0.09	0.11	0.40	1.23	1.97	
7	1.24	0.59	0.14	0.09	0.09	0.09	0.38	1.19	1.92	
8	1.24	0.60	0.15	0.09	0.09	0.07	0.34	1.17	1.88	
9	1.26	0.63	0.16	0.10	0.09	0.07	0.33	1.15	1.85	
10	1.25	0.62	0.15	0.10	0.09	0.07	0.32	1.13	1.83	
11	1.29	0.64	0.16	0.10	0.09	0.06	0.31	1.13	1.81	
12	1.29	0.64	0.17	0.11	0.10	0.06	0.30	1.12	1.79	
13	1.31	0.65	0.18	0.10	0.10	0.07	0.29	1.11	1.77	
14	1.28	0.66	0.17	0.10	0.11	0.07	0.29	1.11	1.77	
15	1.27	0.63	0.16	0.10	0.10	0.07	0.30	1.11	1.76	
16	1.33	0.66	0.17	0.10	0.11	0.08	0.29	1.09	1.75	
17	1.29	0.64	0.15	0.10	0.11	0.08	0.30	1.09	1.75	
18	1.26	0.62	0.15	0.10	0.11	0.09	0.31	1.09	1.76	
19	1.29	0.66	0.16	0.10	0.12	0.10	0.31	1.07	1.74	
20	1.24	0.62	0.15	0.09	0.14	0.12	0.32	1.06	1.72	
21	1.16	0.59	0.15	0.10	0.14	0.11	0.33	1.07	1.73	
22	1.06	0.54	0.14	0.10	0.14	0.12	0.33	1.06	1.72	
23	1.10	0.53	0.12	0.10	0.14	0.12	0.34	1.07	1.73	
24	1.06	0.51	0.12	0.09	0.14	0.12	0.36	1.08	1.76	
25	1.08	0.50	0.11	0.08	0.13	0.13	0.38	1.10	1.80	
26	0.96	0.43	0.08	0.08	0.12	0.11	0.39	1.13	1.86	
27	0.91	0.40	0.08	0.07	0.11	0.11	0.40	1.15	1.93	
28	0.84	0.37	0.06	0.06	0.09	0.11	0.42	1.18	2.00	
29	0.83	0.37	0.05	0.04	0.08	0.12	0.45	1.23	2.07	
30	0.81	0.38	0.05	0.03	0.06	0.15	0.50	1.33	2.23	

Figure 3-18: Estimated measurement and forward model errors for a select number of AMSU channels used in this study, also as a function of beam position. These numbers are higher than the NEBT figures for each channel, but are a more realistic estimate of a true measurement error.

TABLE 4. BACKGROUND ERROR IN RADIANCE SPACE AND OBSERVATION RANDOM ERROR (K)

	AMSU channel									
	4	5	6	7	8	9	10	12	13	
Background systematic error	-0.38	-0.44	-0.23	0.01	0.35	0.07	-2.25	-9.72	-11.3	
Background random error	0.38	0.28	0.21	0.24	0.37	0.51	0.40	1.42	1.69	
Estimated observation error	1.14	0.54	0.13	0.08	0.10	0.10	0.37	1.16	1.89	

Figure 3-19: Error statistics for the background error of the same AMSU channels

### 3.3 MEASUREMENT ERROR ESTIMATES FOR AMSU AND MHS FROM COMPARISON TO FORWARD SIMULATIONS

Global IASI, AMSU and MHS measurements have been provided by Eumetsat for this study for 3 days: 17 April, 17 July and 17 October 2013. The RAL implementation of the retrieval code has been run to simulate measurements for all first guess states on all these days, using the built-in emissivity models of RTTOV for the given location and times. The comparison of these simulated measurements with the satellite observations, provides some insight into the AMSU and MHS measurement errors, though clearly differences can be expected due to errors in the first guess state, forward model errors, as well as the inherent measurement errors themselves.

Figure 3-20-Figure 3-22 show the gridded mean radiance in each AMSU+MHS band, together with the mean difference between the observation and simulation and the standard deviation in that difference. Only scenes with IASI cloud fraction < 0.01 are considered. All of these scenes for all 3 days (ascending and descending node) are included in the statistics. The following points are noted:

- There are particular strong biases over ice/snow. Over sea there is a large negative bias in the simulations as sea-ice is neglected in the simulations. Over Antarctica, the RTTOV emissivities are used but lead to large positive bias.
- There relatively small negative bias in simulations over sea in the window channels.
- There is a relatively large standard deviation in the difference in coast grid-boxes. This will be due to using the IASI land flag to represent the fraction of land in the AMSU scene, which leads to significant error in pixels overlapping the coast.

To summarise differences further, histograms of the differences between observations and simulations are constructed. Ice/snow scenes are avoided in this analysis by (a) restricting the analysis to latitudes between 60S and 60N (b) ignoring scenes over sea with a (first guess) surface temperature colder than 270K. Examples of these (considering observations over land only) are shown in Figure 3-23. In order to estimate the random error in the differences, without undue weight to outliers in the distributions, we fit a Gaussian function to these histograms and consider the mean of the fitted Gaussian as a measure of the bias in the simulations and the standard-deviation as a measure of the random error. These mean and standard deviations of the Gaussian fit are then summarised in Figure 3-24. For reference, Figure 3-25 shows comparable statistics for a selection of IASI channels (regularly sampling 1 in 5 of the channels used in the retrieval).

The estimated AMSU+MHS measurement errors obtained from the Met Office are compared to the derived standard deviations. As might be expected the diagnosed standard deviations are generally somewhat lower than the observed-simulated standard deviations (as some component of this variability will come from error in the first guess state). However, in general, results are quite consistent. Both measures indicate relatively high uncertainty in the window channels, presumably largely due to errors modelling the surface emissivity. Similarly the derived standard-deviations for IASI are typically slightly larger than the measurement errors used by the retrieval scheme. Standard deviations over land are particularly high in window channels (presumably again due to errors in modelling surface emissivity).

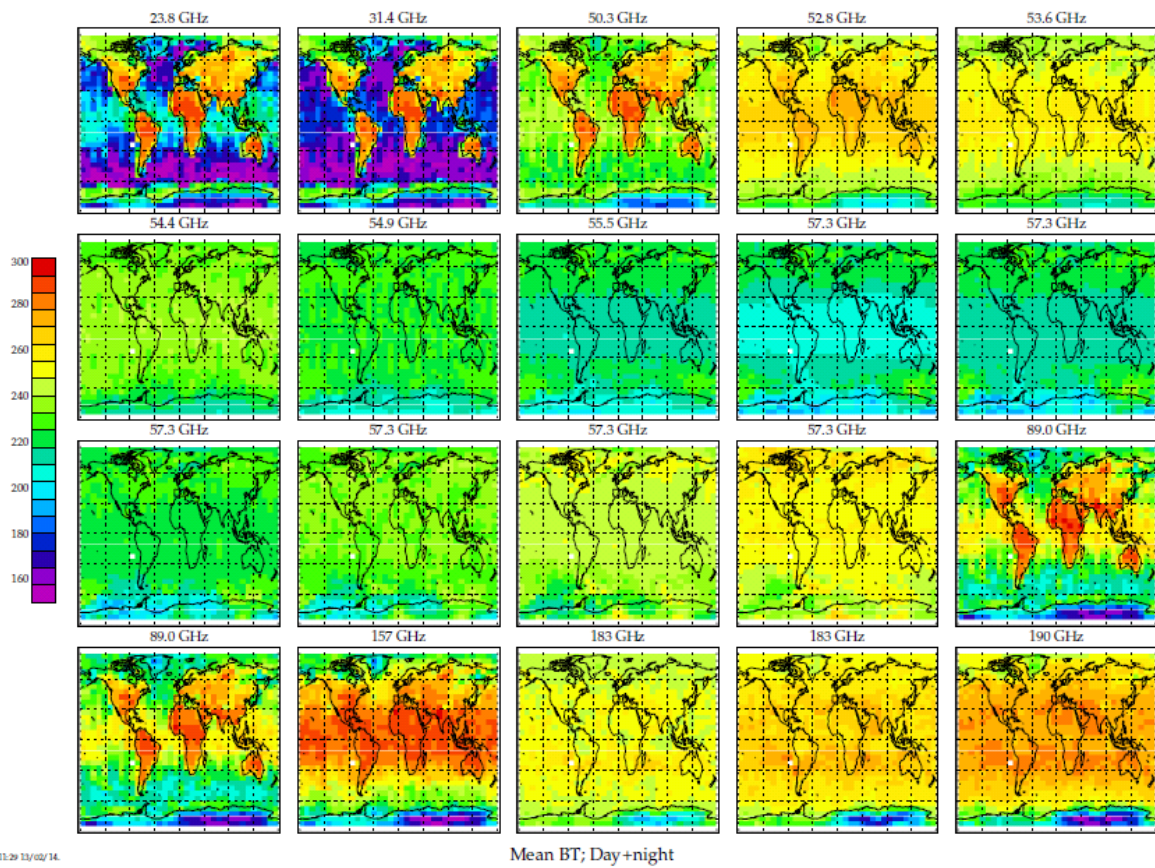


Figure 3-20: Mean observed radiance in all AMSU (top 3 rows) and MHS (bottom row) channels in 5x10 degree latitude, longitude bins, considering scenes with IASI cloud fraction < 0.01 for all three days.

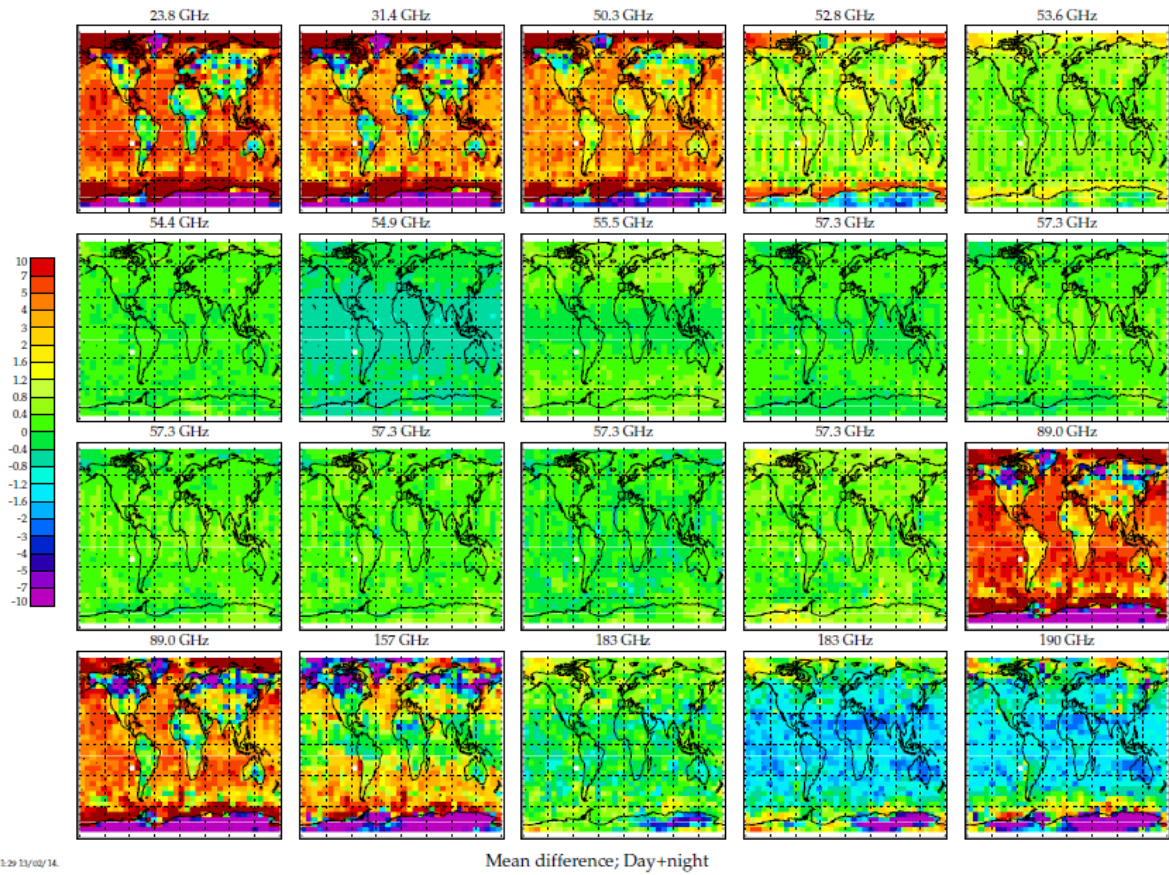


Figure 3-21: Mean difference between observations and simulations in 5x10 degree latitude, longitude bins, considering scenes with IASI cloud fraction < 0.01 for all three days.

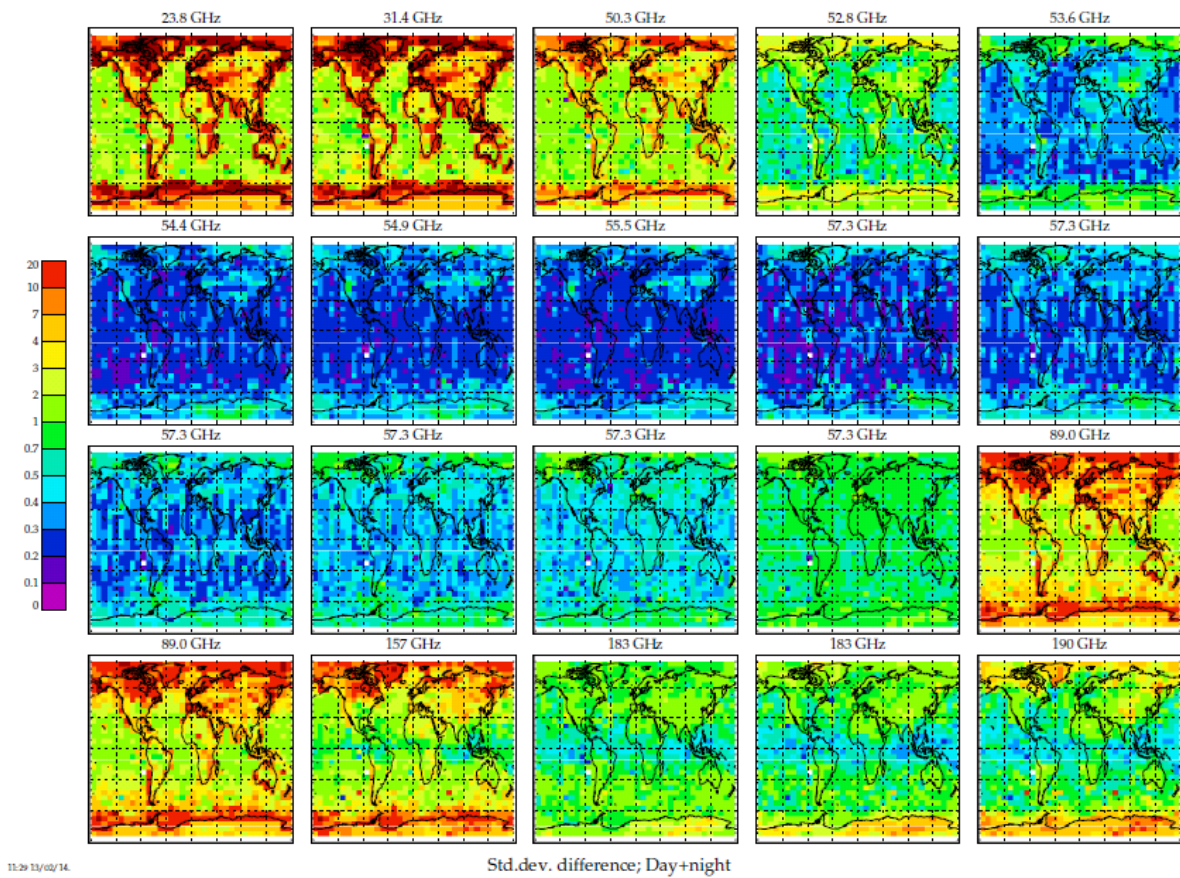
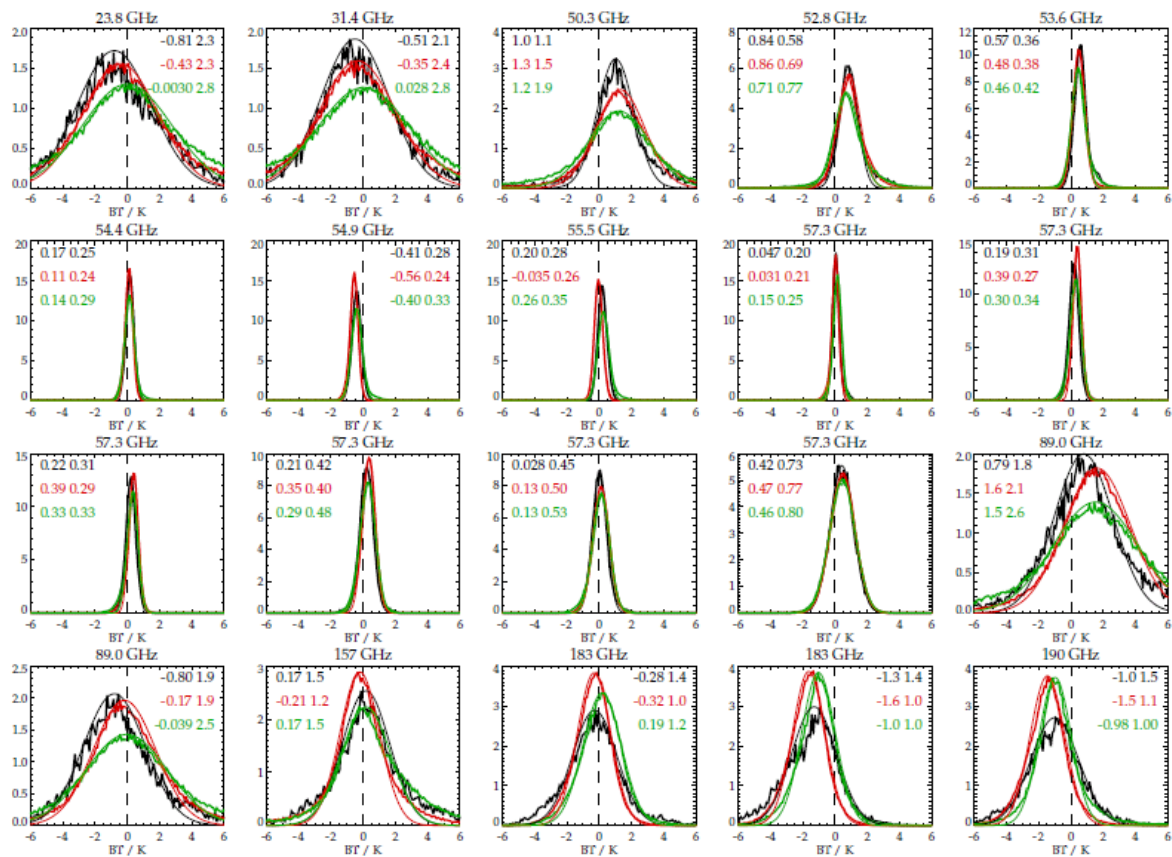


Figure 3-22: Standard deviation of the difference between observations and simulations in 5x10 degree latitude, longitude bins, considering scenes with IASI cloud fraction < 0.01 for all three days.



14.

Cloud fraction < 0.01; Land

Figure 3-23: Histograms of the differences between observed and simulated AMSU (top 3 rows) and MHS (bottom row) brightness temperatures. Different colours show results for different latitude bands: Black=60-30S; red=30S-30N; green=30-60N. Thin lines show a Gaussian function. Results shown are for scenes over land, with IASI cloud fraction < 0.01.

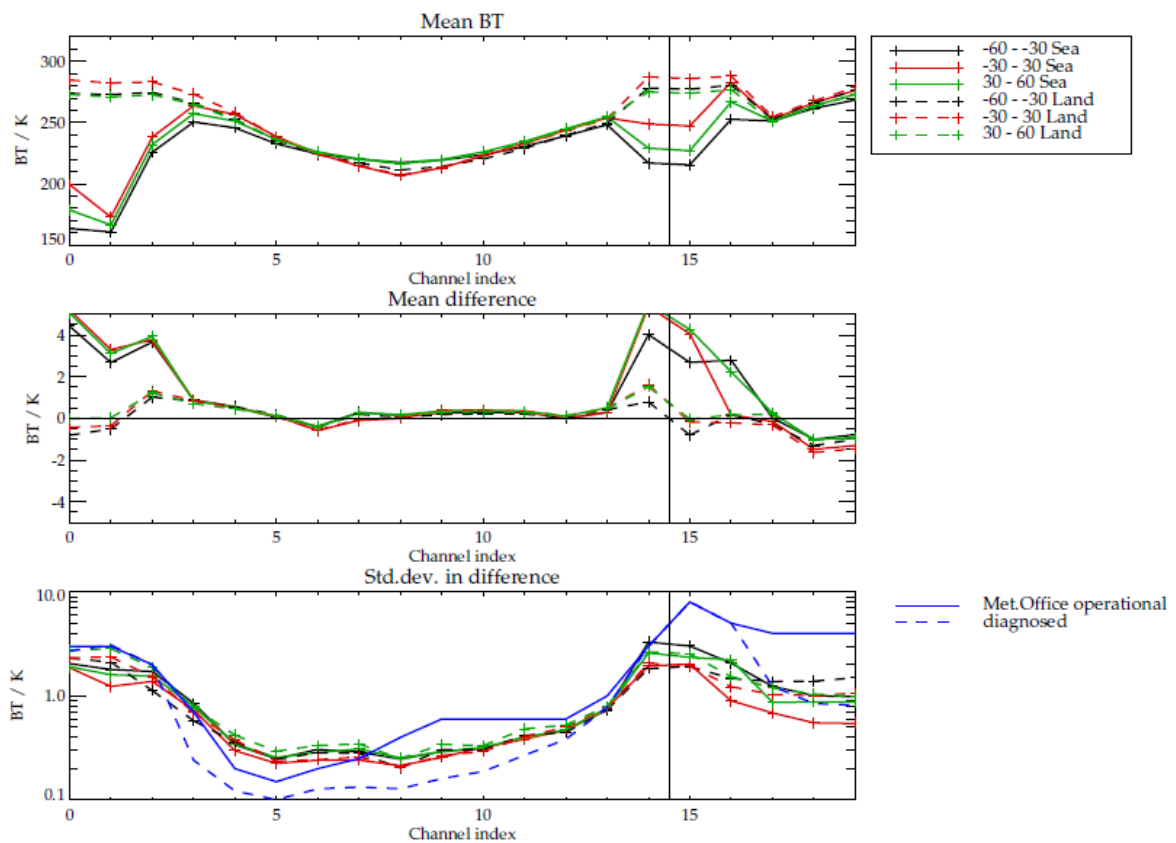


Figure 3-24: Summary of the comparison between AMSU+MHS radiances with simulations. Top panel shows the mean observed brightness temperatures in each channel (index 0-14 are AMSU-A and index 15-19 are MHS). Middle panel shows the mean difference (observation – simulation). Bottom panel shows the standard deviation in the difference. In each panel, different colours (black, red, green) correspond to different latitude bands. Solid lines show results over sea and dashed lines over land. In the bottom panel, estimates of AMSU+MHS noise from the Met Office are also shown for comparison.

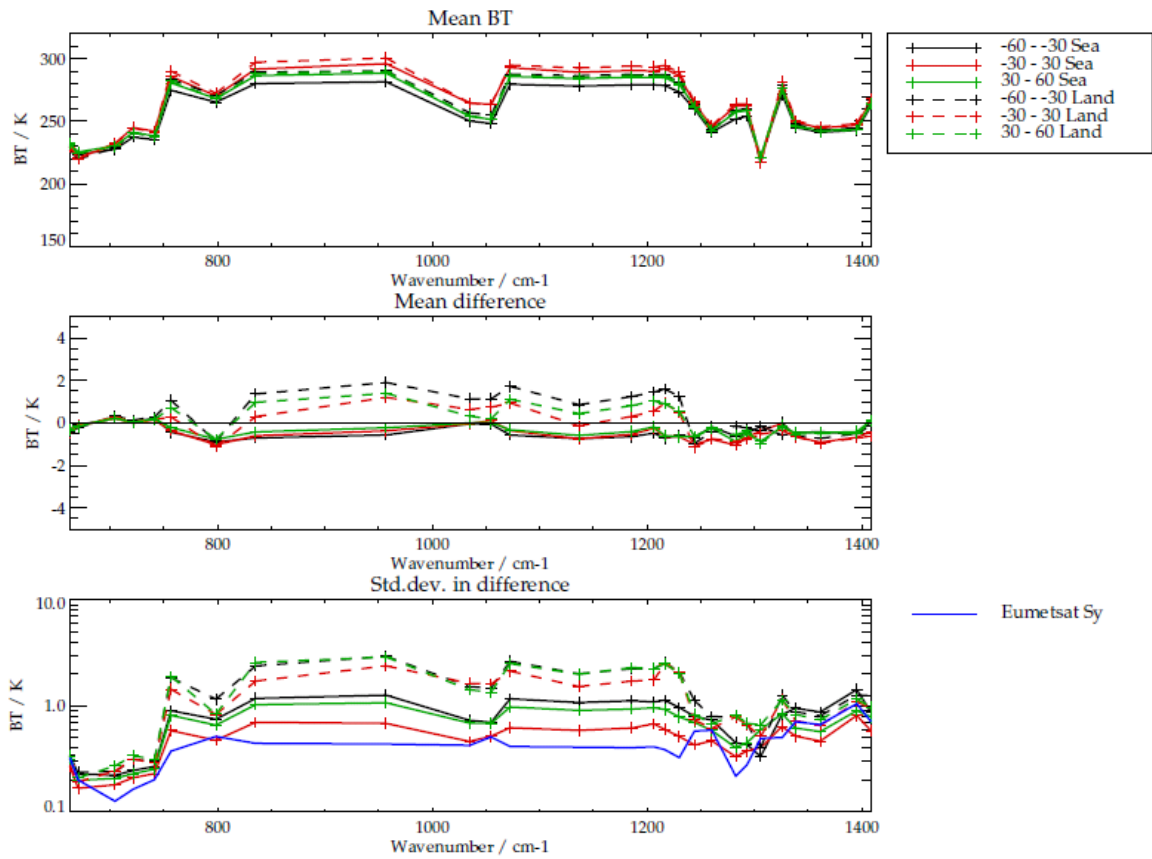


Figure 3-25: As previous figure but comparing IASI observations and simulations. Bottom panel shows the square-root diagonals of the measurement covariance assumed in the operational Eumetsat scheme.

### 3.4 ESTIMATING THE CROSS-CORRELATIONS OF THE MEASUREMENT ERRORS OF AMSU/MHS

The measurement errors for AMSU and MHS derived from the literature, and also the on obtained within this study from the MetOffice, only define the diagonal elements of the measurement covariance needed for the OEM. I.e. no error correlation between adjacent channels is present. Correlations are specifically assessed in the work at ECMWF reported in Bormann et al. **Error! Reference source not found.** This work is briefly summarised here.

The three methods are used to assess measurement errors in the work:

- Hollingsworth/Loenneberg Method
- Desroziers Statistic
- Background Error Method

A common denominator of all three methods is that they are based on a statistical ensemble of first guess (FG) or analysis departures of pairs of observations. The observations in each pair are required to be less than 1 hour apart and originate from the same instrument on the same satellite. All possible pairs were collected over the study period, and the pairs of observations were binned by separation distance, using a binning interval of 25 km unless indicated otherwise.

A common assumption is that the FG is spatially correlated, whereas observation errors are not. By analysing the error contribution and arranging the results in increasing order of the norm of the pair of measurements from the statistical ensemble, a conclusion of the cross-correlation length can be drawn. The different approaches of the individual methods are summarised in short details in the following paragraphs.

#### 3.4.1 HOLLINGSWORTH/LOENBERG METHOD

This method is based on the assumption that true background errors are spatially correlated, whereas observation errors are spatially uncorrelated. As a result, observation errors can be estimated by calculating FG-departure covariances from pairs of FG departures as a function of separation distance (see, for instance, the black lines in Figure 3-30). Observation errors are estimated by extrapolating the covariance/separation relationship from non-zero separations to zero separation, so that the FG-departure variance at zero separation is split into a spatially correlated part and a spatially uncorrelated component. The latter is assumed to give the observation error. The method also assumes that observation and background errors are uncorrelated.

#### 3.4.2 BACKGROUND ERROR METHOD

This method uses covariances of FGdepartures and subtracts from these the assumed background errors, mapped into radiance space, and possibly scaled as described below. The background-error estimates are taken from the assimilation system, and they have been derived using an ensemble method. The background-error-subtraction method assumes that observation and background

errors are uncorrelated, and that the assumed background errors provide good estimates of the true background errors. The method is applied to derive spatial and inter-channel observation-error characteristics.

### 3.4.3 DESROZIER'S METHOD

Assuming that variational data-assimilation schemes broadly follow linear estimation theory, consistency diagnostics can be derived for observation, background and analysis errors in observation space from FG and analysis departures. These diagnostics have been derived and summarized by Desroziers et al., and the authors of Bormann et al. make use of the following relationships:

$$R = E [d_a d_b^T]$$

$$HBH^T = E [d_b d_b^T] - E [d_a d_b^T]$$

where  $R$  is the diagnosed observation-error covariance matrix,  $B$  is the diagnosed background-error covariance matrix,  $H$  is the linearized observation operator,  $d_b$  are the background departures of the observations,  $d_a$  are the analysis departures of the observations and  $E [ ]$  is the expectation operator.

Apart from the usual assumptions on Gaussian errors and no error correlations between FG and observation, etc., the diagnostic expressions also assume that the weight given to the observations in the analysis is in agreement with the true error covariances.

While primarily introduced as a consistency diagnostic, Desroziers et al argue that the diagnostic equations may be used to estimate improved versions of the background- or observation-error covariances. They point out that the diagnostic equations formulate a fixed-point problem, and the solution may be derived iteratively by using the diagnosed values in a subsequent assimilation, which is then used again to calculate the diagnostics. The method has been used to estimate observation errors and inter-channel error correlations.

Figure 3-26 up to Figure 3-29 show the measurement error estimates and also the measurement error cross-correlations from the the methods described above. The results are first given for the AMSU-A instrument, and then for MHS. It's worth noting that the AMSU-A analysis is based on data from the NOAA satellite, whereas this study of "OEM retrievals of measurements from IASI, AMSU and MHS is" based on measurement data from the MetOp-A version of AMSU-A and MHS. Given that the instruments on all platforms are of identical design, and that all potential inter-channel or inter-spatial cross-correlations are design specific, and not instrument specific, the findings should be directly transferrable to MEtOp AMSU/MHS.

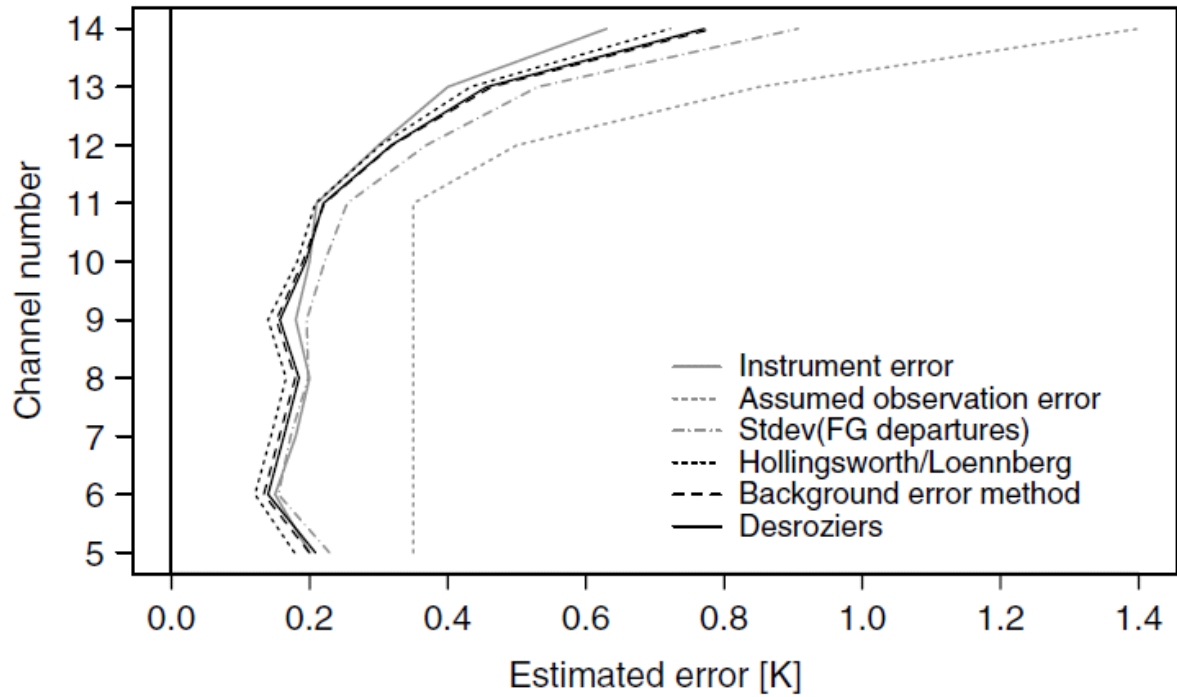


Figure 3-26: AMSU-A measurement error estimates from Hollingsworth/Loennberg, Desroziers and background error method.

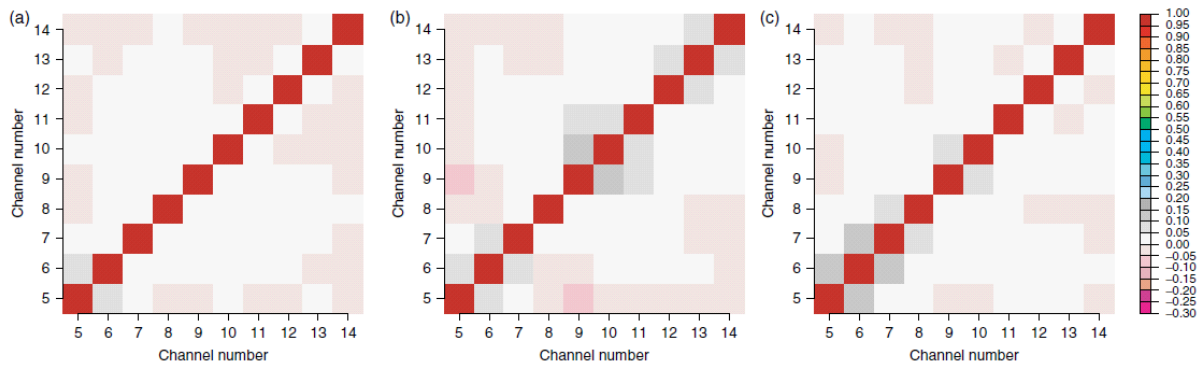


Figure 3-27: AMSU-A error covariance matrices for (a) Hollingsworth/Loennberg, (b) background error and (c) Desroziers. Note that from Desroziers statistics the resulting matrix is not generally square; it has been squared in this example. Generally though, the cross correlations for AMSU-A are diminutive.

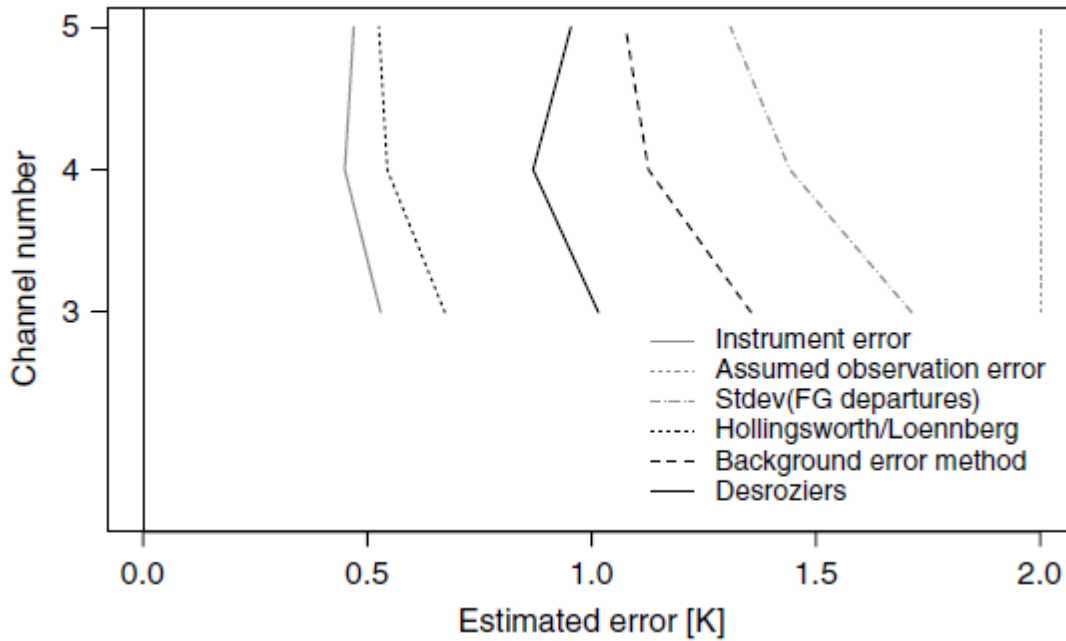


Figure 3-28: AMSU-A measurement error estimates from Hollingsworth/Loennberg, Desroziers and background error method.

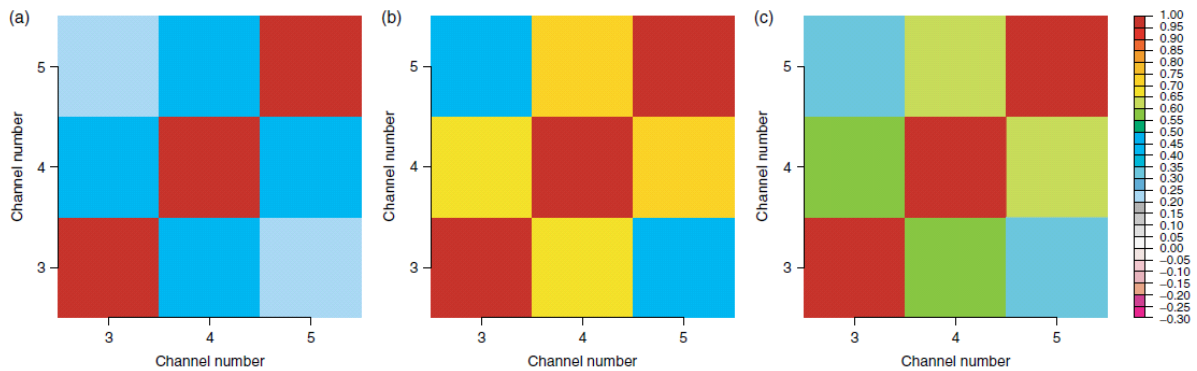


Figure 3-29: MHS error covariance matrices for (a) Hollingsworth/Loennberg, (b) background error and (c) Desroziers. Note that from Desroziers statistics the resulting matrix is not generally square; it has been squared in this example. As opposed to AMSU-A the channel cross-correlations of MHS are rather large, and the results from the three methods differ visibly.

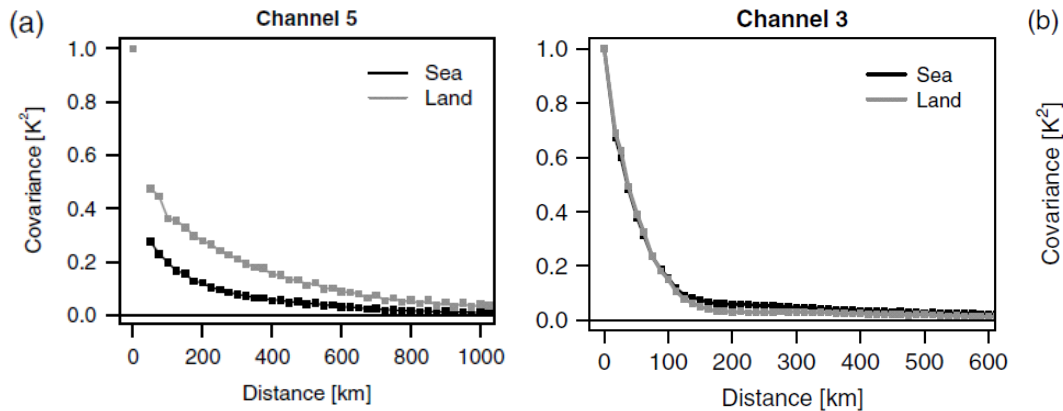


Figure 3-30: Spatial observation-error correlation for AMSU-A channel 5 (a) and MHS channel 3 (b) with a 12.5 km binning interval. (Note the smaller range of separation distances for MHS compared to AMSU-A).

### 3.4.4 COMPARISON OF HOLLINGSWORTH, DESROZIER, ETC. VS. RAL AND METOFFICE MEASUREMENT ERRORS

The conclusion from Bormann et al. **Error! Reference source not found.** are that both the channel and spatial cross-correlations for AMSU-A are negligible. It is therefore not surprising that the measurement errors for the AMSU channels generally agree between all 4 datasets. It's only in the few window channels (4, 5, 6) that the RAL analysis is slightly higher than both the Hollingsworth/Loennberg and the Desroziers method. That is less so for MHS on the other hand. For MHS, Bormann et al. found more significant cross-correlations. Nevertheless, the measurement errors they derive lie between the RAL analysis (Hollingsworth/Loennber) and the MetOffice diagnosed error (Desroziers). The four different datasets are therefore reasonably self-consistent. Only the operational MetOffice error is significantly larger than the others, but we have to recall that the operational error will include systematic error components (i.e. forward model errors).

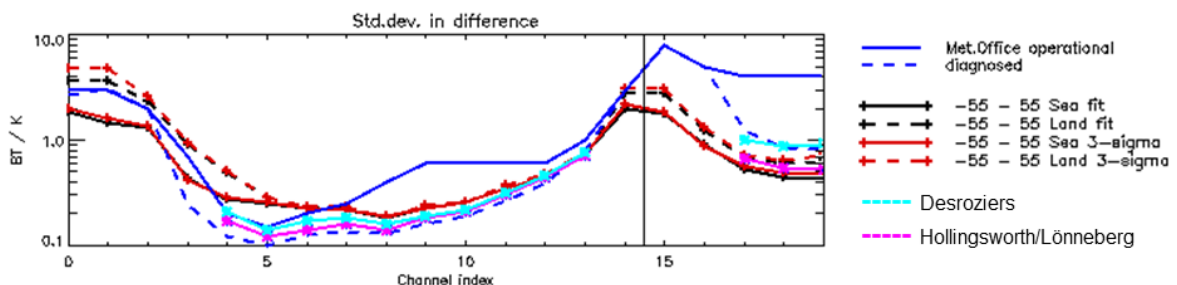


Figure 3-31: Comparison of AMSU/MHS measurement errors with the RAL methods described in Section **Error! Reference source not found.** as well as the MetOffice operational measurement errors. Where data is present, both the Desroziers and the Hollingsworth/Loenneberg method produce errors similar to the RAL method. Only in the window channels does the RAL method result in slightly larger measurement errors.

The MetOffice operational errors are larger overall, but they do include forward model errors which skews the comparison.

## 4 TASKS 2 & 3: OEM(MWIR/METOP-B) OVER OCEAN, CLEAR-SKY AND LAND, CLEAR-SKY

In task 2, an OEM scheme for IASI which matches the Eumetsat product processing facility (PPF) settings is implemented at RAL. After verifying the performance of the scheme, we then apply it to Eumetsat selected days of IASI and AMSU/MHS cloud-free data over ocean (Task 2) and land (Task 3), to generate results for IR only and MW+IR (MWIR). Fixed surface emissivities as defined by RTTOV are assumed in this task. Results are evaluated by comparison to ECMWF analyses using a range of diagnostics.

### 4.1 DERIVATION OF BIAS CORRECTION AND OBSERVATIONAL ERROR COVARIANCE FOR AMSU+MHS, BASED ON IASI RETRIEVALS

IASI only retrievals based on the Eumetsat OEM have been used to derive a bias correction and observation error covariance for AMSU+MHS, under the assumption that the retrievals provide the best estimate of the true atmospheric state on which to base radiative transfer simulations of the AMSU+MHS observations. The following approach is implemented:

- Results from the IASI-only scheme for all three days (17 April, 17 July, 17 October 2013) are used to simulate measurements in the AMSU+MHS channels.
- The mean differences between these simulations and observations are determined separately for scenes over land and over sea. Only cloud-free scenes (according to the provided cloud mask) between latitudes 60 S and 60 N are considered (to avoid ice and snow covered cases, for which the emissivity is not well defined by RTTOV).
- Differences are computed in 6 bins of across-track (and detector) pixel index, regularly spaced from 0-119 in steps of 20 across-track pixels (there are 120 IASI observations across track, i.e. 30 scans and 4 detectors).
- This results in a 20 (AMSU+MHS channel) times 6 (across-track bins) times 2 (land, sea) dimension array, which is bi-linearly interpolated (in across-track pixel index and land fraction) to give the bias correction to be applied to a given observation.

An approach based on view zenith angle (as provided by Eumetsat for IASI) was also tested, however some channels (particularly 8-14) appear to have bias which is not symmetric from the nadir, hence across-track index is considered more suitable.

The binned differences are illustrated in Figure 4-1. This also shows the standard deviation in the differences (derived from a Gaussian fit to the histogram of differences). Standard deviations are also compared to the estimates of AMSU+MHS measurement errors from the Met Office. Generally the values derived here and from the Met Office are comparable, and lie between the analysed differences and the inferred contribution from observation / forward model errors. It is however

noted that the standard deviation is relatively large in channels 4 and 5 at the edges of the swath and all standard deviations are relatively large in channels 0-2.

Figure 4-2 shows a similar comparison but from simulations based on the PWLR first guess (instead of IASI retrieval). It is noted that bias over sea in window channels 0-2 and 14 is smaller in this case (and this is also true for the corresponding standard deviations).

The observation covariance for retrievals is then derived from the difference between the simulations and the bias corrected observations (considering all across-track pixels). A 3-sigma test is applied to exclude outliers, based on the standard deviation of the Gaussian fit to the histogram of all deviations (as described under Task 1, above). A separate covariance is computed for land and sea. The standard deviations are illustrated in Figure 4-3 (in which results are compared to the estimated values from the Met Office). Solid lines in this figure show the standard deviation of a Gaussian fit to the histogram of deviations; dashed lines show the standard deviation of the distribution derived from the covariance matrix (which are very similar to each other). Note that standard deviations are larger (by up to factor 3) in window channels over land.

The correlation matrices in Figure 4-4. These reflect expected correlations in the window channels, arising from spectrally correlated errors in the modelling of surface emissivity.

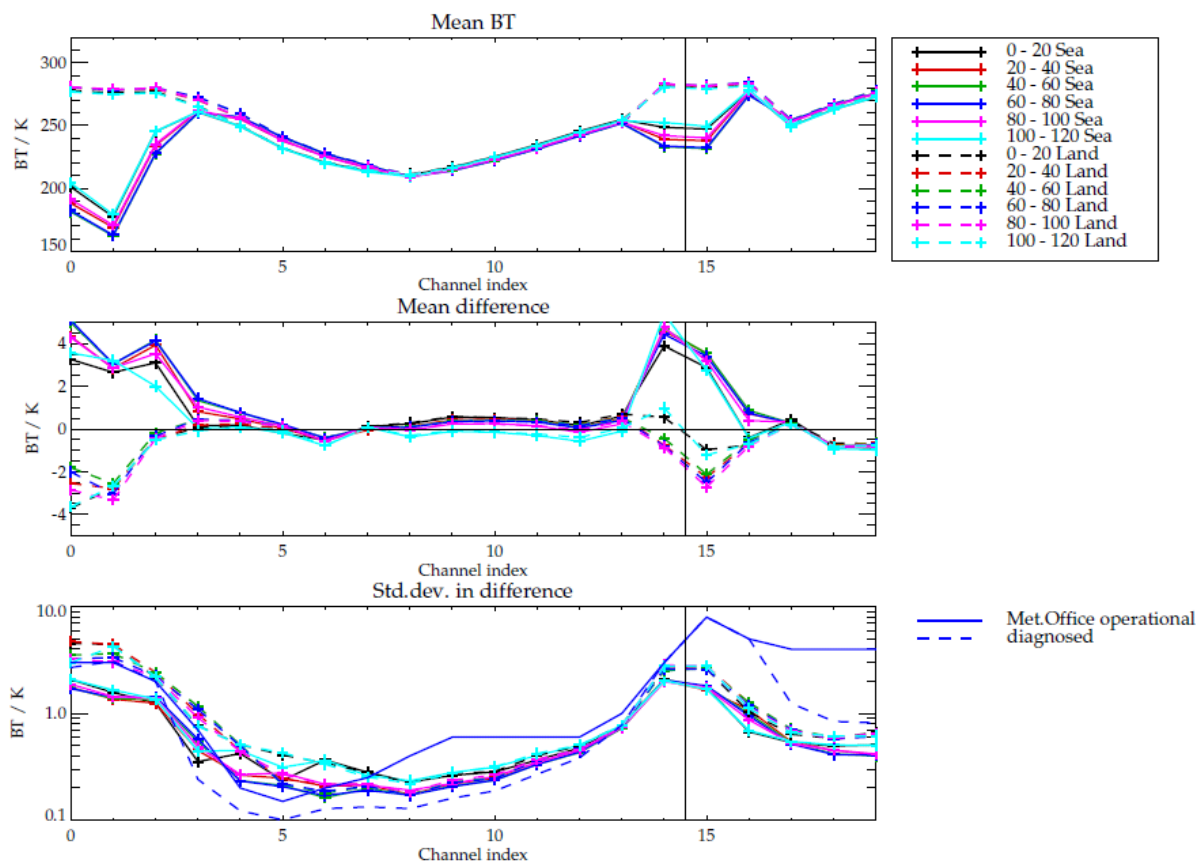


Figure 4-1: Statistical comparison of simulated and observed AMSU+MHS radiances, as a function of cross-track scan index. Simulations based on IASI-only retrievals.

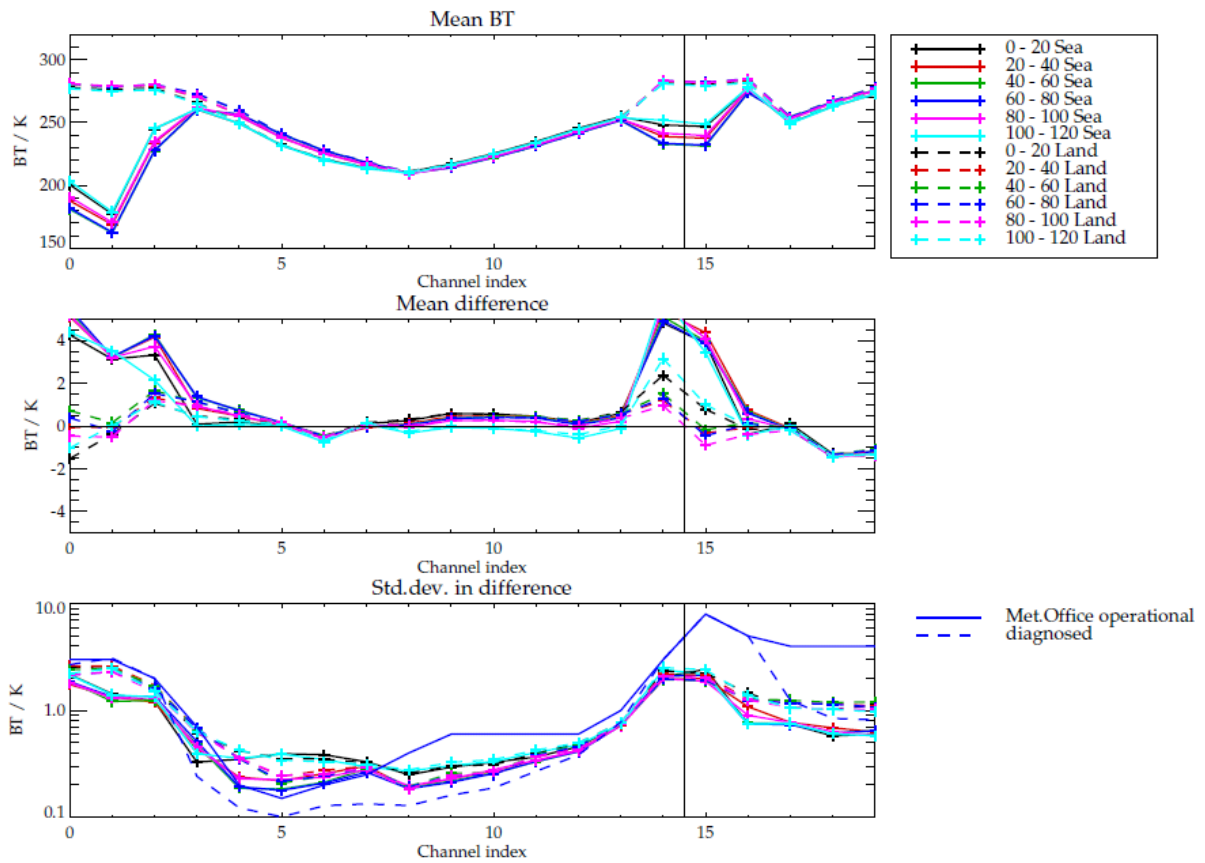


Figure 4-2: Statistical comparison of simulated and observed AMSU+MHS radiances, as a function of across-track scan index. Simulations based on PWLR state.

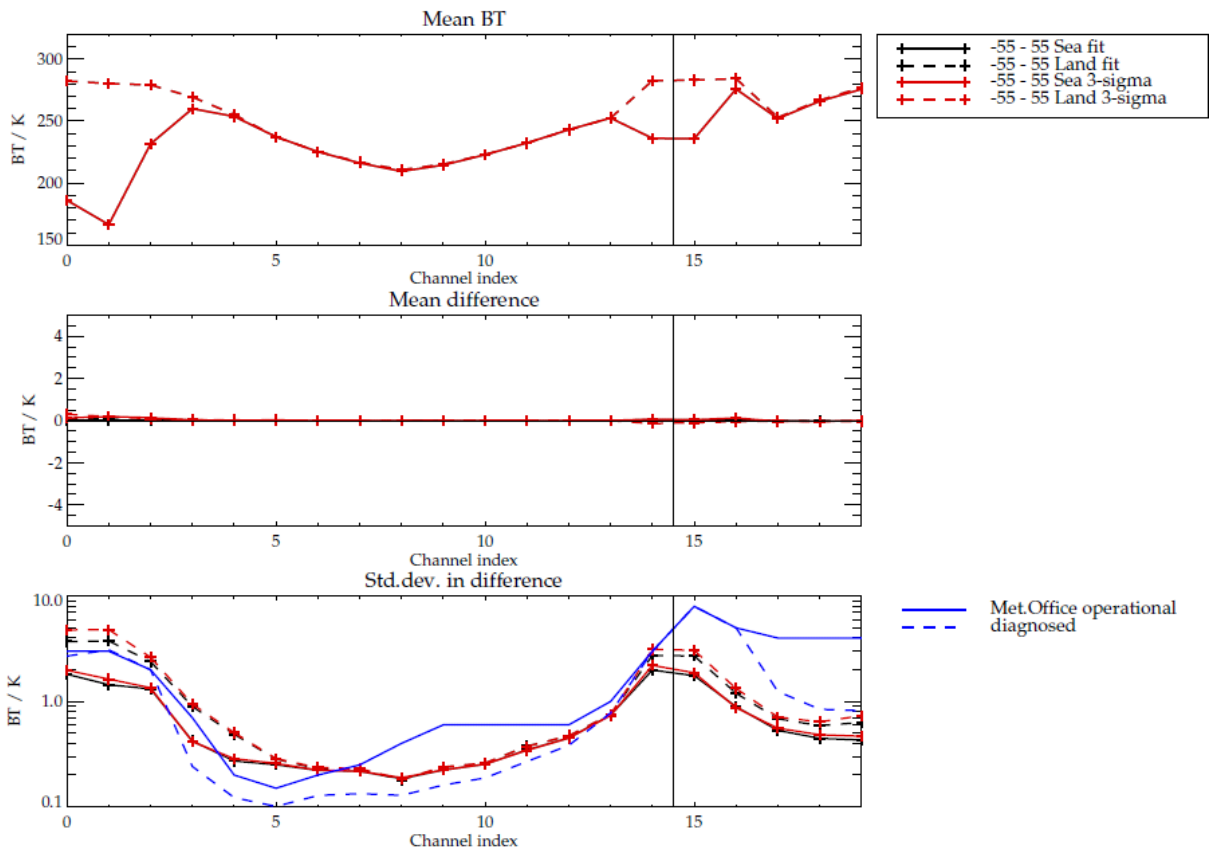
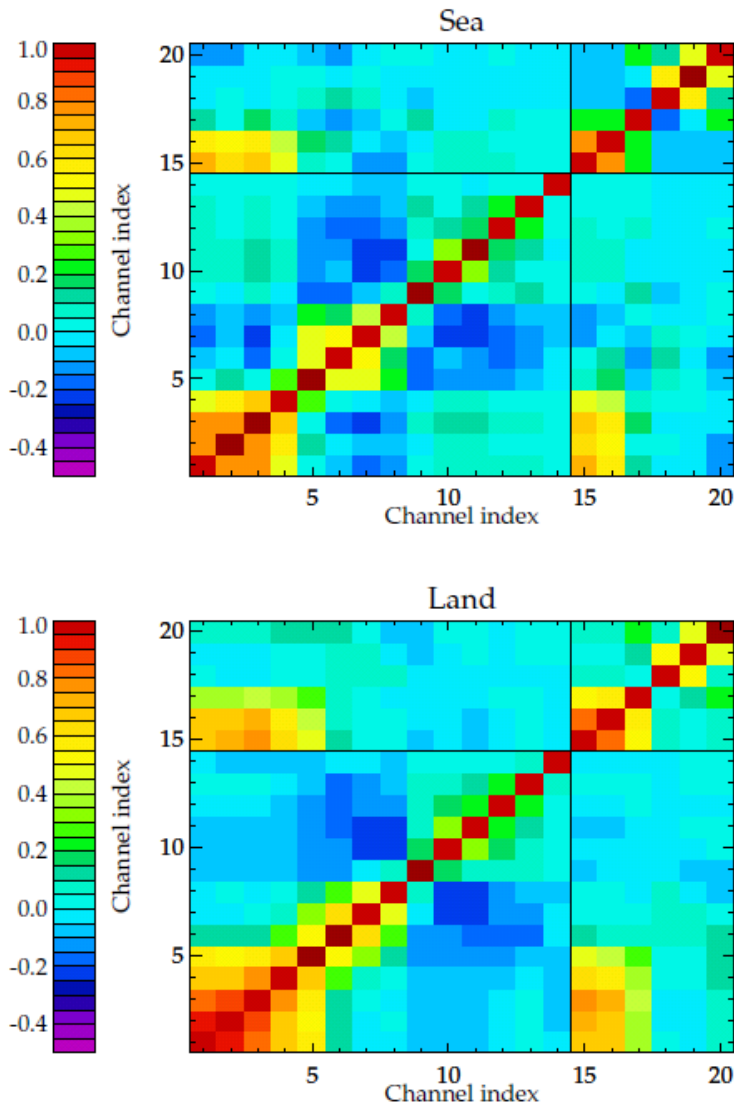


Figure 4-3: Statistical comparison of simulated and observed AMSU+MHS radiances, after bias correction of AMSU+MHS. Simulations based on IASI-only retrievals. Statistics are derived based on Gaussian fit to histograms and directly as mean and standard-deviations, after applying a 3-sigma test to exclude outliers.



19:10:04/04/14

Figure 4-4: Derived observation correlation matrices for Ocean (top) and Land (bottom), based on differences between AMSU+MHS observations and simulations based on IASI-only retrievals. Solid vertical/horizontal line in both plots separate AMSU and MHS channels.

## 4.2 IASI OEM RETRIEVALS (IR AND MWIR): RESULTS

Retrievals have been run for all three selected days, globally over both land and sea for three retrieval configurations:

- IASI only (which can be compared directly to the Eumetsat ODV results).
- IASI+AMSU+MHS, using the bias correction described in section 4.1 and full estimated covariance.
- IASI+AMSU+MHS, as above, but setting off-diagonal elements of the covariance to 0.

To illustrate the information added by AMSU+MHS, four scenes, corresponding to mid-latitude land and sea and tropical land and sea, have been selected from observations on 17 April 2013. Scenes for which an ODV retrieval with relatively small cost and near-nadir observing conditions are selected. For these scenes, plots of the full averaging kernel, and estimated error profiles are shown in section 8 of the plot Annex to this report. These show linear retrieval results based on the PWLR (first guess / prior) profile (no iteration of the state is performed). For these examples, a fourth retrieval option is tested in which the IASI+MHS measurement errors are assumed to be 0.2 K NEBT, an optimistic case corresponding to an assumption that the surface emissivity is perfectly known and hence no corresponding forward model errors need be considered. This indicates the maximum potential information gain that can be reasonably expected.

The changes in degrees of freedom for signal (DOFS, the trace of the averaging kernel) for temperature and water vapour are summarised in Table 2 and Table 3

	IASI-only	MWIR full covariance	MWIR no correlations	MWIR 0.2K NEBT
Mid-latitude land	6.2	8.2	8.1	9
Tropical land	6.9	8.9	8.8	9.9
Mid-latitude ocean	5.6	8.7	8.6	9.5
Tropical ocean	6.9	9.2	9.1	10

Table 2: Degrees of freedom for signal for temperature for 4 retrieval options and 4 example observations.

	IASI-only	MWIR full covariance	MWIR no correlations	MWIR 0.2K NEBT
Mid-latitude land	4	4.6	4.5	5
Tropical land	5.5	5.9	5.9	6.4
Mid-latitude ocean	3	3.8	2.8	4
Tropical ocean	5.4	6.1	6.1	6.5

Table 3: Degrees of freedom for signal for water vapour for 4 retrieval options and 4 example observations.

	RAL Space STFC Rutherford Appleton Laboratory Harwell Oxford Chilton, OX11 0QX, United Kingdom	Document:	Final Report
		Customer Ref:	ITT 13/207194
		RAL Space Ref:	SSTD1569
		2015-01-29	Page 65 of 120

Generally speaking, the following points can be concluded:

- Using the derived observation errors, IASI+MHS add 2 degrees of freedom to temperature and about half a degree of freedom to water vapour. Effects on ozone are negligible.
- Neglecting off-diagonals reduces DOFS on temperature and water vapour by about 0.1 (a small effect).
- For temperature, the improvements are related mainly to the stratosphere though some improvement is also noticeable in the troposphere, in particular over the ocean (where the assumed measurement covariance is relatively low).
- For water vapour improvements are mainly related to the upper troposphere, and penetrate to relatively low altitudes in the mid-latitudes.
- Assuming 0.2 K NEBT errors to apply to all channels adds an additional degree of freedom to temperature and an additional half a degree of freedom to water vapour. This additional information relates to the troposphere for both water vapour and temperature, in some cases considerably sharpening the near-surface averaging kernel.

Global results have been systematically compared to the provided ECMWF analyses. The following sub-set of scenes is generally used for this analysis:

- The L2 (version 6) cloudiness flag must have a value of 1 or 2 (see further discussion on the cloud flags in section 6.3, below). The operational OEM is only performed on such scenes. Usually the term “cloud-free” in this report is taken to refer to these scenes, i.e. not strictly cloud-free but sufficiently so to allow reasonable OEM retrievals without taking cloud explicitly into account.
- The scene does not contain sea ice according to a Eumetsat provided test (based on the AMSU radiances in channels 1-3)
- The scene does not contain significant precipitation, according to a Eumetsat provided flag.

Furthermore, when large scale averaging is performed, this is usually done over a latitude range of 60S to 60N to avoid issues particular to polar regions (problems modelling ice emissivity, low signal to noise etc).

Profiles are retrieved on a vertical grid which is generally much more finely spaced than the vertical resolution. In order to avoid resolution-related issues strongly dominating the comparison, we perform statistical comparisons on smoothed, vertically sub-sampled, versions of the profiles. A vertical grid more consistent with the expected vertical resolution is defined for each species. Profiles values (retrieval and analysis) are obtained at each point,  $i$ , in the grid by taking the weighted average of the profile values between the grid point  $i-1$  and  $i+1$ , weighted by a triangular function which is zero at grid points  $i-1$  and  $i+1$  and peaks at grid point  $i$ . Grids are defined in terms of the quantity  $z^*$ , which is log pressure, scaled to correspond approximately to altitude:

$$z^* = 16 * (3 - \log_{10} p)$$

**Equation 2**

Where  $p$  is pressure in hPa. Grids are defined separately for each species as follows:

	RAL Space STFC Rutherford Appleton Laboratory Harwell Oxford Chilton, OX11 0QX, United Kingdom	Document:	Final Report
		Customer Ref:	ITT 13/207194
		RAL Space Ref:	SSTD1569
		2015-01-29	Page 66 of 120

- Temperature: 0, 1, 2, 3, 4, 6, 8, 10, 12, 14, 17, 20, 24, 30, 35,40,50 km.
- Water vapour: 0, 1, 2, 3,4, 6, 8, 10, 12, 14, 17,20 km
- Ozone: 0, 6, 12, 18, 24, 30, 40 km.

The grid is defined relative to the surface pressure /  $z^*$ .

Comparisons are also made between retrieved profiles and the analysis smoothed by the averaging kernel (determined at the retrieval solution state),  $\mathbf{x}'$ , derived as follows:

$$\mathbf{x}' = \mathbf{a} + \mathbf{A} (\mathbf{t} - \mathbf{a})$$

**Equation 3**

Where  $\mathbf{a}$  is the *a priori* profile from the PWLR,  $\mathbf{t}$  is the supposed "true",  $\mathbf{A}$  is the retrieval averaging kernel (transformed to represent derivatives of the retrieval on the 101 level RTTOV grid with respect to perturbations in the true profile on that same grid).

These results are shown in the plot annex. Both maps of comparisons on individual sub-sampled levels and profile statistics are shown (in sections 6 and 10 of the annex, respectively). Maps are shown for averages of the following three layers 0-2km, 0-6km and 6-12km, defined in  $z^*$  coordinates, relative to the surface pressure.

Section 9 of the plot annex also shows some more comprehensive sets of OE diagnostics for some selected, representative individual scenes. Section 5 includes plots of nadir retrievals along individual orbits. The basic performance of the IR+MWIR schemes are also summarised here in Figure 4-5 and Figure 4-6.

Note that the annex includes results also from the extended retrieval schemes discussed under tasks 4-5 below. For now, we focus on points regarding the application of the standard OEM to IR and MW+IR measurements.

Differences between (RAL) retrievals and (Eumetsat) ODV are generally very small, particularly compared to the estimated retrieval error (from solution covariance). Some differences may be related to different measures of convergence. Some relatively large differences are seen over desert surfaces, where the retrieval cost function values are relatively high. These differences are attributed to the different convergence approaches implemented by the two schemes. In general the RAL scheme iterates further and reaches a slightly lower cost the ODV.

According to the linear retrieval diagnostics (plots in section 8 of the annex), including AMSU+MHS measurements improves estimated errors slightly, however in real retrievals there is very little change in the agreement between retrievals and analysis (without using averaging kernels). Accounting for averaging kernels, the agreement with analysis is seen to degrade slightly (in terms of standard deviation) in general although the apparent degradation is worse for PWLR. The apparent degradation in performance in terms of agreement with analysis, accounting for kernels, is largely independent of viewing angle, latitude, and whether observations are over land or sea.

	RAL Space STFC Rutherford Appleton Laboratory Harwell Oxford Chilton, OX11 0QX, United Kingdom	Document:	Final Report
		Customer Ref:	ITT 13/207194
		RAL Space Ref:	SSTD1569
		2015-01-29	Page 67 of 120

Including or not off-diagonals in the AMSU+MHS observation covariance has a minor effect on retrievals (confirming expectations based on the linear retrieval diagnostics for the four example scenes). For the remainder of the study, the MW measurement covariance with correlations was used in most retrieval runs.

It is clear from the analysis that the PWLR results are already of rather high quality: Errors in temperature are around 1K and errors in humidity around 20-30% in most of the troposphere (reducing above). Performance is generally worse over land, particularly near (or at) the surface. It should however be noted that errors in the analysis (and its interpolation to the IASI location / time) will be larger near the surface over land, so some of this apparent degradation may reflect analysis error rather than retrieval error. It is a challenge for the OEM to significantly improve upon PWLR, however does do so, particularly for temperature over land. Some improvements can be seen near the surface, but it is also interesting to note the structure in the upper troposphere around 50N in the orbit cross-section (Figure 4-5) which is apparently better resolved in the analysis (similar features are seen in other orbits on this day).

A couple of potentially misleading aspects of the comparison approach should be noted:

- PWLR is trained using analysis. There may be situations in which the analysis is systematically wrong, and PWLR follows this incorrect behaviour, while the OEM is drawn towards the truth. In this situation the analysis approach here would indicate that the OEM performs worse than PWLR.
- PWLR is used as *a priori* for the OEM. Some of the same measurement information has been used in the PWLR, so that in principle the prior state depends on the measurements used in the OEM. This is not accounted for in the determination of the averaging kernels which may therefore under-represent the sensitivity of the end product to the truth. In practise this issue may not be too significant as the prior error covariance is large compared to the errors which would be expected purely on the basis of noise on the observations. It is estimated by comparison of PWLR retrieval to analysis and this includes a large contribution from analysis errors (including errors from sampling analysis to the time/place of the IASI observation, as well as inherent NWP error). Nevertheless, in some cases / regions, particularly for ozone, the prior constraint from the PWLR is rather strong, and the retrieval may not move far from the PWLR. Particularly in these situations (dominated by smoothing error), the PWLR may agree well with analysis smoothed by the kernels, because the latter tends to the prior (i.e. the PWLR). In the absence of information from the measurements PWLR and smoothed analysis will agree perfectly. Care should therefore be exercised in drawing conclusions from the relative performance of PWLR and retrieval in comparison to averaging kernel smoothed analysis. In order to avoid this issue and test some aspects of the OEM, in isolation from the PWLR, some retrievals are performed using a more simply defined, looser “climatological” prior state and covariance (see below).

In general, it remains safe to say that if the retrieval improves over PWLR this can be considered a good result for the OEM. However, the converse does not necessarily imply the OEM is really worse than PWLR as PWLR is not independent of the analysis and may have errors in common.

The orbit cross section clearly illustrates the power of the PWLR approach, which allows retrievals of apparently similar (or only slightly degraded) quality to be performed in scenes also affected by cloud. In the later tasks of the study, we assess whether, via addition of the MW observations, the OEM can also be made to function in cloudy scenes.

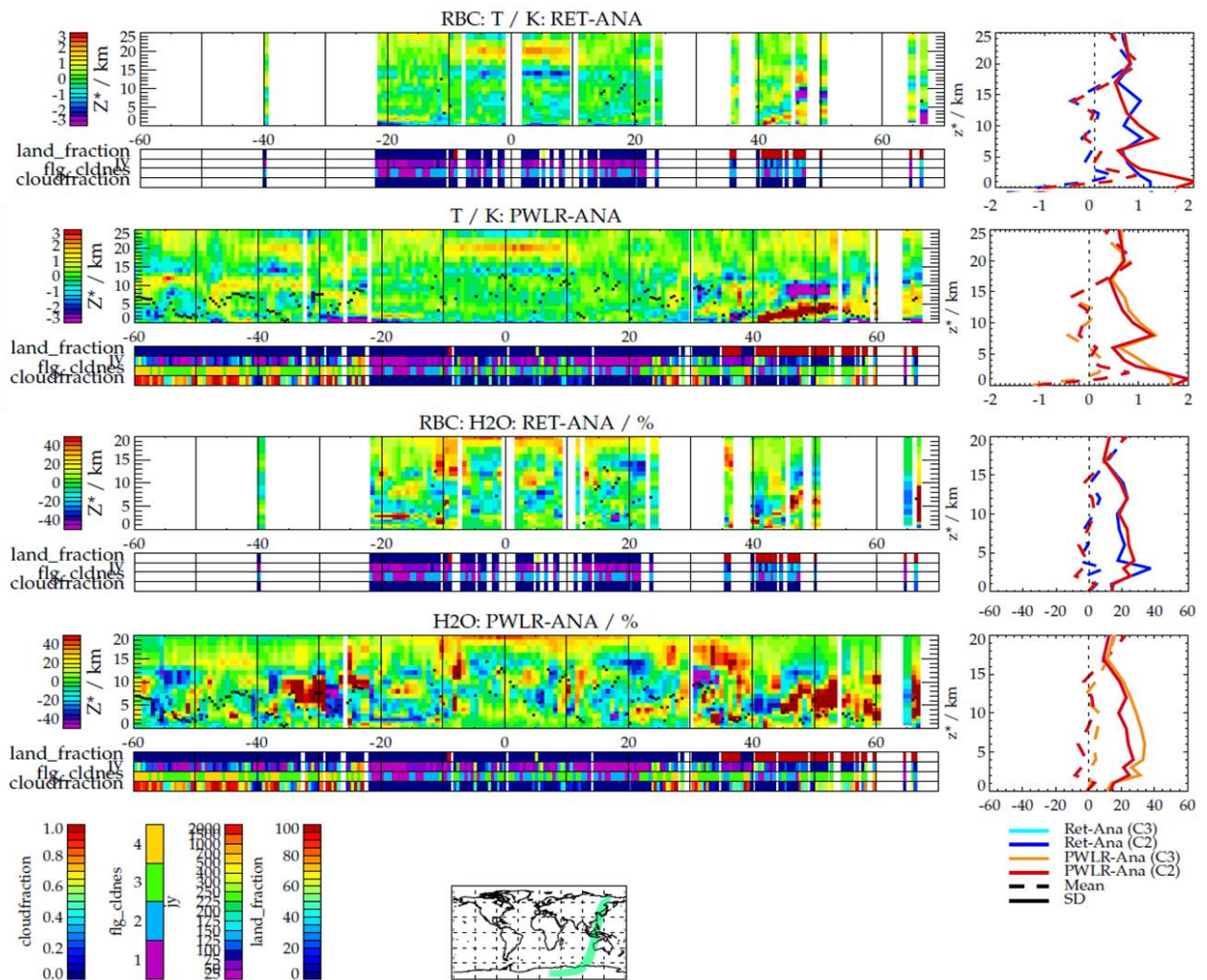


Figure 4-5: Example orbit cross-section from 17 April 2013. Top two panels show the difference from the analysis of the IR-only retrieved (RET-ANA) and PWLR (PWLR-ANA) temperature profiles (in K), respectively; bottom two rows show the corresponding differences for water vapour in %. Ribbons under each cross-section show the land fraction, measurement cost (“jy”), L2 cloudiness flag (“fig\_cldnes”) and the L2 cloud fraction. Panels on the right show the mean and standard deviations of the data in the cross-sections, however only including profiles for which the cloudiness flag is 2 or less (“C2” in legend) or 3 or less (“C3”).

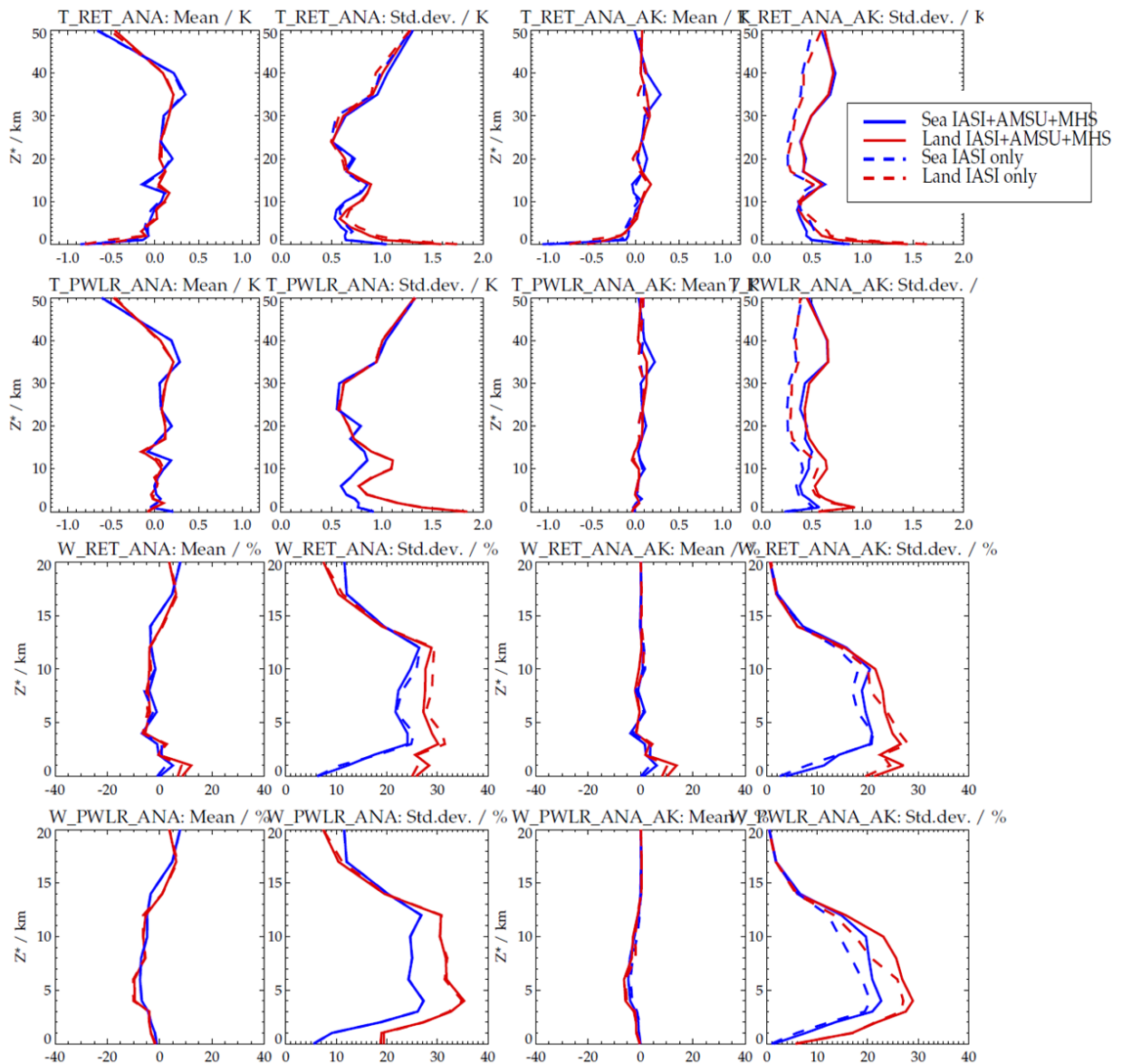


Figure 4-6: Summary of differences between IR and MWIR retrieval, PWLR and analysis. Top two rows show results for temperature; bottom two rows for water vapour. Red curves show results for land and blue for sea. Dashed lines show the IR only results, solid lines MWIR. Panels are presented in pairs, with the left and right hand panel showing, respectively, the mean and standard deviation of the difference between retrieval and analysis (RET\_ANA), PWLR and analysis (PWLR\_ANA), retrieval and analysis smoothed by the averaging kernels (RET\_ANA\_AK), PWLR and analysis smoothed by the averaging kernels (PWLR\_ANA\_AK). The analysis considers all scenes between 60S and 60N, with cloudiness flag 2 or less, and no precipitation or sea-ice, according to the flags provided by Eumetsat.

## 5 TASK 4: OEM (MWIR/METOP-B) OVER LAND, CLEAR-SKY, WITH VARIABLE EMISSIVITIES

### 5.1 ADDITION OF LAND SURFACE EMISSIVITY TO STATE VECTOR

Emissivity has been included in the state vector in terms of principle components, analogous to the approach used to represent the atmospheric profiles, and following an approach already implemented at RAL in our in-house retrieval schemes.

For this project the principle components have been determined from the fields of assumed spectral emissivity which are used in Tasks 2-3. I.e. they are based on the values defined by RTTOV (v10.2) for the times and locations of the IASI measurements on the three days selected for this study. The spectral covariance of all these emissivity spectra (globally over both land and sea), jointly for AMSU+MHS and the selected IASI channels is determined. The eigenvectors and values of this covariance are obtained and used as the basis of the set of spectral patterns used, and the associated *a priori* covariance. Because RTTOV provides co-located emissivity spectra for both MW and IR ranges, the principle components include correlations between MW and IR, which could enable IASI measurement to constrain the emissivity used in the MW and vice-versa. Also because the values span global variation in a presumably realistic manner, the eigenvalues should provide suitable values to use as diagonal elements of the *a priori* covariance for emissivity. All off diagonal elements of the matrix are set to 0.

Note that in RTTOV MW land emissivity can come from two atlases, either TELSEM [Ref:10] or CNRM [Ref:12] (Sea emissivity is calculated using the FASTEM model independent of the selection of land atlas.) TELSEM is based on SSMI observations (and is the default setting for RTTOV v10.2). The CNRM atlas is based on AMSU A and B. Most work here (unless otherwise stated) is based on the TELSEM Atlas.

Both databases are interpolated in RTTOV to define values in the strong absorbing channels from measurements which are only available in the window channels. The spectral interpolation is (probably) of little importance for the simulation of radiances, but is found to introduce some (presumably numerical) artefacts into the spectral emissivity eigenvectors. We therefore simplify the representation of spectral emissivity in the MW before computing the covariance and eigenvectors as follows:

- AMSU channels 1-3 and 15 are taken as provided by RTTOV.
- AMSU channels 4-14 (all in range 52.8-57.3 GHz) are assumed to have the same emissivity as channel 3 (50.3 GHz)
- MHS channel 1 is assumed to have the same emissivity as AMSU channel 15 (both 89 GHz).
- MHS channel 5 is taken as provided by RTTOV.
- MHS channels 2-4 (in range 157-183 GHz) are assumed to have the same emissivity as channel 5 (190 GHz).

A similar approach is adopted in RTTOV for interpolation of the CNRM atlas, here we apply it to all emissivities (from both land atlases and over sea). This means there are at most 5 independent values which define the emissivity in all 20 AMSU+MHS channels (and hence at most 5 eigenvectors are needed to be fitted in the retrieval).

For IASI, RTTOV uses the Borbas/ University of Wisconsin emissivity database [Ref:11] This is based on a set of 416 eigenvectors of the measured emissivity of a set of natural materials, defined on a 416 point spectral grid spanning a spectral range of 699.3 to 2774.30  $\text{cm}^{-1}$ . Emissivity values are extrapolated at fixed value for the channels in the CO<sub>2</sub> band below 699.3  $\text{cm}^{-1}$ . Spatial distributions of emissivity are determined by fitting these eigenvectors to MODIS observations. Only the first 6 spectral patterns are used for this (due to the limited number of MODIS channels), so only these spectral patterns are represented in the emissivity atlas.

By deriving emissivity patterns from the RTTOV atlases, we can therefore obtain up to 6 characteristic spectral patterns, together with realistic estimates of their variability to use in the *a priori* covariance. A few more patterns might be expected from the joint IASI+MW covariance (potentially adding 5 degrees of freedom), however in practise there is substantial correlation, and we therefore only take the first 6 spectral patterns from this matrix. IASI retrievals may well be affected by additional spectral patterns which are not represented in the atlases. In order to address this, further patterns from the set of 416 Wisconsin eigenvectors are added to the set of spectra to be fitted as follows:

- The 416 Wisconsin patterns, in 416x416 matrix  $\mathbf{W}$ , are interpolated onto the spectral sampling of IASI used in the retrievals (139 channels), defined in 139x416 matrix  $\mathbf{W}_i$ .
- The first six Eigenvalues corresponding to the  $\mathbf{W}_i$  can be obtained from the variability of the associated patterns in the RTTOV climatology. The Eigenvalues associated with the Wisconsin patterns are not known however it is assumed that they should decrease in magnitude in the order in which they are provided by Wisconsin. For what follows it is mainly important that the order of the additional patterns is maintained (so the most likely spectral variations remain occur first in the final set of patterns). We assume that each pattern from number 7 onwards has an eigenvalue which is 1.3 times smaller than the previous pattern.
- Having defined the Eigenvectors  $\mathbf{W}_i$  and associated Eigenvalues  $\omega_i$ . A new set of patterns which are orthogonal to the original six are obtained as follows
  - Each pattern (column  $i=1,416$  of  $\mathbf{W}_i$ ) is scaled by the square root of its Eigenvalue to obtain  $\mathbf{p}_i$
  - The six original patterns are fitted to  $\mathbf{p}_i$  to obtaining the residual pattern

$$\mathbf{p}_i' = \mathbf{p}_i - f(\mathbf{p}_i, \mathbf{R}_i)$$

Equation 4

where  $f(\mathbf{p}_i, \mathbf{R}_i)$  is a simple least squares fit of the six RTTOV based patterns (for the IASI channels),  $\mathbf{R}_i$ , to  $\mathbf{p}_i$ .

- A new spectral covariance is constructed from all 416 residual patterns ( $\mathbf{p}_i'$  for  $i=1,N$ ).
- A new set of Eigenvectors, with appropriately ordered Eigenvalues are obtained by decomposing this covariance matrix to obtain  $\mathbf{W}_i'$ .
- The patterns in  $\mathbf{W}_i'$  are added to the 6 RTTOV based patterns, to obtain the full set  $\mathbf{W}'$  (for both MW+IASI). Elements corresponding to MW channels are assumed to be 0. The combined list of Eigenvalues is also obtained,  $\omega'$ .

In principle this results in a list of 422 patterns, however many of these have numerically negligible Eigenvalue. Only a limited number of these patterns are fitted in the retrieval. The retrieval fits the

	RAL Space STFC Rutherford Appleton Laboratory Harwell Oxford Chilton, OX11 0QX, United Kingdom	Document:	Final Report
		Customer Ref:	ITT 13/207194
		RAL Space Ref:	SSTD1569
		2015-01-29	Page 72 of 120

weights (defined in vector  $\mathbf{v}$ ) of each pattern such that the emissivity modelled in RTTOV,  $\mathbf{e}$ , is given by

$$\mathbf{e} = \mathbf{v} \mathbf{W}'$$

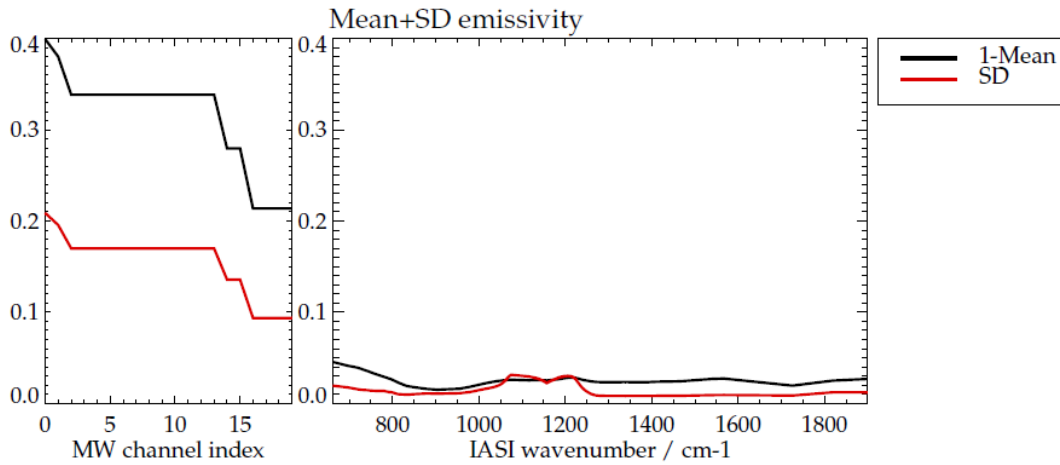
Equation 5

The *a priori* errors for each element of  $\mathbf{v}$  are assumed to be the minimum of the square root of the corresponding Eigenvalue in  $\omega'$  or 0.01 (values smaller than this are not allowed to prevent too tight a prior constraint). The *a priori* covariance is assumed to be diagonal. *A priori* values for  $\mathbf{v}$  are set by fitting the chosen set of patterns to the standard emissivity given by the RTTOV emissivity atlas for a given scene. Differences between this fit and the RTTOV predicted emissivity are small.

A number of options have been investigated as follows:

- Correlations between IASI and MW emissivities can be included or not. In the latter case the first six patterns are determined independently from the IASI channels. Then the first 5 patterns are taken from the RTTOV covariance for the MW channels. Then additional patterns for IASI are added to the list. The user controls the number of IASI patterns fitted the 5 MW patterns are counted in addition, so in results below a retrieval which indicates 20 patterns always includes 20 patterns relevant to the IASI range. If MW correlations are not included then an additional 5 patterns will be included for the MW (25 patterns in all). Note that switching on or off the correlation affects the first 6 patterns in the IASI range, which in turn changes all patterns affecting the IASI range.
- In test retrievals over desert (which are particularly prone to high cost due to presumed issues with RTTOV emissivity), it was noted that fit residuals could be significantly reduced if a pattern representing the first spectral derivative of the Wisconsin mean IASI emissivity spectrum was included in the fit (this has quite sharp gradients in the 10 micron region). This effectively corresponds to fitting a wavelength shift of the mean emissivity. Residuals improve further if pattern representing a wavelength stretch of the mean emissivity is included. We therefore include both these patterns in the main simulations reported here. These are inserted into  $\mathbf{W}'$  in order after the RTTOV based patterns, before the additional IASI patterns discussed above.
- Tests have been run with 10, 20 or 30 patterns (columns of  $\mathbf{W}'$ ) fitted (including 6 RTTOV patterns and the 2 wavelength shift related patterns).

The spectral patterns used are illustrated in Figure 5-1 and Figure 5-2.



Eigenvectors (each offset by 0.25)

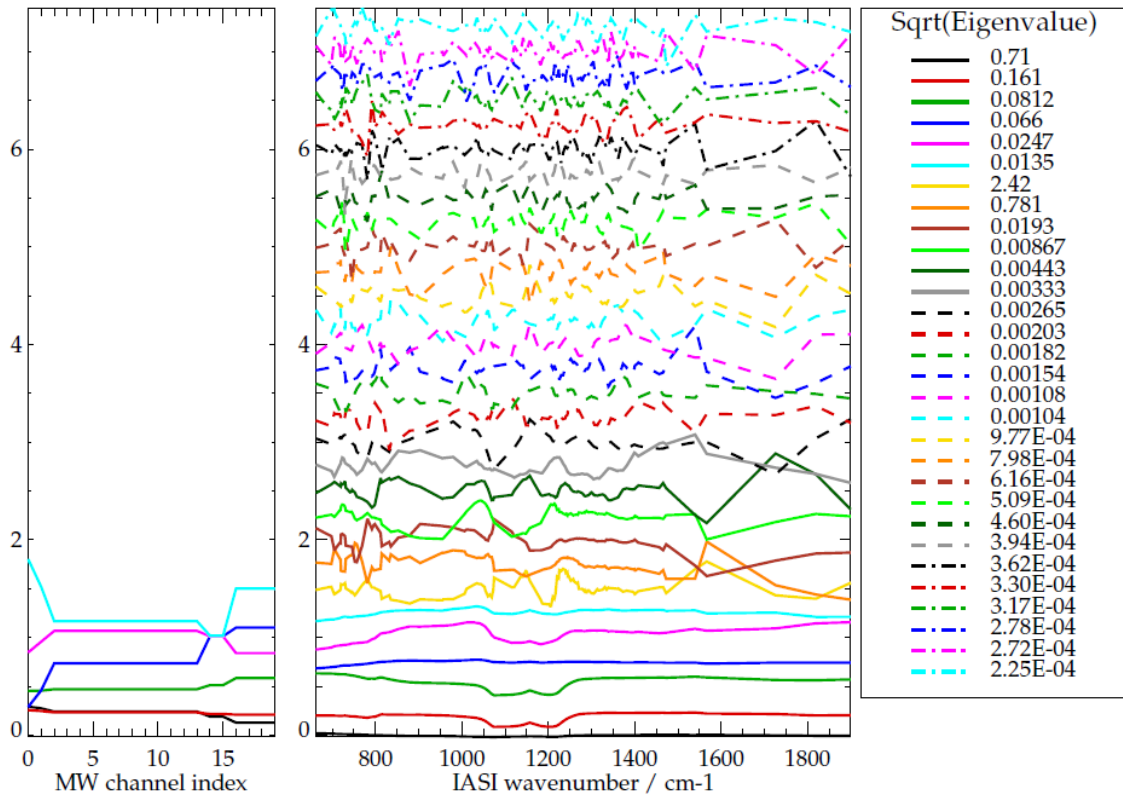
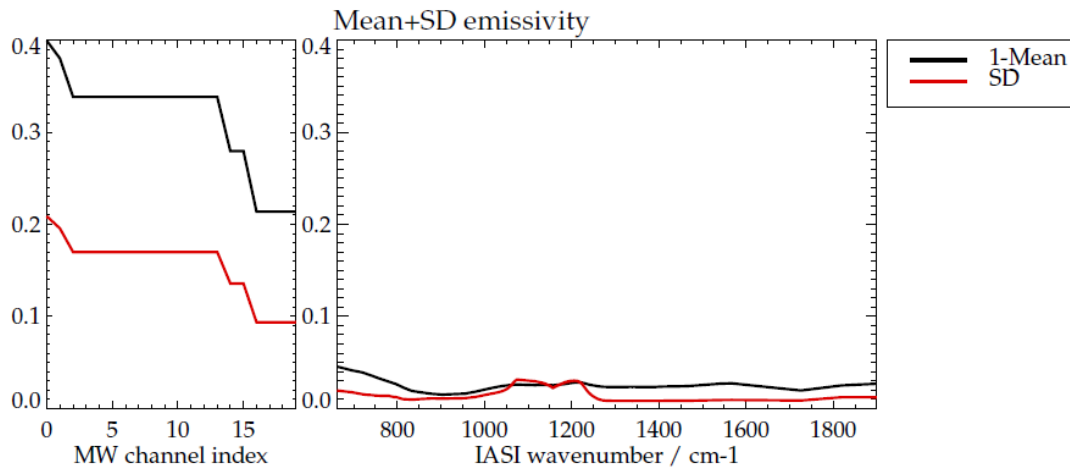


Figure 5-1: Bottom panels shows first 30 spectral patterns used to represent surface emissivity in the retrieval. Each eigenvector is shown offset by 0.25 with respect to the previous vector (for clarity). Only non-zero MW Eigenvectors are shown. The top panels show the mean and standard deviation of the emissivity (note 1 minus the mean emissivity is shown).



Eigenvectors (each offset by 0.25)

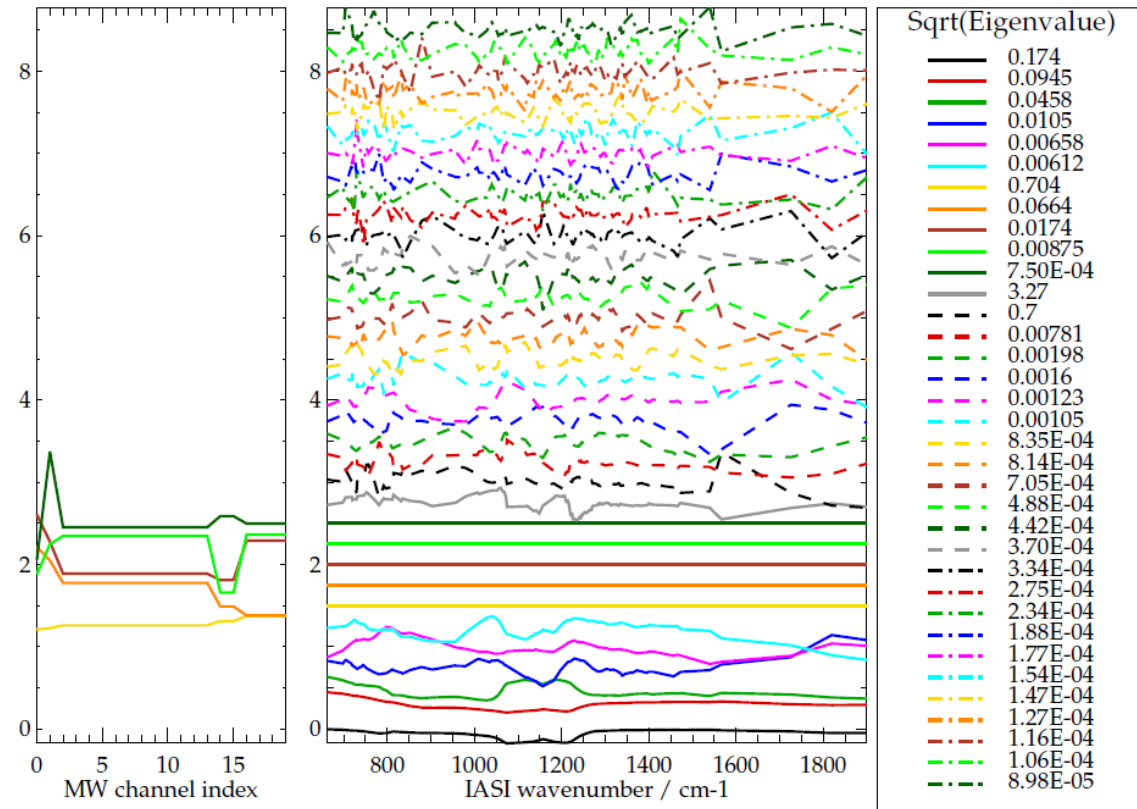


Figure 5-2: As previous figure, when correlation between MW and IASI is ignored.

## 5.2 OEM RETRIEVALS OF MWIR AND STATISTICAL ANALYSIS

### 5.2.1 OVERVIEW OF SIMULATIONS

A series of retrieval experiments have been conducted to assess the performance of the retrieval scheme, with/without emissivity included and with/without MW measurements included. Results are presented here and in the annex to this report from the following retrieval configurations:

In this task we discuss the following retrieval configurations:

- *standard*: IR only, RAL retrieval as close as possible in setting to the EUMETSAT OEM.
- *MWIR*: IR+MW retrieval (no emissivity, no cloud retrieval).
- *MW*: MW only retrieval (no emissivity, no cloud retrieval).
- *Emis:20n*: IR only retrieval, with 20 spectral emissivity patterns retrieved (no emissivity correlations between IR and MW).
- *MWIR; Emis:20*: IR+MW retrieval, with 20 spectral emissivity patterns retrieved. Spectral correlations are assumed between emissivity in IR and MW.
- *MWIR; Emis:20n*: IR+MW retrieval, with 20 spectral emissivity patterns retrieved. Spectral correlations are not assumed between emissivity in IR and MW.
- *Emis:10n*: IR only retrieval, with 20 spectral emissivity patterns retrieved (no emissivity correlations between IR and MW).
- *Emis:30n*: IR only retrieval, with 30 spectral emissivity patterns retrieved (no emissivity correlations between IR and MW).
- *MW; Emis:20*: MW only retrieval, with 20 spectral emissivity patterns retrieved.

All MW retrievals discussed here use full error correlations in the MW measurement covariance. When emissivity is also retrieved, two options are tested for the MW covariance over land:

- 1) As described in the section 4.1, observation – simulation statistics (from the IR retrieval) are used to construct separate covariances and bias correction over land and sea.
- 2) The covariance and bias correction derived for observations over sea is used also over land (i.e. the same covariance and bias correction is used everywhere). This covariance has smaller errors; it is assumed that the larger observation/model deviations found over land are primarily caused by errors modelling emissivity, which should not be included now emissivity is retrieved. This may also be true over ocean, so it may be possible to further reduce the estimated measurement errors, however it is not straightforward to estimate the contribution of emissivity errors to the total estimated error over sea. (These retrievals are usually indicated in plots by the key “MWIR2”.)

Differences between the two versions are usually small, though the second approach has slightly higher information content and slightly better performance; we therefore mainly refer to results from this scheme.

Most retrievals have also been carried out with two prior assumptions:

- Eumetsat piece-wise linear regression (PWLR) used as to define the first guess and *a priori*, as used in the Eumetsat OEM.
- A zonal mean climatology is used to define the *a priori*. This “climatology” is constructed as 10 degree zonal means from the 3 days of ECMWF analysis data provided by Eumetsat for this study. In this case the mean of all profiles in each 10 degree zonal bin, over all three days, are used as the *a priori* profile for a given scene (the 10 degree profiles are assigned to the middle latitude of the bin and profiles are interpolated linearly to the latitude of a given observation). No time dependence is modelled in the climatology. The global covariance of differences between the zonal mean field and the individual ECMWF profiles is used as the *a priori* covariance. The state is actually represented in terms of eigenvectors of this covariance, with variances of the diagonal *a priori* covariance errors given by the corresponding eigenvalues. The profiles, eigenvectors and eigenvalues are shown in figure Figure 5-3. The same number of Eigenvectors are used as in the standard retrieval (28 for temperature, 18 for water vapour and 10 for ozone). No correlations between temperature / water vapour / ozone are assumed. For surface temperature, a similar approach is used: The *a priori* values is the zonal mean value from the three days (interpolated in latitude), and the *a priori* error is the standard deviation of the individual values from this zonal mean, which is approximately 8.6K.

This “climatological” prior is used as an alternative here, to test the performance of the retrieval when given a looser (and less accurate) prior constraint that provided by the PWLR. Certain retrieval options may be expected to show greater impact under these conditions. It is also the case that the, with the climatological prior, the retrieval averaging kernels are unambiguously defined. When PWLR is used, measurements have been effectively used twice (once to obtain PWLR and once in the OEM). Averaging kernels are only determined for the OEM step and so do not characterise the full sensitivity of the result to the measurements and it is therefore not completely correct to expect agreement between the retrieval and the analysis smoothed by the averaging kernels (applying Equation 3) . Using the climatological constraint removes this ambiguity, but I might be expected that the absolute quality of results will be degraded (because in general the PWLR results are in very good agreement with analysis).

Results from all these retrievals are shown in the plot annex to this report.

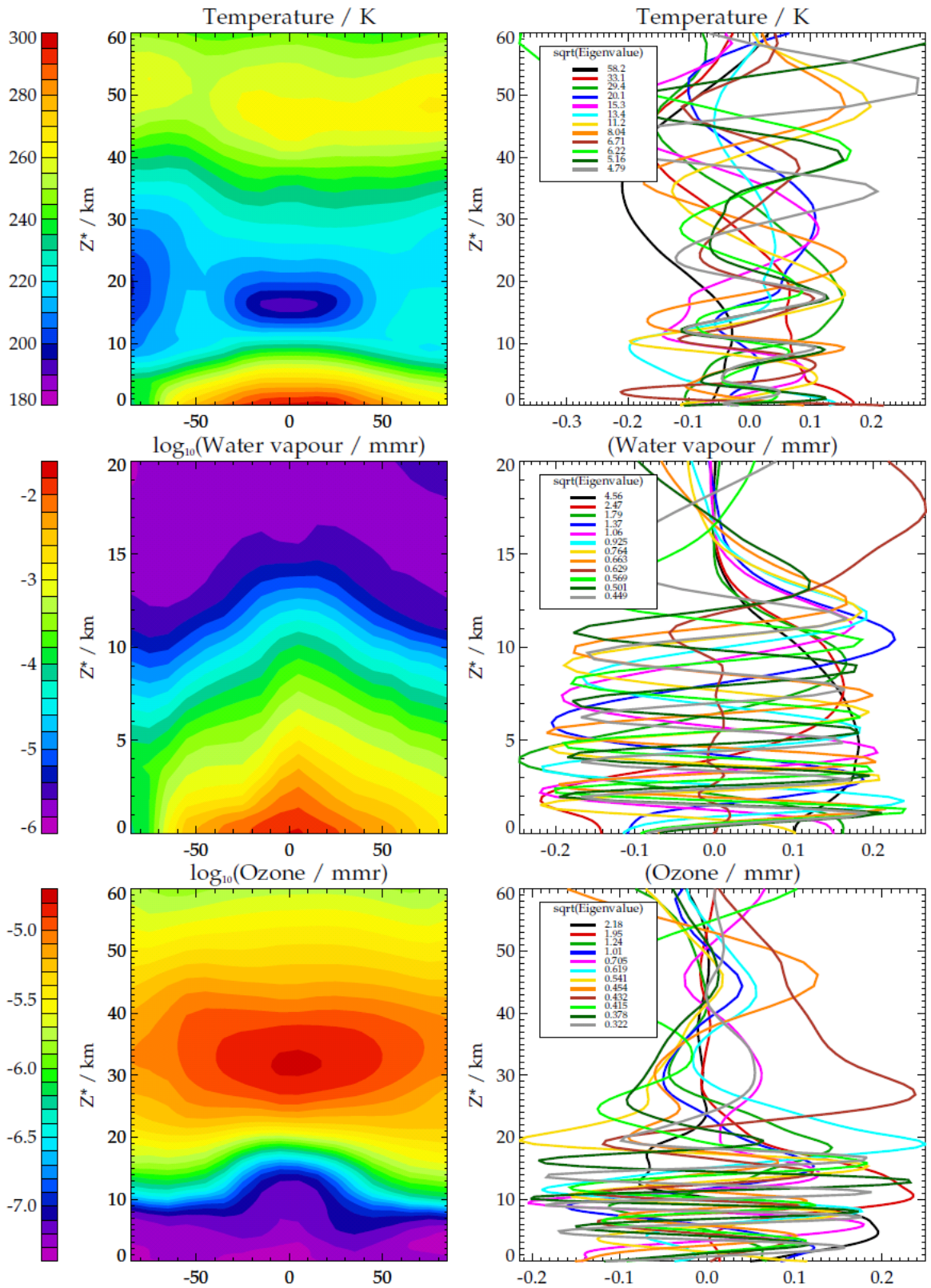
## 5.2.2 COMPARISONS OF OBSERVED AND SIMULATED SPECTRA USING DIFFERENT EMISSIVITY ATLASES

Section 4 of the plot annex contains additional plots comparing observations with simulations. Results are shown for spectra binned by latitude, view zenith angle and by solar zenith angle. Comparisons are made between measurements and simulations based on the PWLR profiles and on retrieved profiles from a range of options. PWLR simulations are performed using either the TELSEM of CNRS MW emissivity atlas. All retrievals are performed using TELSEM.

From these figures, the following points are noted:

- Simulations with PWLR show that mean agreement with observations is different over land and sea. This is the case for both TELSEM and CNRS (land) atlases. The difference in bias is slightly smaller for CNRM, however the CNRM atlas leads to generally higher standard deviation in the differences (more scatter). Since we apply bias correction to MW observations used in retrievals, we prefer to continue using the TELSEM atlas as the improved standard deviation is most likely more useful than the slightly smaller bias before correction.
- The bias over land depends strongly on solar zenith angle, i.e. on whether observations are made the day-time or night-time overpass. A corresponding pattern in bias is also present for the IASI simulations from PWLR (e.g. see fig 13 of the annex). IASI window channels have a positive bias over land in day-time, while the first two AMSU channels are negatively biased with respect to the night-time case (actually bias is positive at night and close to zero during daytime). This difference is difficult to reconcile physically, and the day/night difference is not currently included in the bias correction applied in retrievals (this only models land/sea and view zenith dependent bias).
- As might be expected from the above, when results from IASI retrievals are used to model MW radiances, the divergence in MW bias between day and night increases (fig 15).
- The joint MWIR retrieval also cannot resolve this issue, and day/night differences in bias over land remain, while those over sea are reduced to near zero (fig 16).
- When emissivity is jointly retrieved however the window channels are much better fitted (figs 17 and 18), with reduced bias land/sea/day and night, and reduced standard deviations. Results are slightly better when correlations are not assumed between the MW and IR emissivity patterns (fig 18). However it is unlikely that this improvement has been made with consistent values of retrieved emissivity over the same land locations when observed in daytime vs night-time. I.e. there remains an unresolved inconsistency in the diurnal variation observed over land in the IASI and MW window channels, which probably affects the quality of combined retrievals over land in particular.
- The bias in IASI window channels during day time could be caused by errors in the RTTOV predicted emissivity (which one would hope retrieval of emissivity might correct), or could be explained by errors in the PWLR. One mechanism for errors in PWLR could involve error in representing the diurnal variation of surface (or near-surface) temperature in the training data, which would particularly affect day-time retrievals over land.

We currently keep the approach adopted in task 2 and 3, and used the TELSEM emissivity in retrievals (when emissivity is not retrieved). We also continue to bias correct the MW radiances using the differences of MW observations from simulations based on the IR only retrieval (as described in section 4.1).



17:46 13/07/14

Figure 5-3: Zonal mean fields (left) and Eigenvectors/values of the departures of the ECMWF analysed profiles from the zonal mean, as used to define the “climatological” prior constraint used in some retrievals.

### 5.2.3 EXAMPLE RETRIEVALS WITH EMISSIVITY INCLUDED

Retrievals over desert are particularly problematic for the standard OEM, particularly in the day-time. Typically retrievals lead to relatively high cost, and anomalously high values of tropospheric ozone are retrieved. This behaviour is likely to be related to the strong spectral variations of the desert surface emissivity, particularly in the 10 micron region (around the ozone band).

Initial test of the emissivity retrieval were therefore carried out for a selected desert scene (mainly over Egypt). Results from some tests are shown in figures Figure 5-4- to Figure 5-7. Each figure shows the following:

- Top left: “pink” false colour plot constructed from IASI channels near 8.9, 11 and 12 microns. This is a standard false-colour combination used for SEVIRI, in which desert dust plume tend to appear as pink/magenta.
- Jy: measurement cost
- Nstep: number of retrieval steps (including bad Marquardt Levenberg “tries”)
- The for each state parameter TS (surface temperature), T (temperature profile), W (water vapour profile) and O (ozone profile):
  - Ret: The retrieved value.
  - Ret-ANA\_AK: Difference between retrieval and analysis smoothed by averaging kernel.
  - PWLR-ANA\_AK: Difference between PWLR and analysis smoothed by averaging kernel.

For T,W and O the mean value and mean difference shown is averaged over the lower troposphere (LT), i.e.  $Z^*$  is 0-6km above the surface.

Figure 5-4 shows the standard retrieval, shows cost function values around 1000 (where 100 is more typical of other surface conditions). Sometimes many steps are needed to obtain convergence.

Figure 5-5 shows the corresponding results with 10 emissivity patterns fitted (still only using IASI). Cost function values are typically halved, and the number of steps much reduced. Tropospheric ozone values are also reduced to somewhat more realistic values.

Figure 5-6 shows results with 20 patterns fitted. Cost function values are further reduced (to around 300), as is the tropospheric ozone. Figure 5-7 shows results with 30 patterns fitted. These are quite similar to those with 20 patterns fitted. Most retrievals have therefore been conducted with 20 emissivity patterns.

Water vapour and temperature are not strongly affected by the inclusion of emissivity, or the number of patterns fitted.

Figure 5-8 shows measurements / simulations and fit residuals for the standard retrieval from one of the retrievals (near the centre of the scene). Figure 5-9 show corresponding results for the 20 pattern emissivity retrieval, together with the fitted emissivity spectra, which are compared to that predicted by the RTTOV atlas.

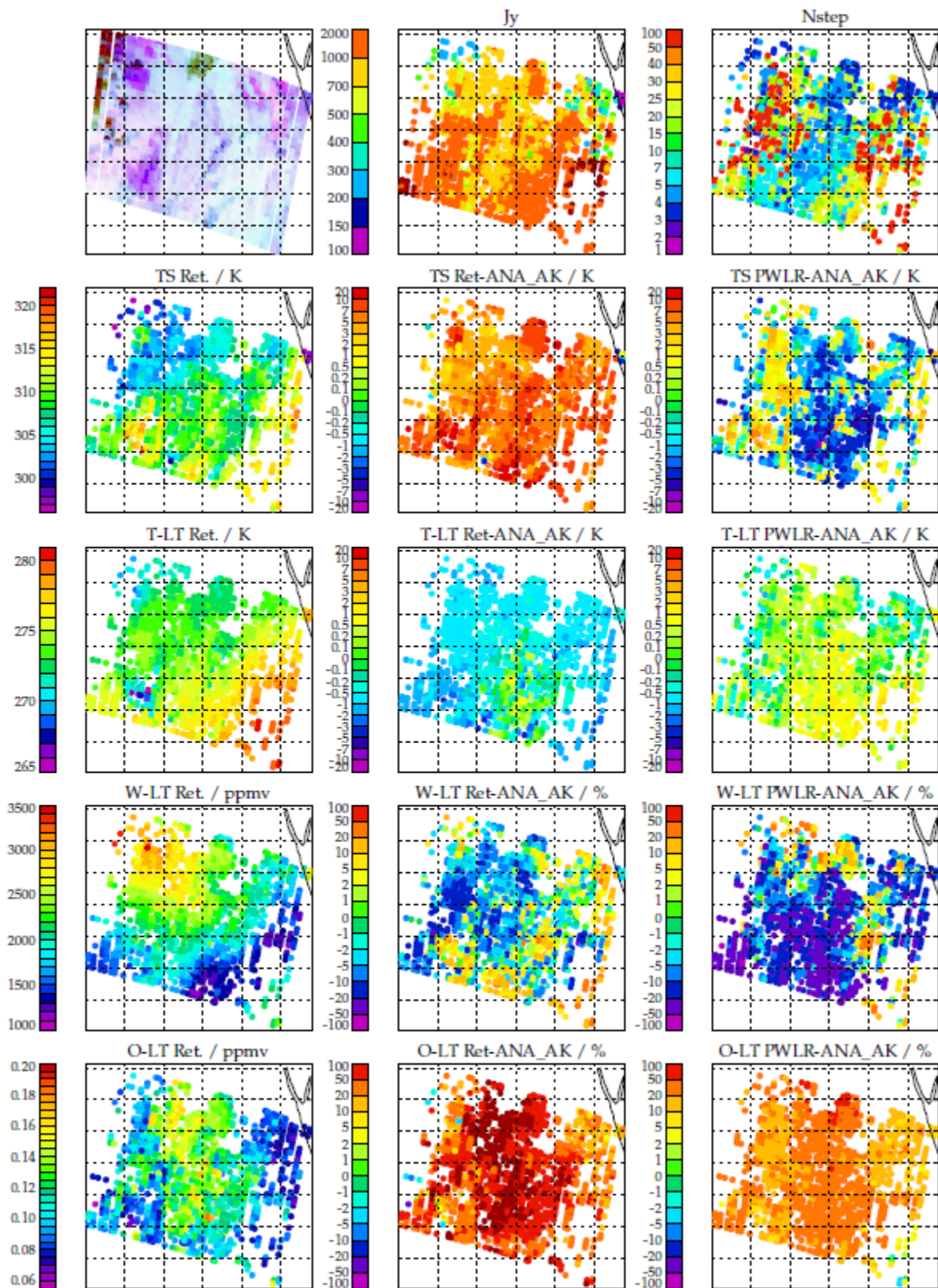
The robustness of the emissivity retrieval has been tested by running retrievals in which the a priori emissivity spectrum is set to 1 (spectrally independent), as opposed to using the RTTOV atlas emissivity spectra as the prior state. Results from this retrieval for the example scene are shown in Figure 5-10. The retrieval gives a very similar emissivity spectrum fit cost (and solution atmospheric state) with this prior, confirming that the retrieval seems to be rather stable.

Global maps of emissivity are presented in the plot annex, and are also illustrated in Figure 5-15. In general departures from RTTOV values are small; the emissivity tends to be bounded reasonably well in the expected range (values do not typically exceed 1 by more than  $\sim 0.02$ ). Also departures from RTTOV show broadly similar patterns in the day and night overpasses.

Despite the strong improvement introduced in desert scenes, systematic fit residuals remain, indicating scope for further work to improve the spectral patterns used in the fit.

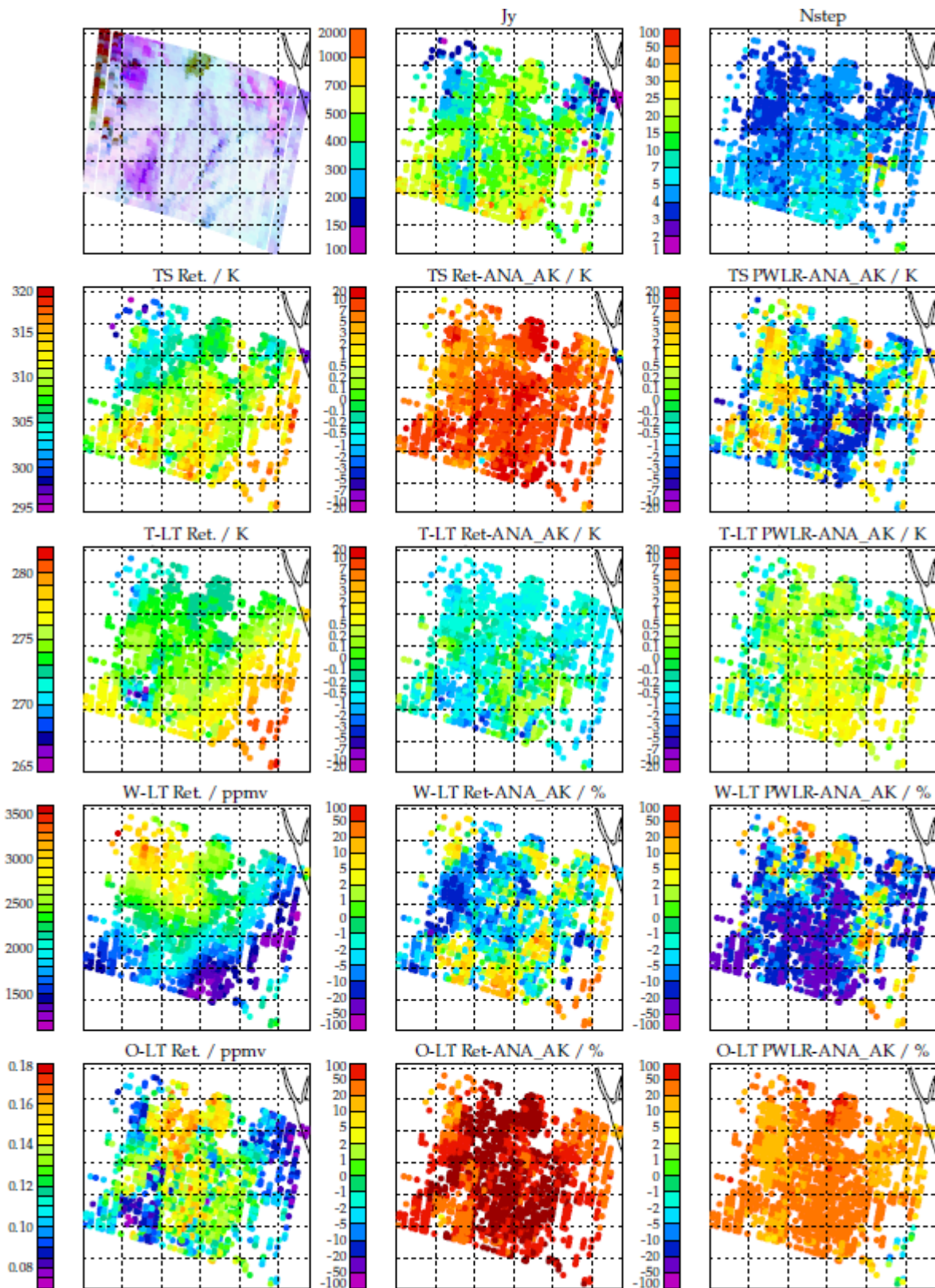
#### 5.2.4 RETRIEVAL OF IR BIAS CORRECTION SCALE FACTORS

While the addition of emissivity to the state vector is found to considerably reduce cost over desert, it was noted that cost remained relatively high over cold (ice/snow) surfaces. Some experimentation was carried out in an attempt to inject into the fitted patterns variations in ice/snow spectral emissivity based on available information from the literature, however it was confirmed that already the existing patterns contained the expected spectral shape of ice/snow (adding further patterns did not change the quality of the fit). It was however noted that residuals over ice/snow were smaller if the Eumetsat prescribed IR spectral bias correction was *not* applied, presumably indicating that the FM errors which this seeks to address are scene dependent, probably related to water vapour spectral features. To address this, the option to retrieve scale factors for the two bias correction vectors  $\mathbf{b}_0$  and  $\mathbf{b}_1$  (see section 2.4) was introduced into the retrieval. This resulted in a retrieval scheme which has generally reduced cost (see Figure 5-13). Introduction of the bias correction factors into the retrieval seems to have no adverse impact on the scheme, so this is enabled by default in most retrievals reported in later work, including task 5,6). The summary tables in section 7 of the annex contain statistics which confirm this. Example maps of the fitted parameters are shown in Figure 5-14. As expected the scaling factor for pattern  $\mathbf{b}_0$  has little scan angle dependence, whereas that for  $\mathbf{b}_1$  clearly shows across-swath structure. Both terms tend to low values towards high latitude.



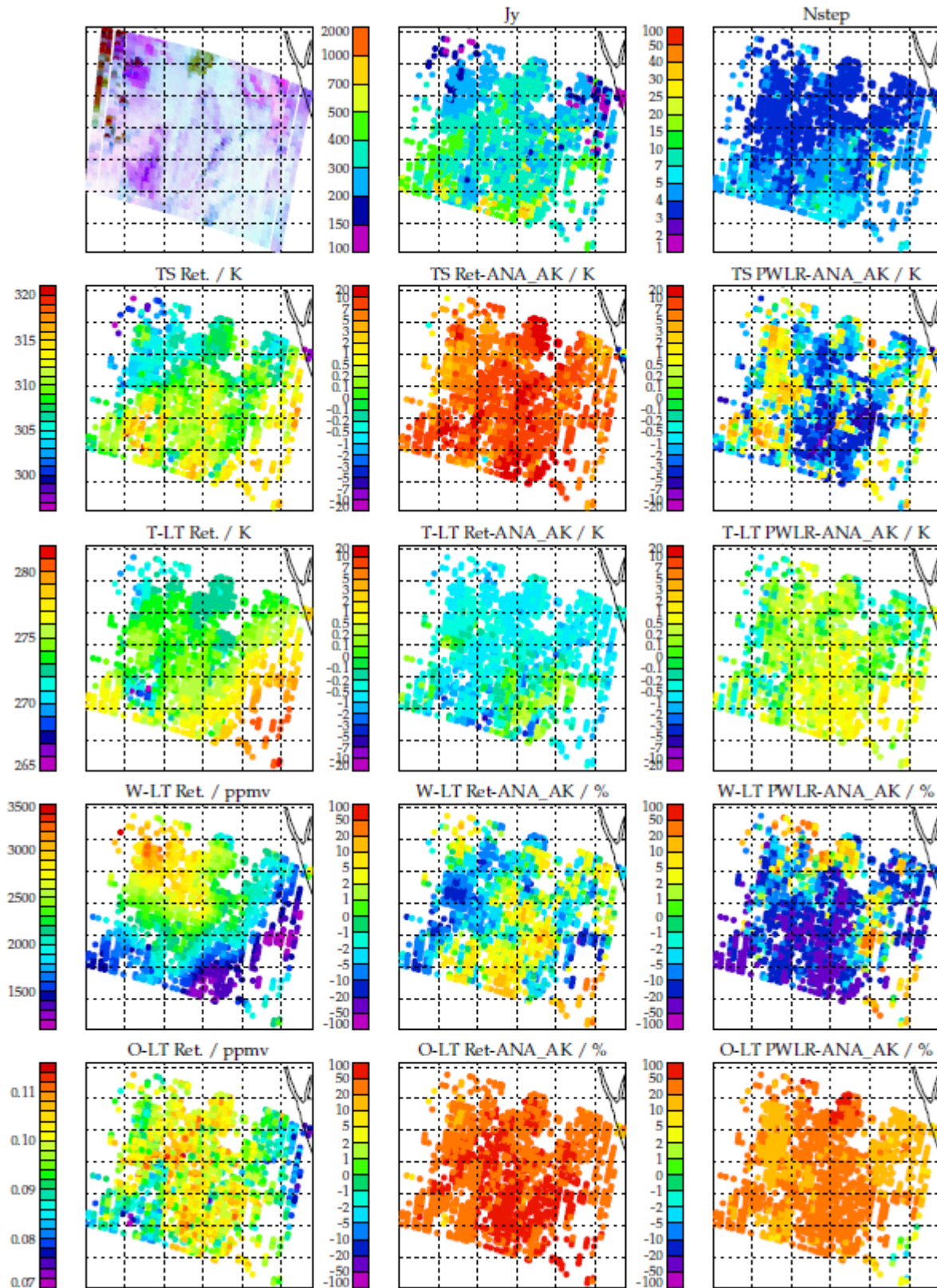
v1p3/output/20130417081200Z\_20130417081455Z\_N\_C\_20130417095338Z\_isamp1.str

Figure 5-4: Example retrieval over desert. Standard retrieval configuration (emissivity from RTTOV).



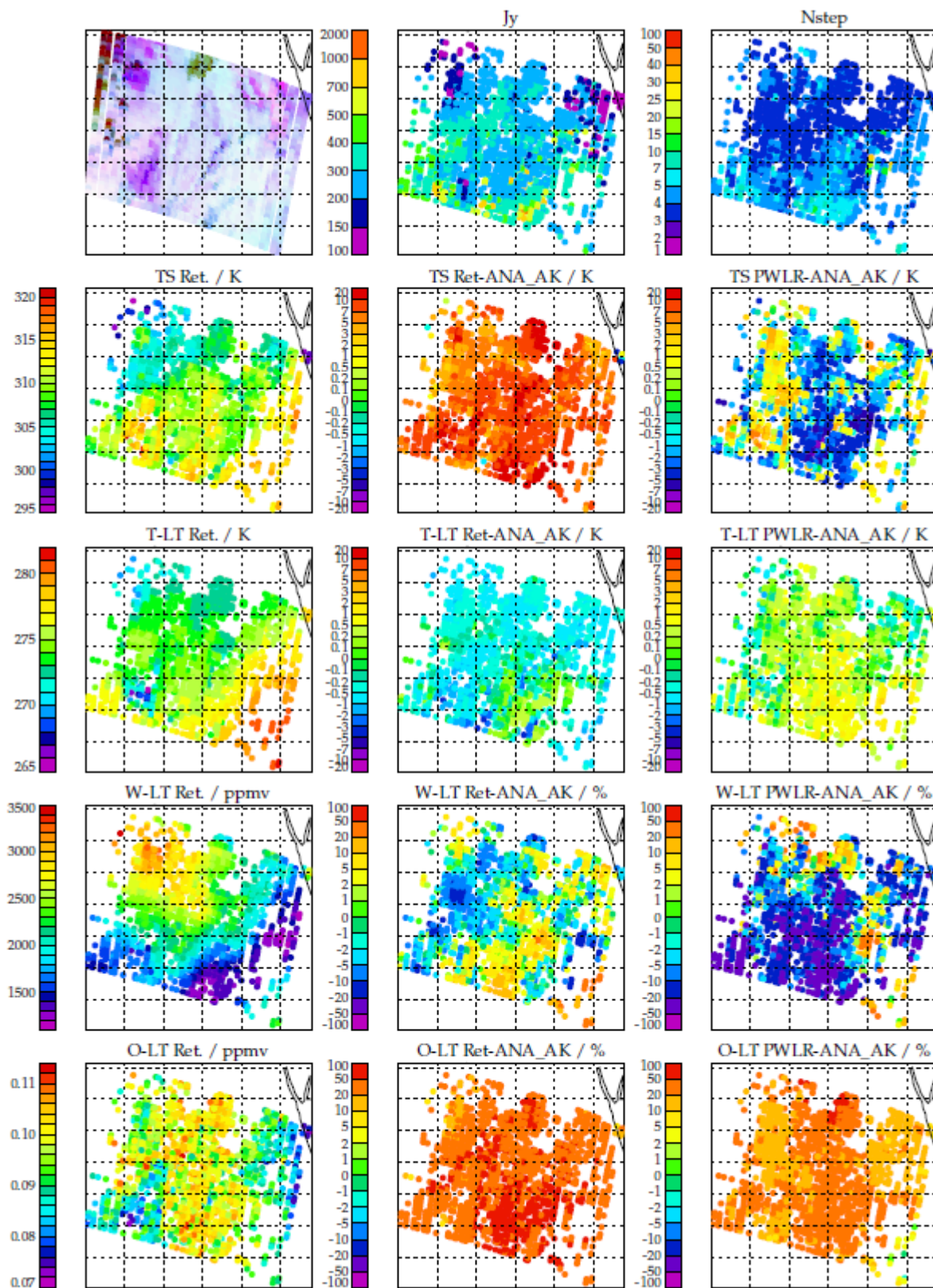
v1p3/output\_rem10-nmi/20130417081200Z\_20130417081455Z\_N\_C\_20130417095338Z\_isamp1.str

Figure 5-5: Example retrieval over desert. 10 emissivity patterns retrieved



v1p3/output\_rem20-nmi/20130417081200Z\_20130417081455Z\_N\_C\_20130417095338Z\_isamp1.str

Figure 5-6: Example retrieval over desert. 20 emissivity patterns retrieved



v1p3/output\_rem30-nmi/20130417081200Z\_20130417081455Z\_N\_C\_20130417095338Z\_isamp1.str

Figure 5-7: Example retrieval over desert. 30 emissivity patterns retrieved

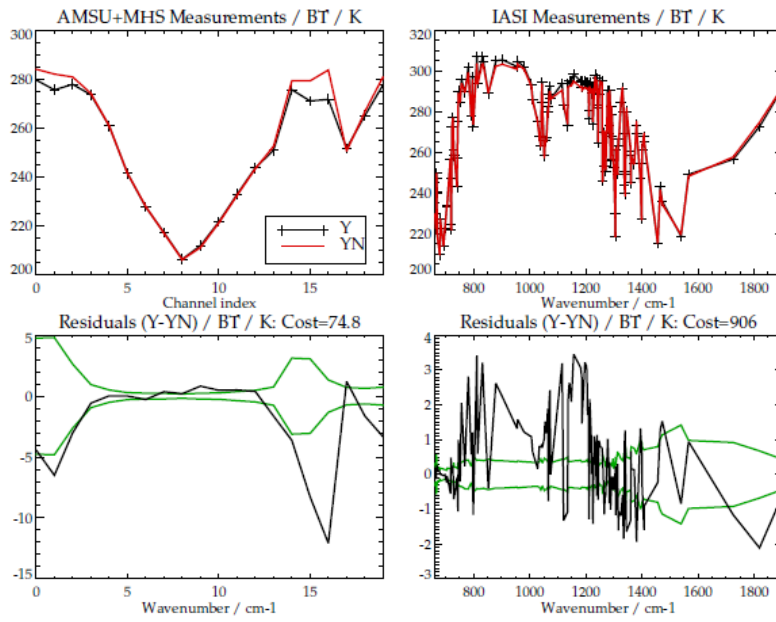


Figure 5-8: Measurements and residuals for standard retrieval in centre of scene shown in Figure 5-4. AMSU+MHS not fitted.

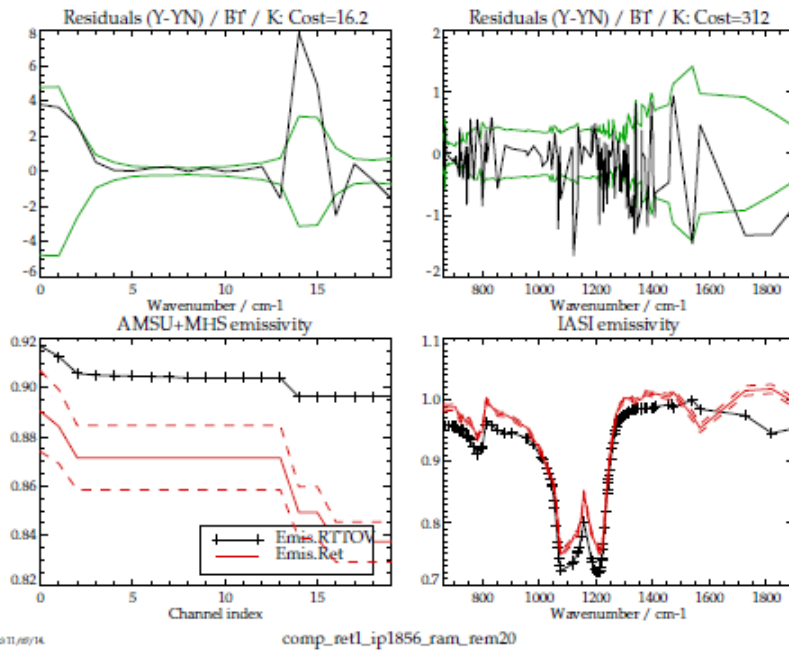


Figure 5-9: Measurements, residuals and RTTOV + fitted emissivity spectra for same scene as previous figure. For retrieval including 20 emissivity patterns. Dashed lines in the emissivity panels show the estimated error in the retrieved emissivity. AMSU+MHS also fitted.

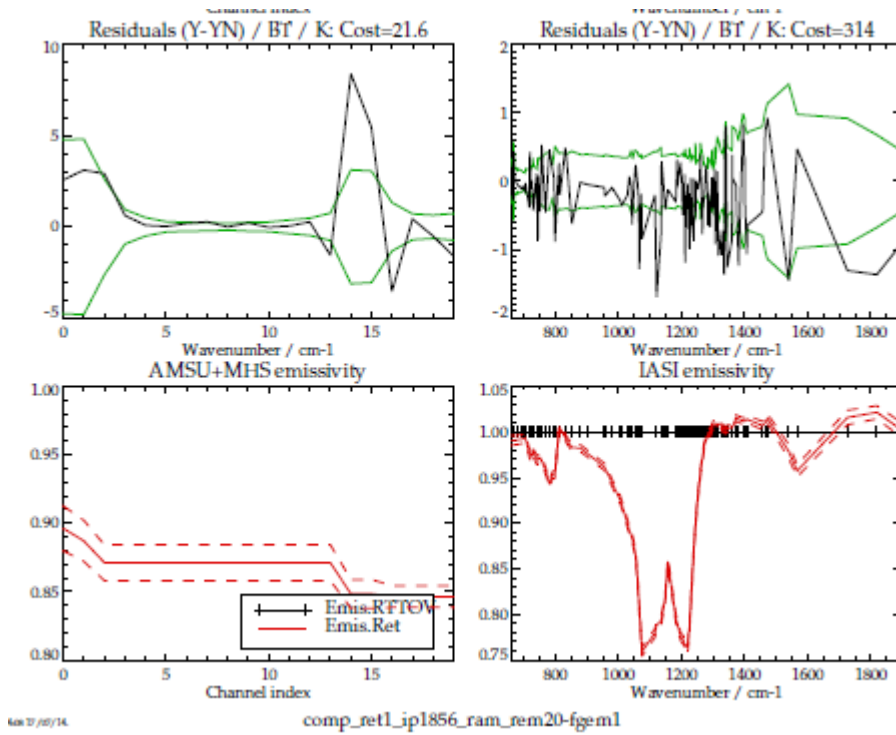


Figure 5-10: Measurements, residuals and RTTOV + fitted emissivity spectra for same scene as previous figure. For retrieval including 20 emissivity patterns. A priori emissivity set to 1 (spectrally uniform). Dashed lines in the emissivity panels show the estimated error in the retrieved emissivity. AMSU+MHS also fitted.

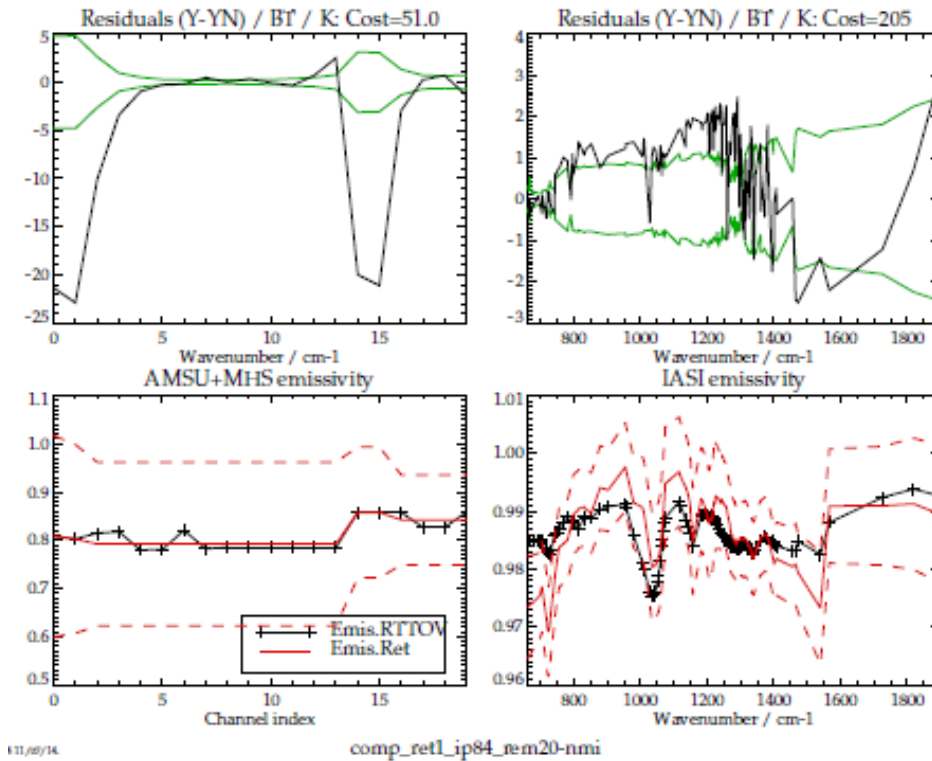


Figure 5-11: Measurements, residuals and RTTOV + fitted emissivity spectra for scene over Greenland. Emissivity retrieved.

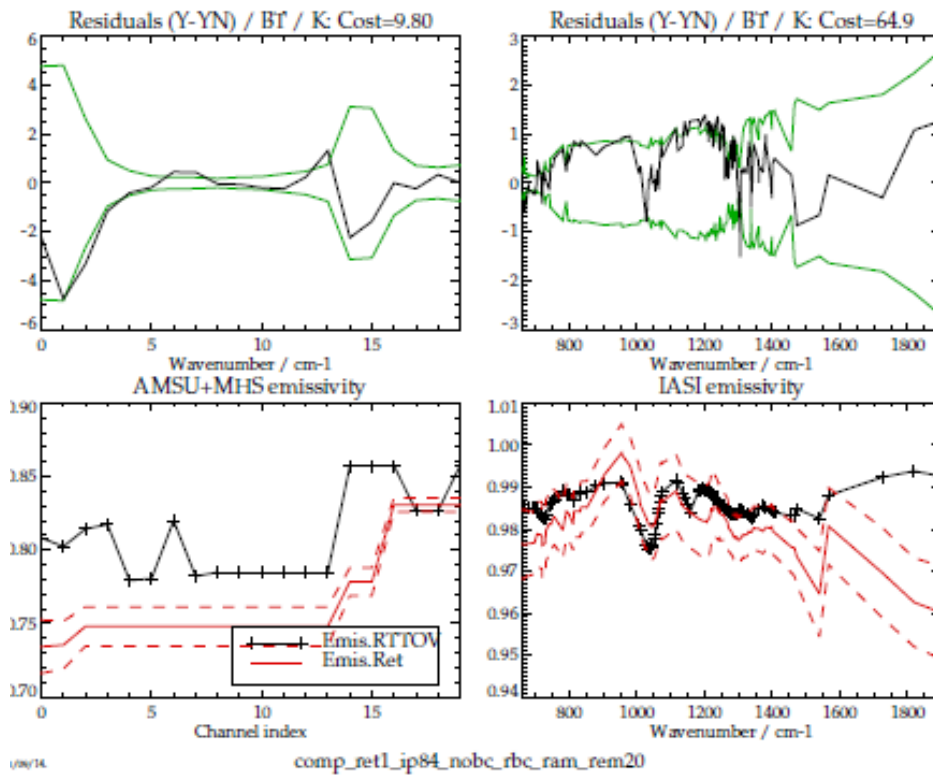


Figure 5-12: Measurements, residuals and RTTOV + fitted emissivity spectra for scene over Greenland. Emissivity and bias correction scale factors retrieved.

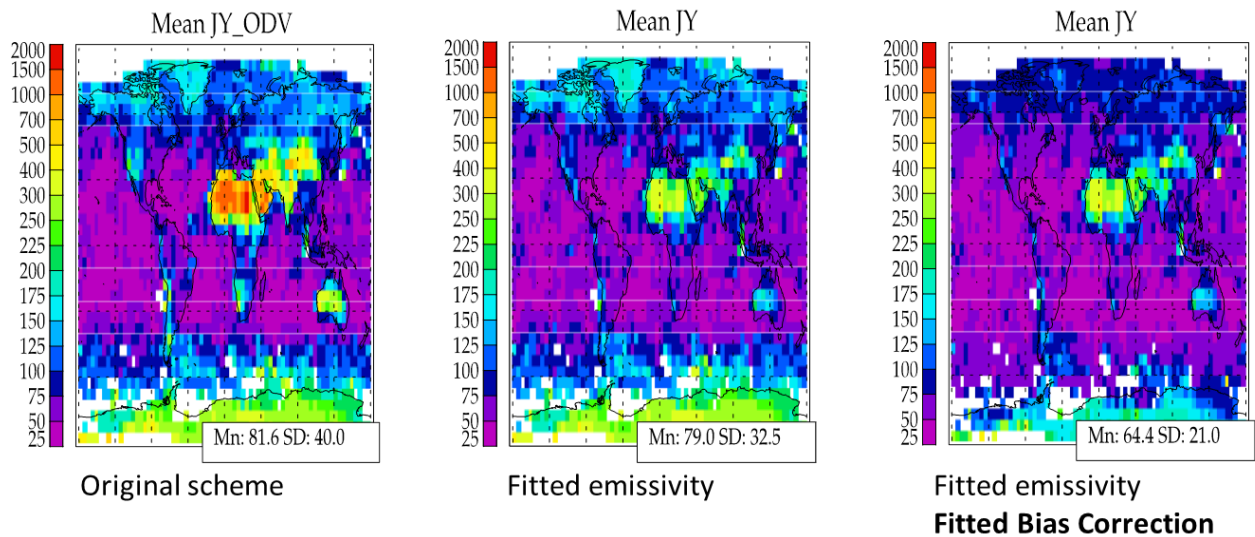


Figure 5-13: Measurement cost function values for the standard IR only scheme (left), IR scheme with fitted emissivity (centre) and IR scheme with fitted emissivity and IR bias correction scale factors (right). Maps consider results for all 3 Metop B days, day+night.

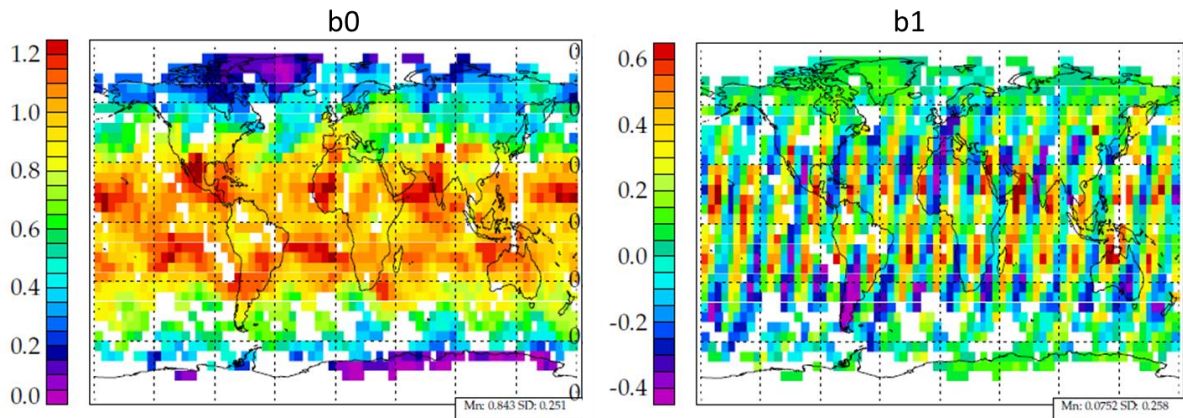


Figure 5-14: Maps of the retrieved bias correction scale factors for vectors b0 (left) and the scan dependent term b1, right. Results shown are 5 degree gridded means of cloud-free day time retrievals on 17 April 2013.

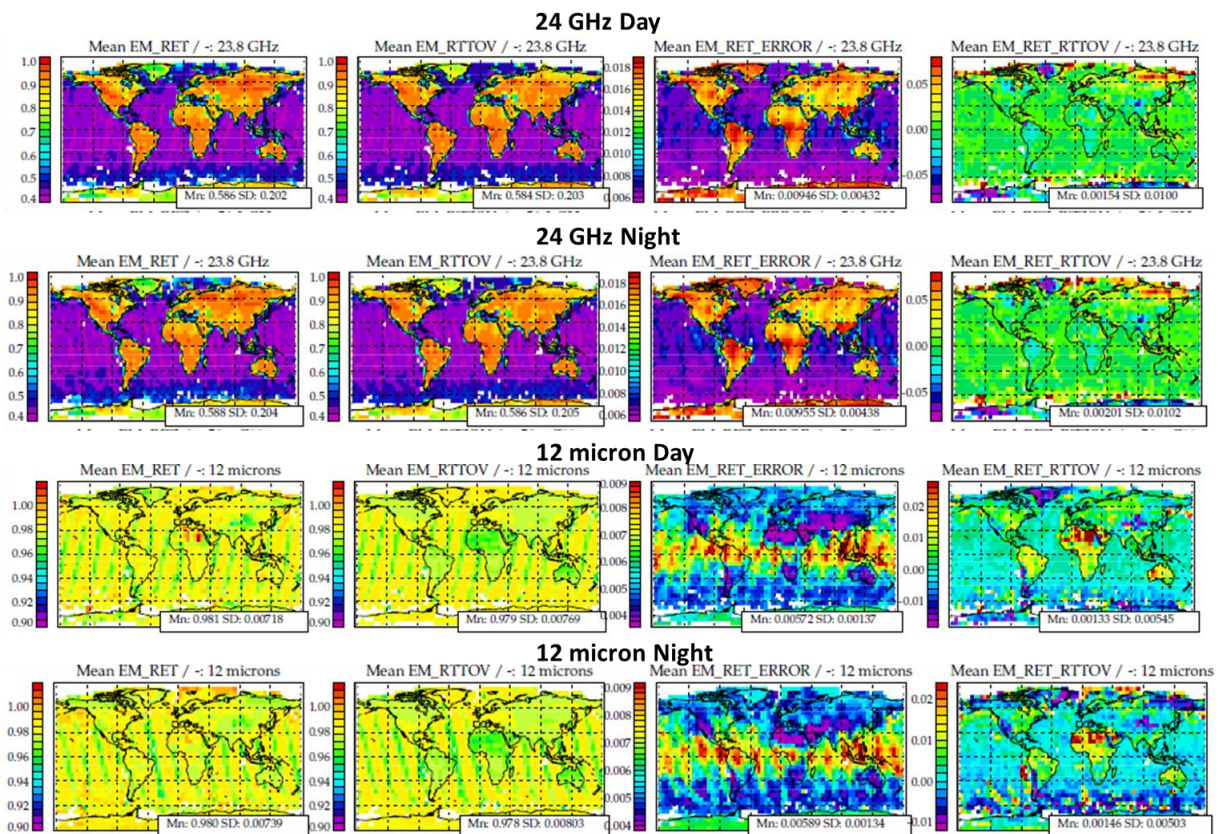


Figure 5-15: Maps of the retrieved emissivity, compared to RTTOV atlas values. Top two rows show, respectively, results day-time and night-time at 25GHz; Bottom two rows show corresponding results at 12 microns. From left-right panels show: retrieved emissivity; RTTOV emissivity; the ESD for emissivity; the difference between RTTOV and retrieved emissivity.

## 5.2.5 IMPACT OF EMISSIVITY RETRIEVAL ON TEMPERATURE AND HUMIDITY

Figure 5-16 shows results analogous to those in Figure 4-6, but in this case MWIR results include joint retrieval of emissivity. Results for temperature are hardly changed at all, but for humidity there is a significant improvement from fitting emissivity in the lower troposphere (<3km), over land. Standard deviation compared to analysis is reduced from 25 to 20%. Results are shown here for the MWIR scheme, but similar performance is achieved for the IR-only scheme. Summary tables in section 7 of the annex show that this is a robust effect, independent of the whether PWLR or climatology is used as prior, or of the option selected for the MW measurement covariance.

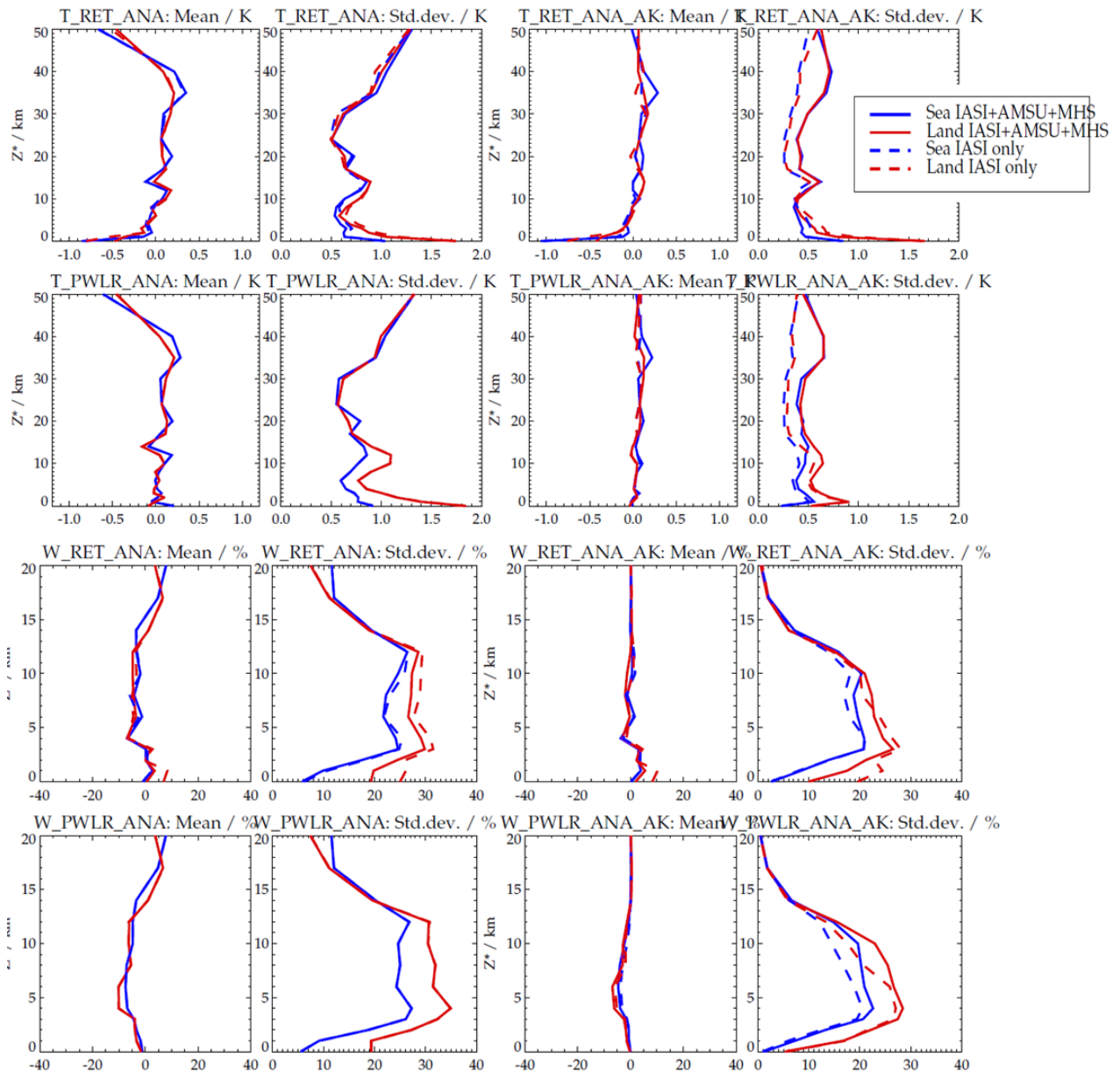


Figure 5-16: Summary of differences between standard IR and MWIR retrieval, PWLR and analysis. MWIR includes joint retrieval of surface emissivity. Top two rows show results for temperature; bottom two rows for water vapour. Red curves show results for land and blue for sea. Dashed lines show the IR only results, solid lines MWIR. Panels are presented in pairs, with the left and right hand panel showing, respectively, the mean and standard deviation of the difference between retrieval and analysis (RET\_ANA), PWLR and analysis (PWLR\_ANA), retrieval and analysis smoothed by the averaging kernels (RET\_ANA\_AK), PWLR and analysis smoothed by the averaging kernels (PWLR\_ANA\_AK). The analysis considers all scenes between 60S and 60N, with cloudiness flag 2 or less, and no precipitation or sea-ice, according to the flags provided by Eumetsat.

## 6 TASK 5: OEM(MWIR/METOP-B) IN PARTIAL OR FULL CLOUDY IFOVS

In this work package cloudy pixels are introduced to the retrieval. Operational products are used to segment scenes by cloudiness. A series of flags are cloud related quantities are available in the IASI L1 and L2 products. Here we focus on a few of the parameters given by the version 6 L2 products (refer to the IASI level 2 Product Guide [Ref:3] ). The primary indicator of cloud used here is the cloudiness flag “FLG\_CLDTST”. Possible values of this cloud flag are: 1 (clear), 2 (presumably clear), 3 (partly cloudy), 4 (fully cloudy). In particular scenes with cloudiness flag 1 or 2 are analysed in the previous work of this study. The work of task 5 focuses on extending and characterising the performance of the OEM for scenes with cloudiness 3 and 4. In order to further segment scenes the L2 cloud fraction and cloud top pressure are also used.

Within this task the OEM is extended to make allowance for the presence of cloud in two ways:

- The method of McNally and Watts [Ref:14] is used to identify channels which are affected by cloud, such that individual channels rather than whole spectra can be screened.
- RTTOV’s simple black-body model for cloud is used in the FM and the fraction of pressure of the cloud is retrieved.

The quality of the retrievals in cloudy scenes is assessed by comparison to ECMWF analysis, as in the previous tasks.

### 6.1 MCNALLY-WATTS METHOD (WMC)

The McNally-Watts cloud detection scheme (here referred to as the WMC scheme) attempts to identify spectral channels which are unaffected by cloud, rather than find completely cloud-free scenes. In this way observations in a sub-set of cloudy scenes can still be used, even if the information content of the observations is reduced compared to cloud-free conditions.

The approach consists of three main steps (also illustrated in Figure 6-1):

1. For a given measurement, a clear-sky RT simulation is performed based on the best available knowledge the atmospheric state. In [Ref:14] this is taken from short-range NWP forecasts. Here we use the PWLR results.
2. Considering cloud as a black body situated at a given altitude, the sensitivity to cloud of each channel as a function of altitude is determined. This can be obtained from output, which is automatically computed by RTTOV at step 1 (overcast radiances). The lowest altitude at which each channel can be considered to be unaffected by cloud is identified.
3. The difference between observations and measured radiances (i.e. departures) are ordered in decreasing order of the assigned channel cloud-altitude-sensitivity. In this ordering it is expected that differences will be small until the assigned channel altitude is at or below the altitude of a cloud (if present). At this point the difference should (mainly) increase or decrease monotonically (depending on the temperature of the cloud compared to the underlying surface). The scheme attempts to identify where these cloud induced departures

	RAL Space STFC Rutherford Appleton Laboratory Harwell Oxford Chilton, OX11 0QX, United Kingdom	Document:	Final Report
		Customer Ref:	ITT 13/207194
		RAL Space Ref:	SSTD1569
		2015-01-29	Page 92 of 120

start to occur. Channels with altitude sensitivity above this point can be considered cloud unaffected.

Steps 2 and 3 are dependant of a number of settings, which can be varied to alter the sensitivity of the approach. This is particularly true for step 3, where a number of complicating factors arise, in particular:

- Cloud extinction is wavelength dependent, so it may be beneficial to consider distinct spectral bands (e.g. long-wave CO<sub>2</sub>, short-wave CO<sub>2</sub>, water vapour bands, ozone band).
- Vertical structure in cloud is coupled to vertical structure in temperature, and the T/p dependence of line-shapes means that departures are not strictly monotonic, so low pass filtering of the ordered radiances is required. Obtaining a clean monotonic signal may include tuning the channels, which are used as well the properties of the low pass filter. Once a clean signal is obtained, threshold values need to be defined (based on gradient and absolute departures) to identify where the departure occurs.

To avoid a length exercise to optimise these settings for this particular application, we directly use the NWPSAF cloud detection code, obtained from ([https://nwpsaf.eu/deliverables/IR\\_aerosol\\_cloud\\_detect/](https://nwpsaf.eu/deliverables/IR_aerosol_cloud_detect/)), together with its default settings for IASI. These are presumed to be the settings operationally used at ECMWF (tbc). This implements step 3 of the above scheme. Step 2 is implemented as described in [Ref:14] . Note the following aspects of this implementation:

- For IASI, only long-wave CO<sub>2</sub> channels are used in the test. The cloud-sensitivity-altitude derived from these channels is transferred to the other bands.
- The scheme depends on using a specific set of channels. Using the channels of the OEM scheme results in much degraded (less monotonic) sets of departures and hence poorer detection performance. We therefore run RTTOV for both sets of channels (the standard WMC channels and the OEM channels). The cloud-sensitivity-altitude is first identified from the WMC channels, after which all OEM channels with sensitivity below this value are subsequently ignored in the retrieval.

Channels are “ignored” by setting their respective measurement errors to a very large value (variance  $1 \times 10^{19}$ ).

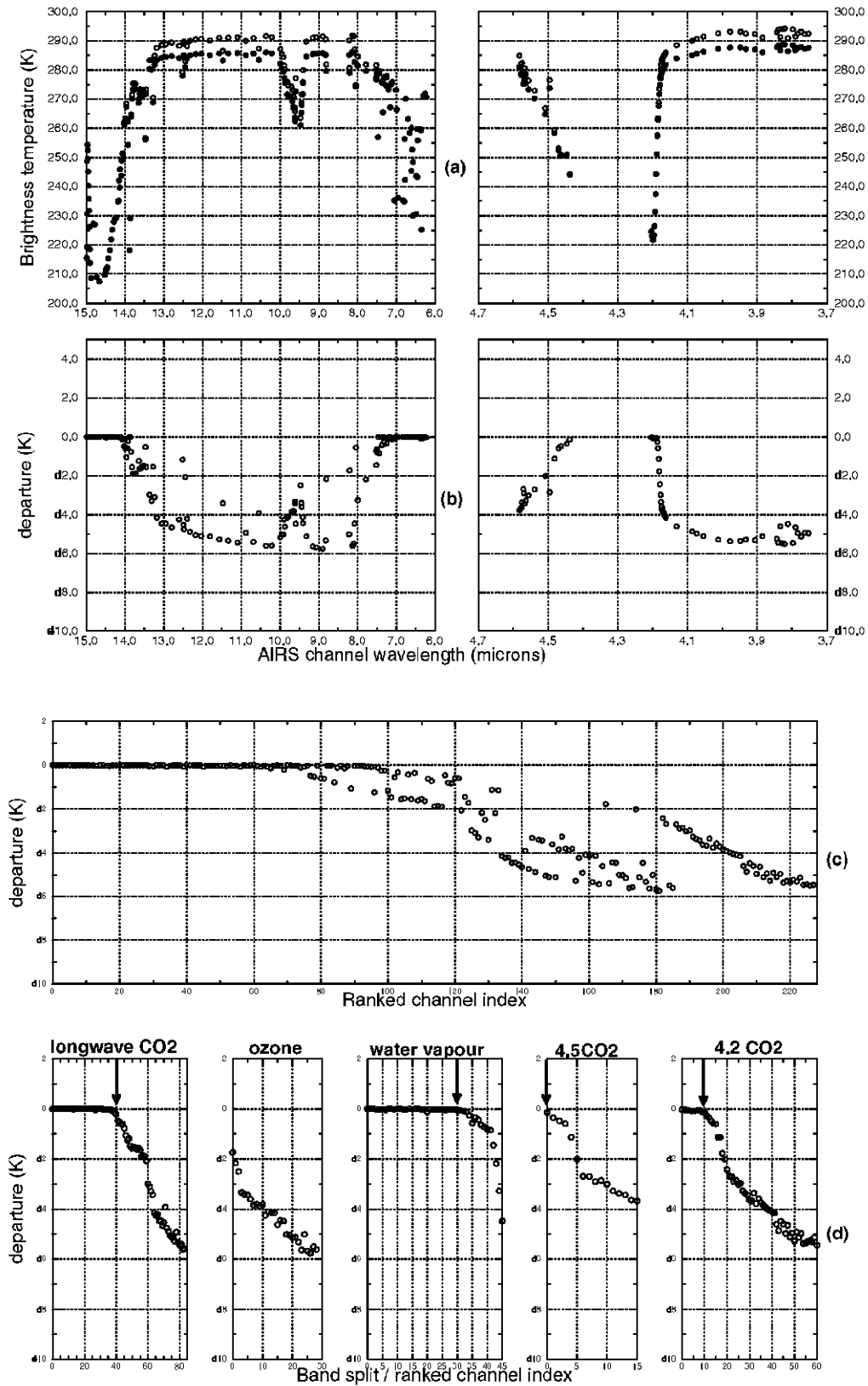


Figure 6-1: From McNally & Watts paper: (a) Simulated clear radiances (open circles) and simulated cloudy radiances (solid circles) without noise, (b) the departure vector formed by the difference of cloudy minus clear, (c) the ranked departures and (d) the ranked/band-partitioned departures.

## 6.2 RETRIEVAL OF CLOUD IN THE OEM

As an alternative to using WMC to screen cloud-affected channels, the potential to deal with cloudy scenes by include a simple cloud representation in the state vector/FM is tested. Here we adopt the simple blackbody cloud model built into RTTOV. The state vector is extended with the following parameters:

- Logarithm of the cloud fraction (so the value is forced to be positive). A priori value is  $\ln(0.01)$  (i.e. 1% fraction) with a priori error 10 (i.e. 1000% relative error on the prior 1% fraction).
- $Z^*$  cloud pressure-height in km. A priori value is 5km, with error 5km.

Sample results for a given scene are shown in Figure 6-2 over the isle of Kyushu (Japan). In the false colour infrared image (top centre) we can clearly see a homogeneous cloud cover over the southern part of Japan, extending to the west over the sea up to the shores of China.

The retrieved cloud top fraction and height reflect this picture very well. Even some of the finer details and filament structures of the northern cloud boundary region are returned by the retrieval. The retrieved cloud top height of  $\sim 10$ km is realistic for that latitude; values around 5km in cloud-free regions reflect the prior value.

Most importantly in this picture is the observation that the retrieved surface temperature (bottom centre) underneath the cloud layer also looks very credible. There are no artefacts in the surface temperature field at all at the demarcation line between the cloudy and the cloud free domains, as could reasonably be expected.

Looking at the standard deviation of the retrieved surface temperature (bottom right) it is furthermore evident that the retrieval is challenged much more in the presence of clouds. The low values over cloud free regions are from regions where the infrared channels contribute all the information in the temperature retrievals. In these regions the infrared window channels can see all the way down to the surface. The regions of high estimated standard deviation (ESD) indicate situations where most information comes from either prior (PWLR) or MW channels.

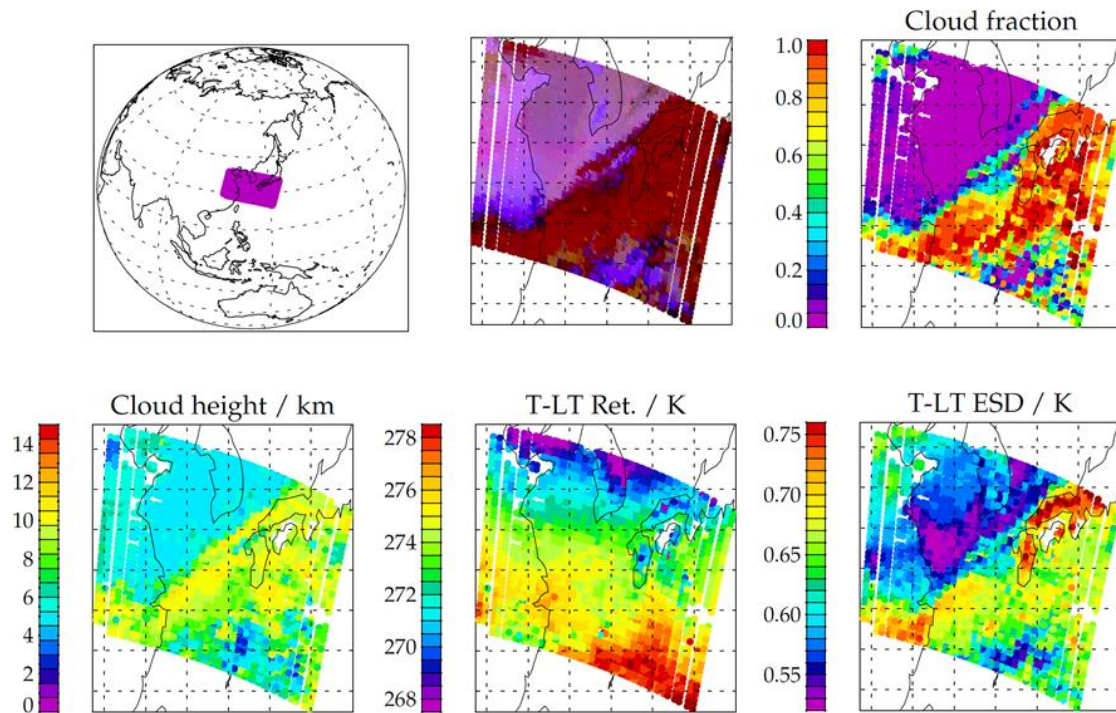


Figure 6-2: Results of adding cloud fraction and cloud top pressure to the state vector. These retrievals are nominally restricted to cloud free views with the aim to test the retrieval mechanics, but due to unavoidable errors in the cloud-flagging, some views can still be affected by clouds as this example over the Kyushu region of Japan demonstrates. The retrieved cloud fraction and cloud top height are consistent with the false colour infrared picture (top centre). The retrieved surface temperature underneath the partially cloudy pixel appears reasonable, though the ESD reflects the lack of sensitivity of the IR observations to the surface.

### 6.3 COMPARISON OF CLOUD MEASURES

The modified OEM has been applied to process all scenes with both cloud treatment options, this results in a estimates of cloud height and fraction from the OEM scheme (when cloud is retrieved), and cloud height from the WMC approach. These are compared to the operational L2 quantities here.

Figure 6-3 illustrates various cloud measures obtained during daytime from the Metop B data on 14 April 2013. Quantities are averaged over 5x5 degree latitude longitude boxes:

- RAL ZCLEAR: The WMC identified minimum cloud-sensitivity-altitude.
- Eumetsat cloud flag: the Eumetsat flag (which can have value 1-4).
- RAL cloud fraction: Retrieved cloud fraction from MWIR (also retrieving emissivity).
- Eumetsat cloud fraction: Cloud fraction from operational L2 product.
- RAL cloud-top height: Retrieved cloud-top pressure, converted to approximate altitude (scaled  $\log(\text{pressure})$ ).

- Eumetsat cloud-top height: L2 cloud-top pressure, converted to approximate altitude as above.

The bottom rows of Figure 6-3 (and following) show the cloud top height comparison again, but this time normalised by mean cloud fraction. This means that in the binning process each retrieved cloud top height is multiplied by the corresponding retrieved cloud fraction, and once the binning is completed the values are divided by the mean cloud fraction of the entire bin.

Figure 6-4 shows similar data for nighttime measurements. Figure 6-5 and Figure 6-6 show, for cloud fraction and height respectively, the scatter density plots for RAL OEM vs. Eumetsat L2 products, split by land/sea and by latitude range.

It is clear from these plots that:

The general patterns of cloudiness from the schemes correlate well.

The WMC scheme indicates a “clear” altitude, which is generally considerably (~factor 2) greater than the other measures of cloud height – it is therefore considered to provide quite a conservative cloud screening.

The Eumetsat L2 and RAL OEM cloud fraction and height correlate very well. Over land there is little bias, and what bias there is, is introduced through some outliers in the height comparison. Over sea, the Eumetsat fraction is systematically (~0.1) larger than the RAL OEM result, with a compensation effect in height.

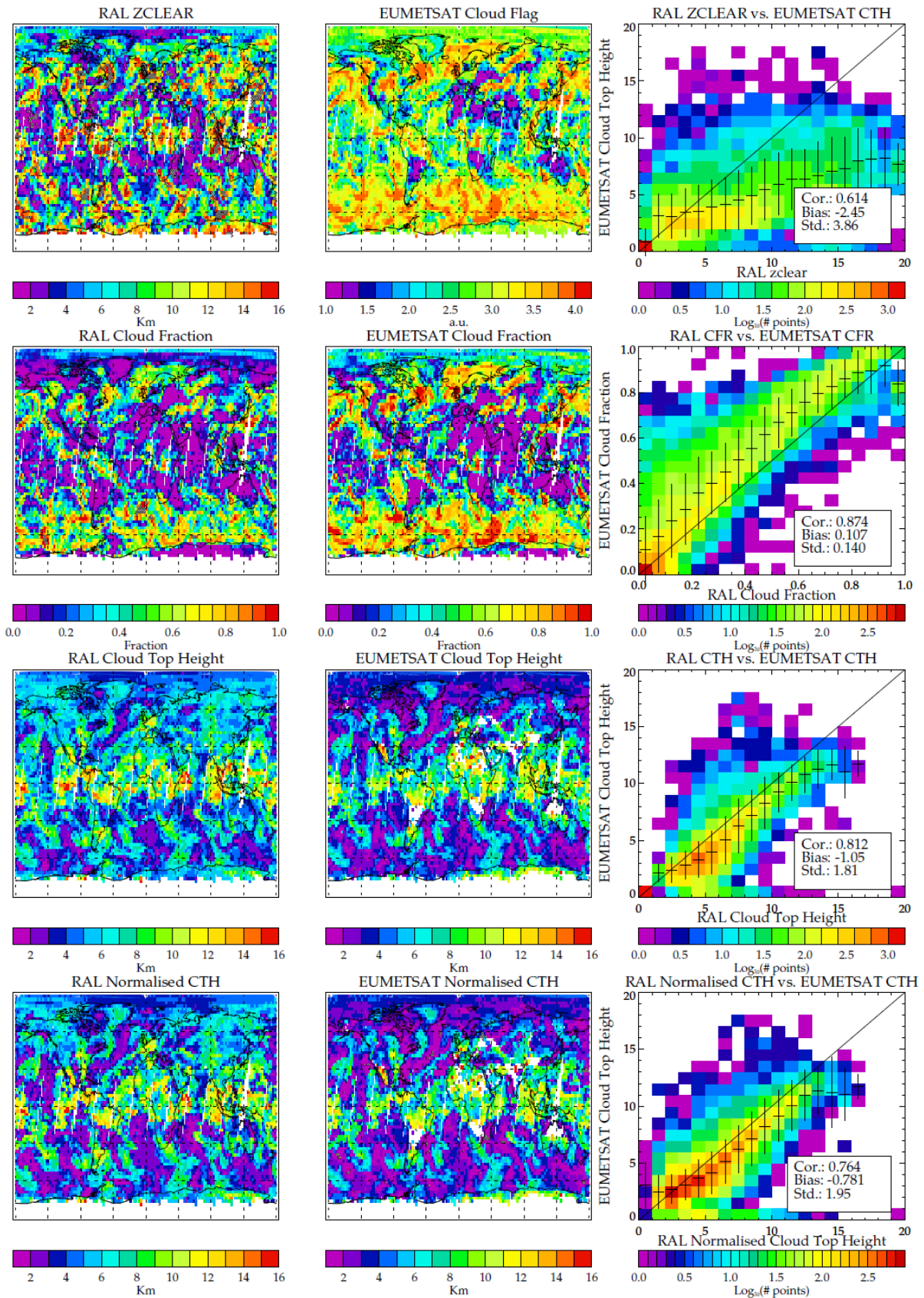


Figure 6-3: Comparison of retrieved cloud parameters for daytime orbit segments.

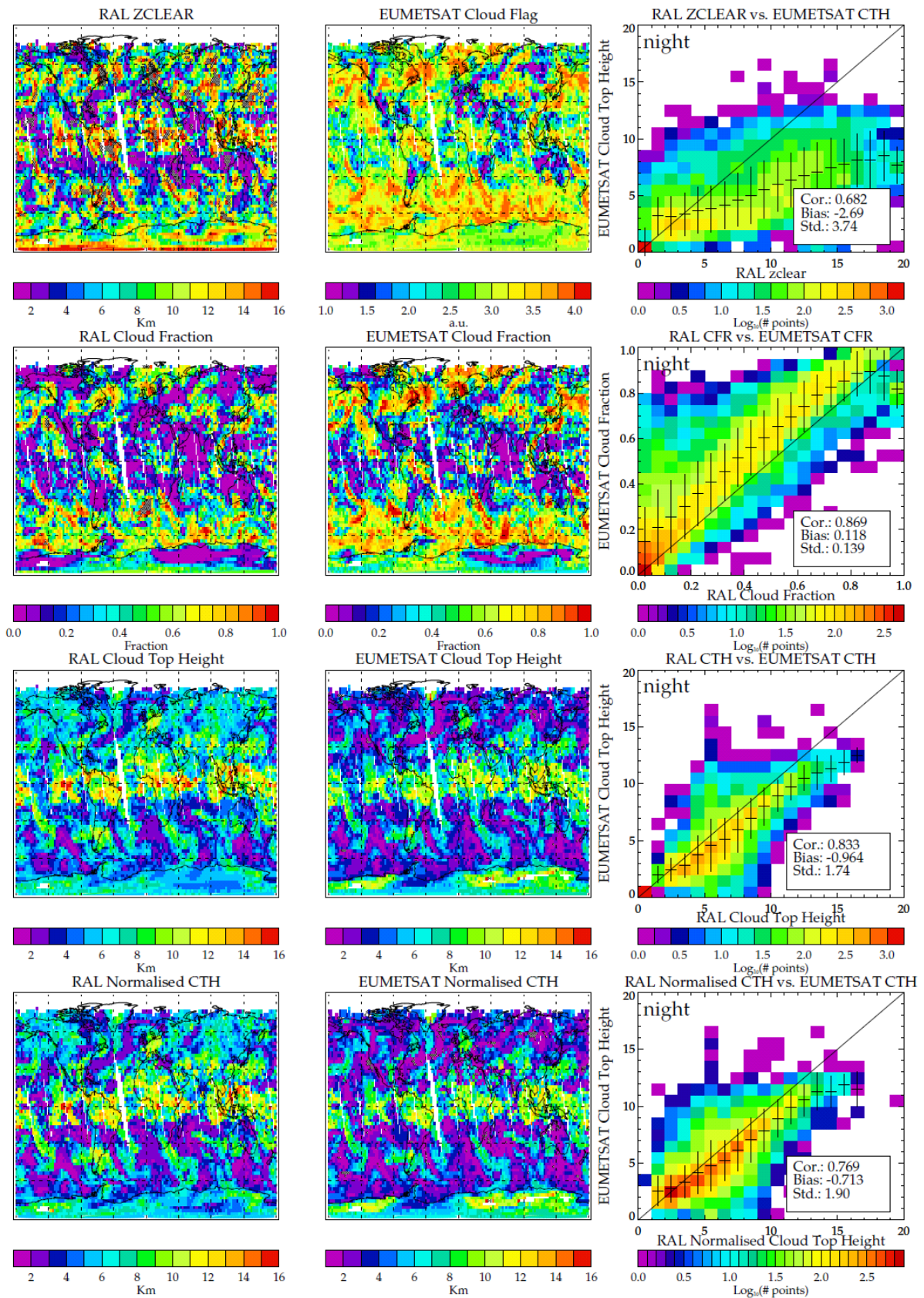


Figure 6-4: Comparison of retrieved cloud parameters for night-time orbit segments.

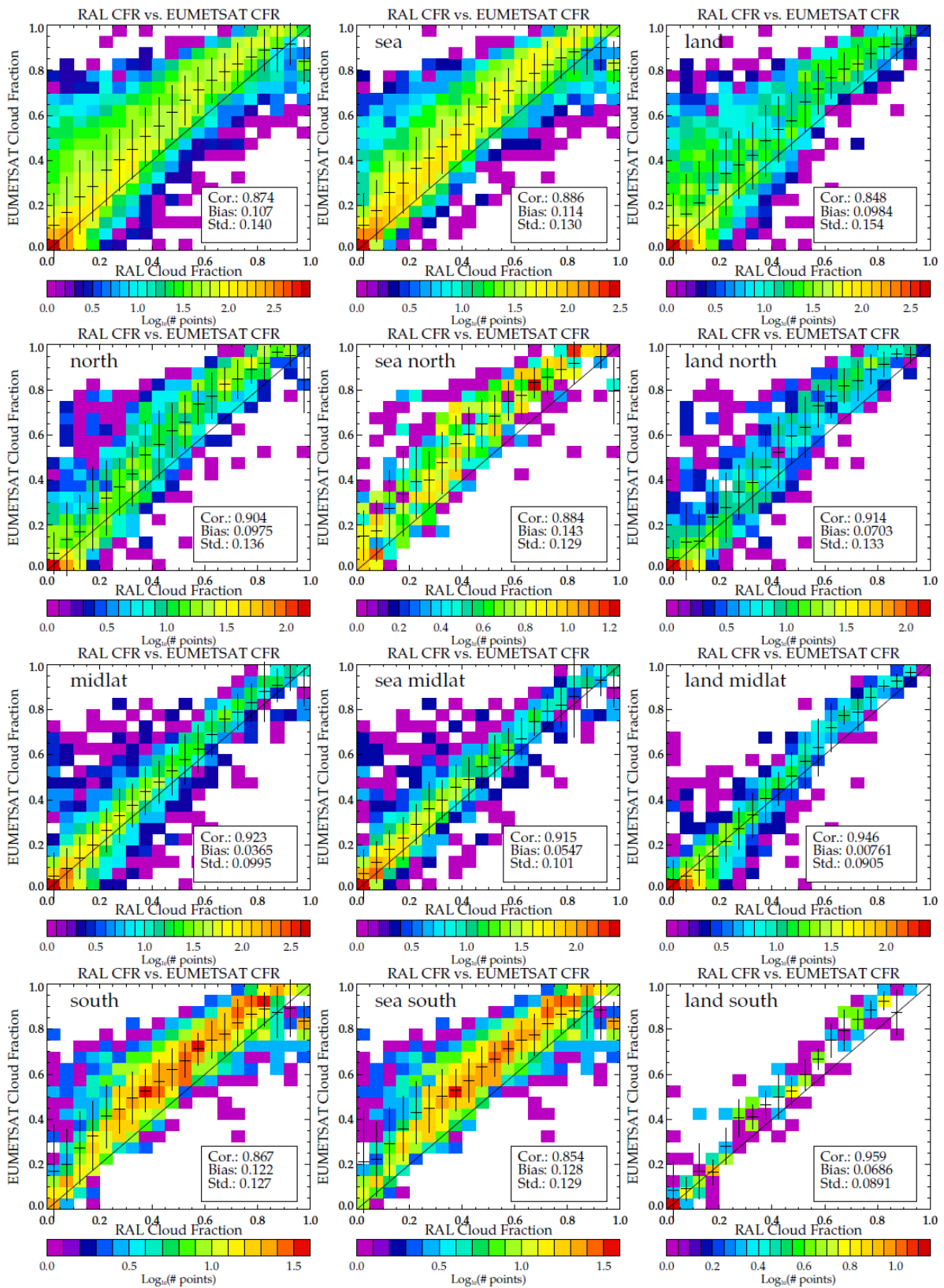


Figure 6-5: Correlations of retrieved cloud fraction by the RAL and EUMETSAT scheme, dissected in to various regions (sea/land and north/mid-latitude/south).

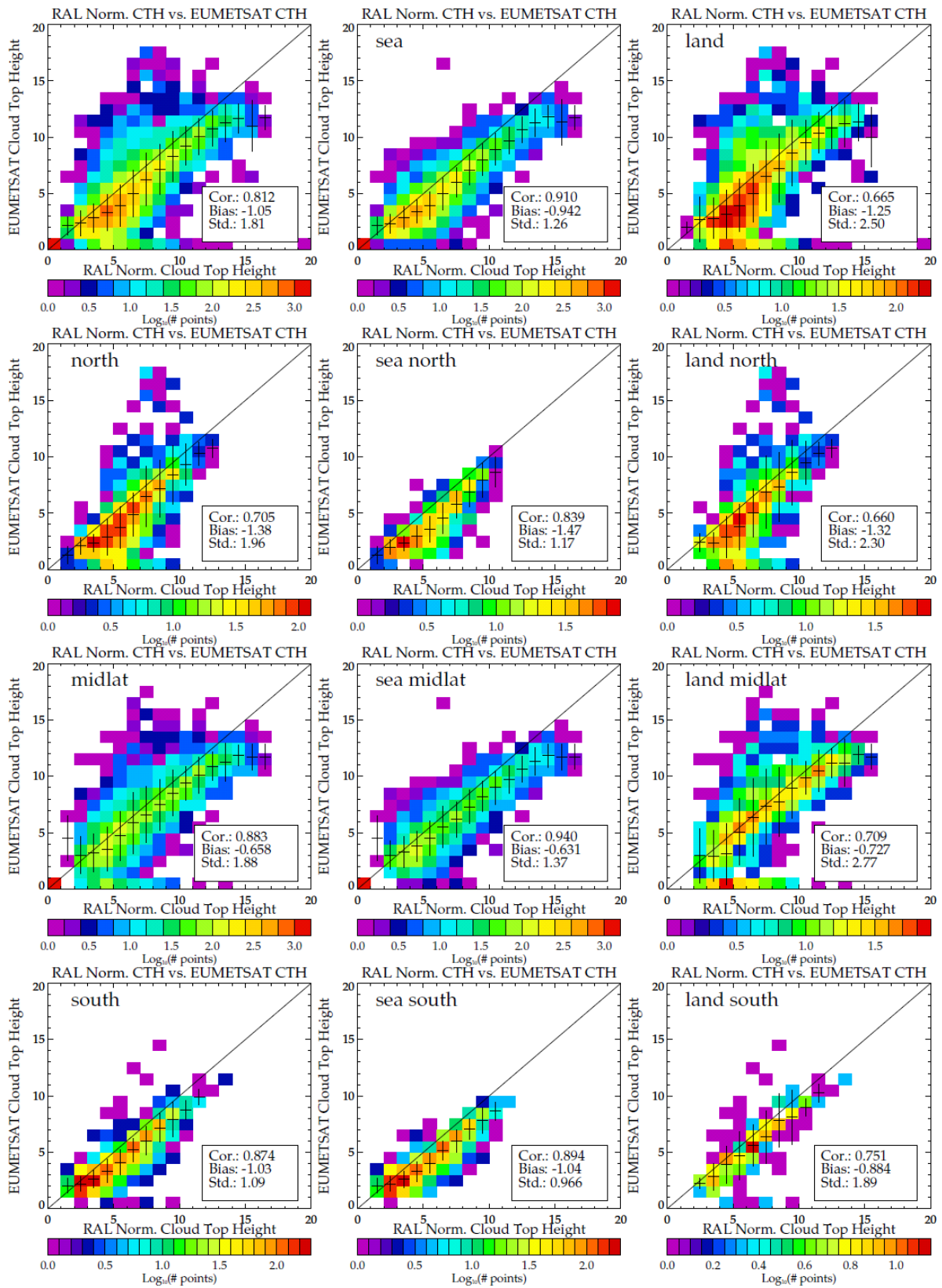


Figure 6-6: Correlations of retrieved cloud top height by the RAL and EUMETSAT scheme, dissected in to various regions (sea/land and north/mid-latitude/south).

## 6.4 OEM RETRIEVALS (MWIR) W/ CLOUDS AND STATISTICAL ANALYSIS

The impact of cloud on the OEM retrievals has been assessed by running a series of retrieval experiments. The basic retrieval configuration used includes fitting surface emissivity (20 components), with correlation between IR and MW (if MW fitted). We also include fitting of scale factors for the IASI bias correction spectral patterns. The following retrieval configurations are run on all scenes for which a PWLR result is present:

- Cloud is neglected by the FM. PWLR used as *a priori*.
- Cloud is neglected by the FM, but the WMC method is used to flag/ignore channels affected by cloud. PWLR used as *a priori*.
- Cloud is included in the state/FM. In this case tests have been run using both PWLR as *a priori* and the climatological constraint.

In all cases both IR only and MWIR retrievals have been run.

Some example retrievals are illustrated in Figure 6-7 and Figure 6-8 which, analogous to Figure 4-5, shows cross sections of retrieval- analysis along an orbit, for a number of different retrieval configurations. Many more results are presented in sections 5 and 11 of the plot annex. Note that statistics are computed only for retrievals which have a final cost smaller than 500. Where cloud is neglected it is important to note that cloudy scenes give rise to high cost, so this screening tends to remove the most cloud affected scenes from statistics for the case in which all cloud is not treated at all. One of the main benefits of both cloud treatment approaches (WMC or cloud retrieval) is the at the number of scenes with acceptable retrievals increases greatly, and this should be noted when studying the summary tables in section 11 of the annex. For retrievals which treat cloud (WMC or cloud retrieval), most scenes converge to lower cost than 500.

Tables are shown in Figure 6-9 - Figure 6-13, which show mean retrieval diagnostics and statistics for lower temperature and water vapour, for day-time land scenes only (all scene versions are included in the annex). The tables are colour coded by the value in the cell, to broadly indicate increasing values from purple-blue-green-red. In these figures scenes are summarised as a function of the cloudiness flag. Other tables and maps in the annex divided results up also by the Eumetsat cloud fraction and height. In the diagnostic summary table, the following key is used in the x-axis:

- N: Number of scenes averaged in the sample (x1000)
- JY: Measurement cost from (RAL) retrieval.
- JX: State cost from (RAL) retrieval.
- NI: Number of retrieval iterations in RAL retrieval.
- T:DOFS: Number of temperature profile degrees of freedom for signal.
- W:DOFS: Number of water vapour profile degrees of freedom for signal.
- O:DOFS: Number of ozone profile degrees of freedom for signal.
- TS:DOFS: Number of surface temperature degrees of freedom for signal.
- EM:DOFS: Number of surface emissivity degrees of freedom for signal (if retrieved).
- CFR:DOFS: Number of cloud fraction degrees of freedom for signal (if retrieved)

	RAL Space STFC Rutherford Appleton Laboratory Harwell Oxford Chilton, OX11 0QX, United Kingdom	Document:	Final Report
		Customer Ref:	ITT 13/207194
		RAL Space Ref:	SSTD1569
		2015-01-29	Page <b>102</b> of <b>120</b>

The table for temperature uses the following key:

- RET: Retrieved value
- ANA: ECMWF Analysis
- ESD: The estimated retrieval error (from the solution covariance).
- RET - ODV: Difference between retrieval and the corresponding Eumetsat result.
- RET - ANA: Difference between retrieval and analysis.
- PWLR - ANA: Difference between the PWLR and ANA.
- RET - ANAxAK: Difference between retrieval and analysis smoothed by the retrieval averaging kernel.
- PWLR - ANAxAK: Difference between the PWLR and ANAxAK.

Most mean quantities shown here are simple means over all samples, in a given layer (0-6km in the case of the example figure shown here). The standard deviation is a measure of the variation of the quantity (or difference) within the whole layer, including in the vertical. To avoid outliers these standard deviations are computed from accumulated histograms (probability distributions) of each quantity (see annex for more details).

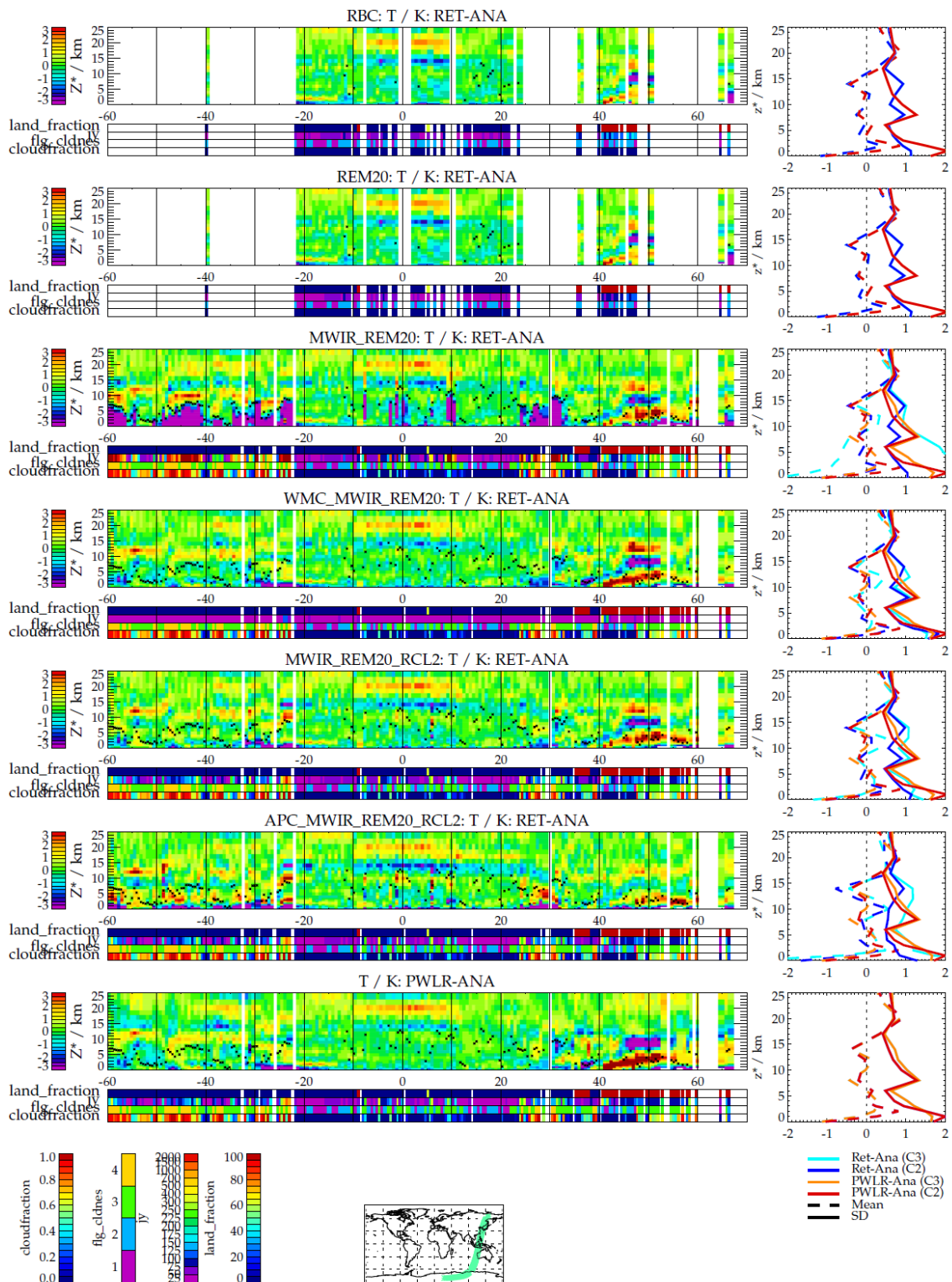
The following points are made with regard to handling of cloud in the OEM:

- When cloud is ignored, cost is similar for cloud mask 1 or 2. However it can be noted that there is an increased negative bias in Retrieval – Analysis temperature for mask 2 cases compared to mask 1 (indicating cloud contamination to be an issue even for these cases). Cost increases greatly for cloud mask 3 and again for cloud mask 4 (as does the bias). Most scenes still pass the cost threshold (500) when only IR channels are fitted. However when MW is also fit, only around half the available mask-4 cases pass this test (indicating the MW and IR cannot be reconciled without accounting for cloud).
- Ignoring cloud generally gives rise to a negative T bias and positive humidity bias in the lower troposphere, in particular at levels below the cloud, with decreasing magnitude as function of height above the cloud in both cases.
- When applying McNally Watts almost all scenes converge. Cost is generally very low because the screening is conservative; all channels are used in only a small fraction of scenes (much less than would be indicated by the cloud mask). Biases vary weakly with cloudiness, though can be notable particularly in humidity when cloud fraction is very high and the cloud is above 4km altitude. This bias is quite different depending on whether MW is used or not, indicating error in either MW or analysis for high cloud amount/height. On the other hand, DOFS for all species is seen to degrade as cloudiness increases and so the retrieval will tend towards its (PWLR) prior. For this reason the contribution of the MW is particularly evident when WMC is used. MWIR DOFS are generally larger than IR DOFS. With WMC, MWIR T+H<sub>2</sub>O DOFS are comparable to those of IR only without the cloud screening. DOFS for surface temperature are very low for WMC if the MW is not used (even then they are significantly smaller than 1). DOFS for ozone are always small for WMC.
- WMC clearly provides a very conservative (safe) cloud screening, to the extent that performance of the MWIR in cloud-free scenes (flag 1 or 2) is degraded by using the

approach. Clearly it would be desirable to optimise the use of McNally Watts, and only apply it in scenes which are considered to be sufficiently cloudy to justify it. As an initial suggestion it would seem reasonable to only apply McNally Watts when cloud mask is 3 or 4.

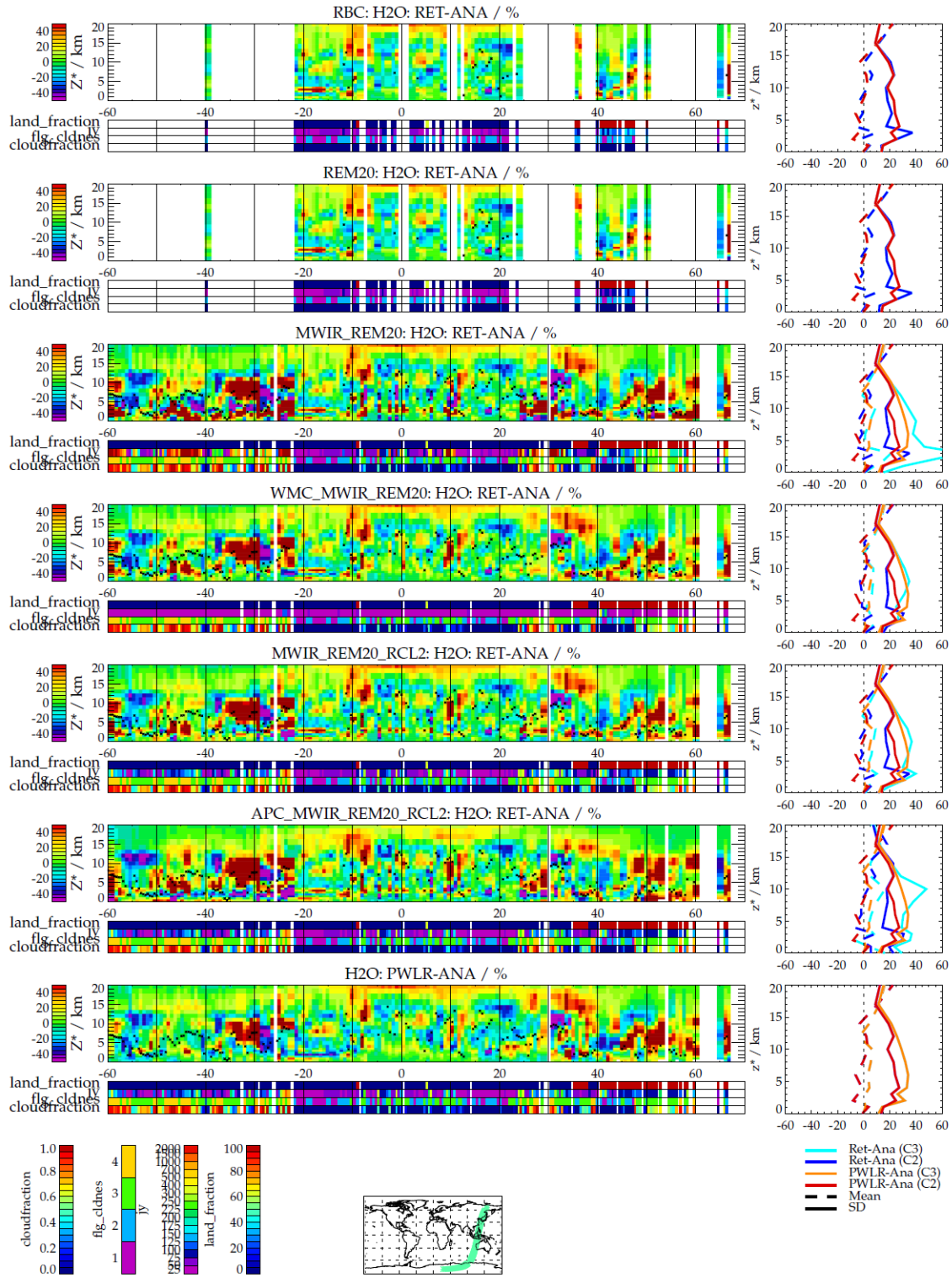
- DOFS are larger when cloud is retrieved than when McNally Watts is applied. The benefit of MW channels is clear also in this case for cloudy scenes (mask 3 + 4). This can be seen in DOFS, but also in reduced bias in retrieved T, especially when the climatological constraint is used.
- When cloud is retrieved DOFS for surface and temperature are reduced even in cloud free scenes, indicating that there is some cross-correlation between these variables (as might be expected). This is also reflected in the larger number of iterations required when cloud is retrieved. Nevertheless, the quality of the retrieved parameters in cloud-free scenes does not seem particularly adversely affected by introducing cloud parameters into the retrieval, even when the loose climatological prior is used (though this in itself does appear degrade end-end performance compared to the use of the PWLR prior).
- Generally speaking bias and standard deviations in Retrieval - Analysis are quite similar for WMC and cloud retrieval options, when PWLR is used as prior. Biases and standard deviations are somewhat worse when the climatological prior is used. In that case MW is clearly helpful in reducing both bias and standard deviation.
- For lower tropospheric temperature the retrieval of cloud seems clearly beneficial. When cloud is retrieved OEM improves on the PWLR, when that is used as prior, even for cloud mask 3 (as well as for cloud mask 1 or 2). This strongly increases (~ factor 2) the number of scenes for which the OEM result appears useful. If the climatological prior is used, the standard deviation of lower tropospheric T increases cf PWLR, however the effect is reduced if the MW is used, again clearly indicating the benefit of using the MW in the OEM.
- For LT water vapour all retrieval configurations show performance degrading as the cloud flag increases; however this is also true of PWLR, and OEM performance with WMC or cloud retrieval remains comparable to that of PWLR for cloud conditions 3 (even if this is degraded in all cases compared to cloud flag 1 or 2). It may be that this reflects errors in analysis and or co-location with analysis which are particularly significant in cloudy scenes.
- In the UT it can be seen that the OEM clearly outperforms the PWLR in standard deviation of T and H<sub>2</sub>O, at least for cloud mask 1,2 cases. Here the need to treat cloud is less marked – even when cloud is neglected it appears the OEM gives useful results above cloud. Using WMC or introducing cloud retrieval does increase the number of scenes which pass the cost function criterion however (and greatly reduced the average cost in cloudy scenes).
- Surface temperature (see Figure 6-14) seems positively biased in OEM cf. PWLR, with generally larger standard deviation. Because this is particularly true over daytime land, specifically desert regions, It is suspected that this may reflect, at least in part, errors in analysis and/or interpolation to the MetOp observation time.
- DOFS for most profile variables are increased when the climatological prior is used. Measurement cost function values are also slightly reduced (as expected). In many respects the retrievals with climatological prior perform rather well, in particular yielding agreement with analysis comparable to that of the OEM which uses PWLR as prior in cloud-free scenes. Iterations are increased, and standard deviations are greated in more cloudy scenes. There

may be a case for running the OEM with a climatological prior state and covariance, but using PWLR as first guess. This could avoid the difficulty in properly characterising the OEM sensitivity when PWLR is used as the prior profile (while also presumably reducing the number of iterations required for the OEM with climatological prior to converge).



17:49 24/01/15. IASI\_PRP\_1C\_M01\_20130417010856Z\_20130417011159Z\_N\_C\_20130417025417Z.str

Figure 6-7: Orbit cross section showing temperature differences between retrieval and analysis from different retrieval options, including those which model cloud. Cases shown are from top-bottomo: IR only (with bias correction fitted, but not emissivity or cloud); IR-only with emissivity fit; MWIR with emissivity fit, applied to all scenes; MWIR with emissivity, McNally Watts used to screen cloud; MWIR with emissivity and cloud parameters fit; same but with climatological prior instead of PWLR; PWLR compared to analysis.



7:49 24/01/15.

IASI\_PRP\_1C\_M01\_20130417010856Z\_20130417011159Z\_N\_C\_20130417025417Z.str

Figure 6-8: Orbit cross section showing water vapour differences between retrieval and analysis from different retrieval options, including those which model cloud. Cases shown are from top-bottom: IR only (with bias correction fitted, but not emissivity or cloud); IR-only with emissivity fit; MWIR with emissivity fit, applied to all scenes; MWIR with emissivity, McNally Watts used to screen cloud; MWIR with emissivity and cloud parameters fit; same but with climatological prior instead of PWLR; PWLR compared to analysis.

		Mean									
standard		186	133	13	3.2	6.8	4.4	1.9	0.98		
	cm:1	99	71	18	3	6.6	4.3	1.9	0.97	12	
	cm:2	139	83	20	3.1	6.7	4.4	1.8	0.97	12	
	cm:3	156	169	61	4.9	6.7	4.2	1.4	0.96	9.3	
	cm:4	62	213	211	11	6.8	4.3	0.85	0.91	5.5	
MWIR2	cm:1	97	96	20	3.4	9	4.9	1.9	0.98	14	
MWIR2	cm:2	138	109	21	3.5	9	5	1.8	0.97	13	
MWIR2	cm:3	135	195	33	4.4	9	4.8	1.4	0.97	11	
MWIR2	cm:4	34	252	52	6	9.1	4.4	1.1	0.95	9.2	
wmc	cm:1	100	19	4.2	2.1	5.2	2.6	0.12	0.22	0.72	
wmc	cm:2	139	17	3.9	2.1	4.9	2.3	0.12	0.17	0.69	
wmc	cm:3	185	5.4	2	2	3.4	0.65	0.012	0.011	0.031	
wmc	cm:4	85	3.3	1.6	2	3.1	0.32	0.0024	0.00041	0.00028	
wmc MWIR2	cm:1	100	32	7.3	3.1	7.9	3.8	0.13	0.63	3.1	
wmc MWIR2	cm:2	139	30	7.5	3.1	7.8	3.8	0.13	0.6	3	
wmc MWIR2	cm:3	185	17	6.8	3.2	7.2	3.1	0.014	0.53	2.4	
wmc MWIR2	cm:4	85	19	16	4.2	7.1	3	0.0033	0.5	2.2	
Cld2	cm:1	99	69	17	4.4	6.4	4.3	1.9	0.87	12	0.74
Cld2	cm:2	139	72	17	5.3	6.3	4.3	1.8	0.83	12	0.84
Cld2	cm:3	182	120	26	8.6	5.7	3.7	1.3	0.78	8.8	0.98
Cld2	cm:4	84	111	14	9.5	4.9	2	0.63	0.4	4.1	0.99
MWIR2 Cld2	cm:1	97	93	19	4.6	8.8	4.9	1.9	0.92	14	0.75
MWIR2 Cld2	cm:2	139	95	19	5.5	8.8	5	1.8	0.89	13	0.87
MWIR2 Cld2	cm:3	179	145	27	8.5	8.5	4.6	1.3	0.86	10	0.99
MWIR2 Cld2	cm:4	83	138	26	10	7.9	3.8	0.63	0.65	5.9	1
AP=Cli Cld2	cm:1	100	64	15	5.9	10	5.7	3.4	0.96	12	0.74
AP=Cli Cld2	cm:2	139	67	16	6.7	10	5.8	3.4	0.95	11	0.82
AP=Cli Cld2	cm:3	183	104	26	10	9.7	5.2	2.8	0.95	9.3	0.94
AP=Cli Cld2	cm:4	85	90	18	11	8.5	3.6	1.8	0.73	5.3	0.96
AP=Cli MWIR2 Cld2	cm:1	98	88	17	7.5	11	5.9	3.4	0.98	13	0.73
AP=Cli MWIR2 Cld2	cm:2	139	90	18	8.1	11	6	3.4	0.98	13	0.87
AP=Cli MWIR2 Cld2	cm:3	181	135	26	9.7	11	5.7	2.8	0.97	10	0.99
AP=Cli MWIR2 Cld2	cm:4	84	128	22	11	10	4.7	1.9	0.88	6	1
		:Z	:Y	:X	:NI	:T:DOFS	:W:DOFS	:O:DOFS	:TS:DOFS	:EM:DOFS	:CFR:DOFS

Figure 6-9: Summary table showing basic retrieval diagnostics for different cloud-related options. Top row in table shows results for the standard IR only scheme (in cloud-free scenes). Then rows show, divided by cloudiness flag value ("cm:x", where x=1-4), results from different retrieval options (all of which include fitting of emissivity and bias correction parameters), as follows: IR only scheme; MWIR scheme, IR only scheme with McNally Watts, MWIR scheme with McNally Watts; IR only with cloud retrieval; MWIR with cloud retrieval; IR only with cloud retrieval, starting from climatological prior; MWIR with cloud retrieval, starting from Climatological prior. Column headings are defined in the text.

	Mean								Std.deviation (total)			
standard	186	272	272	0.6	-0.22	-0.03	-0.17	-0.059	0.98	1.2	0.75	0.73
cm:1	99	272	272	0.6	-0.18	-0.076	-0.13	-0.091	0.97	1.3	0.69	0.76
cm:2	139	272	273	0.6	-0.36	0.0081	-0.29	-0.025	1.1	1.2	0.94	0.74
cm:3	156	269	271	0.61	-1.2	0.1	-1.3	0.023	2.2	1.3	2.1	0.76
cm:4	62	266	270	0.58	-1.7	-0.15	-1.7	-0.15	4	1.4	3.7	0.81
MWIR2 cm:1	97	272	272	0.58	-0.23	-0.075	-0.22	-0.094	0.95	1.3	0.68	0.81
MWIR2 cm:2	138	272	272	0.58	-0.3	0.007	-0.25	-0.026	1.1	1.2	0.86	0.8
MWIR2 cm:3	135	271	271	0.58	-0.4	0.084	-0.39	0.02	1.6	1.3	1.4	0.85
MWIR2 cm:4	34	267	268	0.56	-0.36	-0.24	-0.3	-0.23	2	1.4	1.9	0.88
wmc cm:1	100	272	272	0.71	-0.031	-0.062	0.0017	-0.014	1.2	1.3	0.39	0.45
wmc cm:2	139	272	273	0.73	0.0004	0.02	-0.0015	-0.0056	1.1	1.2	0.35	0.38
wmc cm:3	185	272	272	0.79	0.13	0.14	0.011	0.0085	1.2	1.3	0.24	0.26
wmc cm:4	85	271	271	0.8	-0.019	-0.045	0.015	0.0027	1.4	1.4	0.26	0.29
wmc MWIR2 cm:1	100	272	272	0.67	-0.046	-0.061	-0.055	-0.077	1.1	1.3	0.48	0.63
wmc MWIR2 cm:2	139	272	273	0.68	-0.0071	0.021	-0.033	-0.033	1.1	1.2	0.5	0.62
wmc MWIR2 cm:3	185	272	272	0.72	0.059	0.14	-0.047	0.027	1.1	1.3	0.51	0.61
wmc MWIR2 cm:4	85	271	271	0.72	-0.13	-0.048	-0.16	-0.083	1.4	1.4	0.62	0.65
Cld2 cm:1	99	272	272	0.63	-0.032	-0.068	0.031	-0.082	0.99	1.3	0.59	0.68
Cld2 cm:2	139	272	273	0.64	0.074	0.017	0.073	-0.026	1	1.2	0.63	0.63
Cld2 cm:3	182	272	272	0.69	0.24	0.13	0.14	0.0087	1.4	1.3	0.91	0.51
Cld2 cm:4	84	271	271	0.76	0.13	-0.056	0.039	-0.031	1.5	1.4	0.65	0.38
MWIR2 Cld2 cm:1	97	272	272	0.59	-0.16	-0.066	-0.15	-0.088	0.95	1.3	0.62	0.78
MWIR2 Cld2 cm:2	139	272	273	0.6	-0.1	0.017	-0.091	-0.023	1	1.2	0.68	0.77
MWIR2 Cld2 cm:3	179	272	272	0.63	0.1	0.13	0.041	0.05	1.2	1.3	0.9	0.75
MWIR2 Cld2 cm:4	83	271	271	0.69	-0.002	-0.061	-0.038	-0.075	1.5	1.4	0.84	0.72
AP=Cli Cld2 cm:1	100	272	272	1.2	0.031	-0.065	0.04	-0.033	1.2	1.3	0.98	1.1
AP=Cli Cld2 cm:2	139	272	273	1.2	0.12	0.018	0.11	0.032	1.4	1.2	1.2	1.1
AP=Cli Cld2 cm:3	183	271	272	1.5	0.19	0.13	0.19	0.15	3.3	1.3	3	1.2
AP=Cli Cld2 cm:4	85	269	271	2.6	0.28	-0.046	0.12	-0.25	5.8	1.4	5.4	1.5
AP=Cli MWIR2 Cld2 cm:1	98	272	272	1	-0.24	-0.066	-0.22	-0.041	1.2	1.3	0.95	1.1
AP=Cli MWIR2 Cld2 cm:2	139	272	273	1	-0.19	0.017	-0.18	0.03	1.3	1.2	1.1	1.1
AP=Cli MWIR2 Cld2 cm:3	181	271	272	1.2	0.016	0.13	0.03	0.18	2.1	1.3	1.9	1.2
AP=Cli MWIR2 Cld2 cm:4	84	271	271	1.5	0.077	-0.053	0.12	0.032	2.2	1.4	2	1.4
	N	T:RET	T:ANA	T:ESD	T:RET - ANA	T:PWLR - ANA	T:RET - ANAxxAK	T:PWLR - ANAxxAK	T:RET - ANA	T:PWLR - ANA	T:RET - ANAxxAK	T:PWLR - ANAxxAK

Temperature / K 0-6km; day land; All days; BC; Emis:20n; asc

23:05 27/01/15.

Figure 6-10: Summary table for lower tropospheric temperature, comparing different options to deal with cloud. Top row in table shows results for the standard IR only scheme (in cloud-free scenes). Then rows show, divided by cloudiness flag value ("cm:x", where x=1-4), results from different retrieval options (all of which include fitting of emissivity and bias correction parameters), as follows: IR only scheme; MWIR scheme, IR only scheme with McNally Watts, MWIR scheme with McNally Watts; IR only with cloud retrieval; MWIR with cloud retrieval; IR only with cloud retrieval, starting from climatological prior; MWIR with cloud retrieval, starting from Climatological prior. Column headings are defined in the text.

	Mean								Std.deviation (total)			
standard	186	231	231	0.7	0.095	0.081	0.14	0.026	0.76	1	0.39	0.56
cm:1	99	231	231	0.71	0.087	0.036	0.12	-0.0033	0.81	1.2	0.34	0.59
cm:2	139	232	232	0.7	0.047	0.12	0.073	0.062	0.79	1	0.39	0.56
cm:3	156	231	231	0.7	-0.05	0.11	0.03	0.069	1.1	1.2	0.6	0.62
cm:4	62	231	231	0.69	0.09	0.084	0.11	0.03	1.1	1.3	0.51	0.66
MWIR2 cm:1	97	231	231	0.67	0.06	0.036	0.086	0.014	0.79	1.2	0.4	0.68
MWIR2 cm:2	138	232	232	0.67	0.056	0.12	0.069	0.082	0.77	1	0.44	0.65
MWIR2 cm:3	135	232	231	0.67	0.08	0.096	0.093	0.07	0.98	1.2	0.61	0.74
MWIR2 cm:4	34	231	231	0.67	0.28	-0.033	0.25	-0.036	1.1	1.3	0.7	0.77
wmc cm:1	100	231	231	0.75	0.095	0.035	0.046	-0.045	0.88	1.2	0.29	0.46
wmc cm:2	139	232	232	0.76	0.11	0.12	-0.016	-0.042	0.84	1	0.27	0.37
wmc cm:3	185	232	232	0.84	0.13	0.16	-0.067	-0.063	1	1.1	0.16	0.17
wmc cm:4	85	232	232	0.86	0.19	0.18	-0.054	-0.055	1.2	1.3	0.14	0.18
wmc MWIR2 cm:1	100	231	231	0.7	0.076	0.035	0.087	0.012	0.83	1.2	0.39	0.64
wmc MWIR2 cm:2	139	232	232	0.71	0.086	0.12	0.068	0.077	0.8	1	0.41	0.61
wmc MWIR2 cm:3	185	232	232	0.75	0.094	0.16	0.051	-0.12	0.95	1.1	0.46	0.64
wmc MWIR2 cm:4	85	232	232	0.75	0.16	0.17	0.092	0.12	1.1	1.3	0.51	0.72
Cld2 cm:1	99	231	231	0.71	0.098	0.036	0.11	-0.0056	0.82	1.2	0.34	0.56
Cld2 cm:2	139	232	232	0.71	0.13	0.12	0.087	0.048	0.76	1	0.36	0.52
Cld2 cm:3	182	232	232	0.73	0.32	0.15	0.18	0.04	1	1.1	0.54	0.51
Cld2 cm:4	84	232	232	0.75	0.27	0.18	0.1	-0.01	1.1	1.3	0.47	0.52
MWIR2 Cld2 cm:1	97	231	231	0.67	0.049	0.038	0.068	0.016	0.81	1.2	0.41	0.67
MWIR2 Cld2 cm:2	139	232	232	0.67	0.084	0.12	0.067	0.083	0.75	1	0.42	0.64
MWIR2 Cld2 cm:3	179	232	232	0.68	0.18	0.15	0.13	0.11	0.92	1.1	0.55	0.71
MWIR2 Cld2 cm:4	83	232	232	0.68	0.17	0.18	0.13	0.12	1	1.3	0.56	0.8
AP=Cli Cld2 cm:1	100	231	231	0.95	0.14	0.033	0.13	0.0024	0.82	1.2	0.55	0.92
AP=Cli Cld2 cm:2	139	232	232	0.96	0.11	0.12	0.11	0.11	0.83	1	0.59	0.87
AP=Cli Cld2 cm:3	183	232	232	1	0.43	0.15	0.32	0.14	1.4	1.1	1.3	0.97
AP=Cli Cld2 cm:4	85	233	232	1.3	0.53	0.17	0.4	0.17	2.5	1.3	2.4	1.1
AP=Cli MWIR2 Cld2 cm:1	98	231	231	0.88	0.082	0.035	0.099	0.019	0.85	1.2	0.65	0.94
AP=Cli MWIR2 Cld2 cm:2	139	232	232	0.88	0.087	0.12	0.091	0.11	0.84	1	0.64	0.88
AP=Cli MWIR2 Cld2 cm:3	181	232	232	0.9	0.19	0.15	0.17	0.13	1	1.1	0.88	0.97
AP=Cli MWIR2 Cld2 cm:4	84	232	232	0.92	0.16	0.18	0.17	0.17	1.1	1.3	0.92	1.1

23.05.27/01/15.

Figure 6-11: Summary table for upper tropospheric temperature, comparing different options to deal with cloud. Top row in table shows results for the standard IR only scheme (in cloud-free scenes). Then rows show, divided by cloudiness flag value ("cm:x", where x=1-4), results from different retrieval options (all of which include fitting of emissivity and bias correction parameters), as follows: IR only scheme; MWIR scheme, IR only scheme with McNally Watts, MWIR scheme with McNally Watts; IR only with cloud retrieval; MWIR with cloud retrieval; IR only with cloud retrieval, starting from climatological prior; MWIR with cloud retrieval, starting from Climatological prior. Column headings are defined in the text.

	Mean								Std.deviation (total) <sup>§</sup>			
	186	3829	3684	12	0.45	-2.6	1.5	-1.1	16	17	12	11
standard	99	3317	3402	11	-0.49	-3.3	0.57	-1.6	14	17	9.4	11
cm:1	139	3832	3797	13	-0.0027	-2.5	0.61	-1	18	20	13	13
cm:2	156	4965	4288	17	2.8	-1.4	1.7	-0.73	32	22	27	13
cm:3	62	8037	4436	22	3.5	-1.7	3.2	-0.63	55	20	52	9.5
cm:4	97	3366	3405	11	-0.17	-3.3	0.86	-1.6	13	17	9.6	12
MWIR2 cm:1	138	3908	3797	13	0.33	-2.4	1.1	-1.1	18	20	13	14
MWIR2 cm:2	135	4782	4270	16	1.8	-1.4	1.9	-0.57	27	22	22	14
MWIR2 cm:3	34	5371	4012	17	0.7	-1.9	1.4	-0.58	19	19	14	10
MWIR2 cm:4	100	3289	3400	14	-1.2	-3.3	0.22	-0.63	15	17	5.1	5
wmc cm:1	139	3743	3795	17	-1	-2.3	-0.038	-0.42	18	20	4.1	4
wmc cm:2	185	4209	4357	22	-1.5	-1.8	-0.32	-0.34	23	24	1.6	1.6
wmc cm:3	85	4476	4659	25	-1.1	-1.6	-0.2	-0.33	26	27	1.6	1.6
wmc cm:4	100	3331	3400	13	-0.46	-3.3	0.73	-1.1	14	17	8.2	9.3
wmc MWIR2 cm:1	139	3798	3795	15	-0.014	-2.3	0.71	-0.83	18	20	10	11
wmc MWIR2 cm:2	185	4407	4357	19	0.84	-1.8	0.74	-0.77	23	24	15	13
wmc MWIR2 cm:3	85	5376	4658	24	3.3	-1.6	2.2	-0.26	35	27	28	13
wmc MWIR2 cm:4	99	3283	3402	11	-0.56	-3.3	0.53	-1.5	14	17	9.2	11
Cld2 cm:1	139	3755	3796	13	-0.56	-2.4	0.34	-0.95	18	20	12	12
Cld2 cm:2	182	4403	4347	16	-1	-1.9	-0.66	-0.57	27	24	19	12
Cld2 cm:3	84	5075	4661	24	0.28	-1.6	0.61	-0.0024	29	26	12	5.6
Cld2 cm:4	97	3334	3404	11	-0.15	-3.2	0.85	-1.6	13	17	9.6	12
MWIR2 Cld2 cm:1	139	3836	3797	13	0.3	-2.3	1.1	-1.1	17	20	13	14
MWIR2 Cld2 cm:2	179	4521	4341	16	1.6	-1.8	1.6	-0.85	27	23	21	15
MWIR2 Cld2 cm:3	83	5383	4660	22	4.3	-1.7	3.4	-0.42	36	26	30	14
MWIR2 Cld2 cm:4	100	3276	3411	20	-0.73	-3.2	0.25	-2.7	16	17	13	16
AP=Cli Cld2 cm:1	139	3806	3815	23	-0.51	-2.3	0.23	-2	21	20	18	19
AP=Cli Cld2 cm:2	183	4144	4367	26	-2.9	-1.8	-1.8	-0.67	40	24	37	22
AP=Cli Cld2 cm:3	85	4657	4676	43	-2	-1.5	2.5	3.7	65	26	58	27
AP=Cli Cld2 cm:4	98	3358	3412	19	-0.26	-3.2	0.62	-2.7	15	17	13	16
AP=Cli MWIR2 Cld2 cm:1	139	3910	3817	22	0.39	-2.3	1	-2.2	20	20	18	19
AP=Cli MWIR2 Cld2 cm:2	181	4505	4365	26	1.7	-1.8	2.4	-1.3	39	24	37	23
AP=Cli MWIR2 Cld2 cm:3	84	5166	4678	39	7	-1.6	8.4	-1.1	55	26	54	27
AP=Cli MWIR2 Cld2 cm:4												

N  
 W:RET  
 W:ANA  
 W:BSD/%  
 W:RET - ANA/%  
 W:PWILR - ANA/%  
 W:RET - ANAxAK/%  
 W:PWILR - ANAxAK/%  
 W:RET - ANAxAK/%  
 W:PWILR - ANAxAK/%  
 W:RET - ANA/%  
 W:PWILR - ANA/%  
 W:RET - ANAxAK/%  
 W:PWILR - ANAxAK/%

Water vapour / ppm 0-6km; day land; All days; BC; Emis:20n; asc

23.06.27/01/15.

Figure 6-12: Summary table for lower tropospheric water vapour, comparing different options to deal with cloud. Top row in table shows results for the standard IR only scheme (in cloud-free scenes). Then rows show, divided by cloudiness flag value ("cm:x", where x=1-4), results from different retrieval options (all of which include fitting of emissivity and bias correction parameters), as follows: IR only scheme; MWIR scheme, IR only scheme with McNally Watts, MWIR scheme with McNally Watts; IR only with cloud retrieval; MWIR with cloud retrieval; IR only with cloud retrieval, starting from climatological prior; MWIR with cloud retrieval, starting from Climatological prior. Column headings are defined in the text.

	Mean								Std.deviation (total)				
standard	186	156	162	16	-0.79	-1.8	0.23	-0.62	12	14	6.2	7	
cm:1	99	140	149	14	-1.1	-1.8	-0.14	-0.47	11	13	5.2	6.6	
cm:2	139	166	173	17	-1.2	-1.9	-0.18	-0.58	13	16	7.2	8.2	
cm:3	156	223	237	22	-0.66	-0.82	-0.12	-0.44	19	21	10	11	
cm:4	62	391	272	33	0.84	0.41	0.25	-0.16	14	16	7.4	7.1	
MWIR2 cm:1	97	144	149	14	-0.62	-1.7	0.21	-0.45	10	13	6.1	8.2	
MWIR2 cm:2	138	172	173	16	-0.78	-1.9	0.14	-0.59	13	16	8.2	10	
MWIR2 cm:3	135	215	228	20	-0.49	-0.87	0.11	-0.31	18	21	13	14	
MWIR2 cm:4	34	184	188	17	1.2	0.22	0.78	-0.025	11	14	7	8.8	
wmc cm:1	100	139	149	16	-0.85	-1.8	0.18	-0.33	11	14	3.9	4.9	
wmc cm:2	139	167	173	20	-1.1	-1.9	0.077	-0.29	14	16	3.5	4.4	
wmc cm:3	185	244	250	35	-1	-1.2	-0.045	-0.033	23	24	1.7	1.7	
wmc cm:4	85	306	316	46	-0.26	-0.56	-0.054	0.0085	22	23	1.6	1.7	
wmc MWIR2 cm:1	100	145	149	14	-0.6	-1.8	0.43	-0.38	11	14	5.9	7.9	
wmc MWIR2 cm:2	139	171	173	17	-0.56	-1.9	0.47	-0.45	13	16	7.5	9.7	
wmc MWIR2 cm:3	185	262	250	28	0.12	-1.2	0.72	-0.31	21	24	13	15	
wmc MWIR2 cm:4	85	449	317	43	2.3	-0.51	1.4	-0.45	21	23	15	14	
Cld2 cm:1	99	140	149	14	-0.96	-1.8	-0.0024	-0.51	11	13	5.3	6.6	
Cld2 cm:2	139	168	173	17	-0.99	-1.9	0.06	-0.62	14	16	7.2	8.2	
Cld2 cm:3	182	227	250	25	-0.67	-1.2	0.23	-0.55	22	24	12	11	
Cld2 cm:4	84	302	318	39	0.081	-0.49	0.25	-0.19	21	23	6.8	5.3	
MWIR2 Cld2 cm:1	97	145	149	14	-0.61	-1.8	0.24	-0.47	10	13	6.2	8.2	
MWIR2 Cld2 cm:2	139	174	173	16	-0.59	-1.9	0.24	-0.63	13	16	8.3	10	
MWIR2 Cld2 cm:3	179	252	248	23	0.34	-1.1	0.61	-0.55	20	23	14	16	
MWIR2 Cld2 cm:4	83	434	317	39	2.5	-0.38	1.5	-0.48	20	22	15	15	
AP=Cli Cld2 cm:1	100	141	150	16	-0.94	-1.8	-0.31	-1.2	12	13	8	11	
AP=Cli Cld2 cm:2	139	170	173	19	-0.55	-1.9	0.0042	-1.5	15	16	11	13	
AP=Cli Cld2 cm:3	183	239	253	29	1.4	-1.2	1.3	-1.6	24	24	20	19	
AP=Cli Cld2 cm:4	85	274	316	51	1.7	-0.5	2.5	0.94	32	23	20	21	
AP=Cli MWIR2 Cld2 cm:1	98	145	150	15	-0.61	-1.8	0.0063	-1.1	11	13	8.1	11	
AP=Cli MWIR2 Cld2 cm:2	139	175	174	17	-0.55	-1.9	0.017	-1.4	14	16	11	13	
AP=Cli MWIR2 Cld2 cm:3	181	266	253	27	1.3	-1.1	0.98	-1.6	22	24	18	20	
AP=Cli MWIR2 Cld2 cm:4	84	507	316	51	4.5	-0.43	3.2	-1.5	24	22	22	19	
	:N	W:RET	W:ANA	W:ESD/%	W:RET - ANA/%	W:PWLR - ANA/%	W:RET - ANAXAK/%	W:PWLR - ANAXAK/%	W:RET - ANA/%	W:PWLR - ANA/%	W:RET - ANAXAK/%	W:PWLR - ANAXAK/%	

Water vapour / ppm 6-12km; day land; All days; BC; Emis:20ng<sup>asc</sup>

23/06/27/01/15.

Figure 6-13: Summary table for upper tropospheric water vapour, comparing different options to deal with cloud. Top row in table shows results for the standard IR only scheme (in cloud-free scenes). Then rows show, divided by cloudiness flag value ("cm:x", where x=1-4), results from different retrieval options (all of which include fitting of emissivity and bias correction parameters), as follows: IR only scheme; MWIR scheme, IR only scheme with McNally Watts, MWIR scheme with McNally Watts; IR only with cloud retrieval; MWIR with cloud retrieval; IR only with cloud retrieval, starting from climatological prior; MWIR with cloud retrieval, starting from Climatological prior. Column headings are defined in the text.

	Mean								Std.deviation (total)			
standard	54	294	292	0.39	2.9	0.12	2.9	0.13	3.5	2.9	3.5	2.8
cm:1	31	297	294	0.49	3.5	-0.35	3.5	-0.32	3.8	3	3.7	3
cm:2	38	293	292	0.52	1.7	-0.29	1.7	-0.29	4	3	4	2.9
cm:3	41	281	289	0.58	-6.3	-0.37	-6.4	-0.39	5	2.9	4.9	2.8
cm:4	13	262	285	0.73	-9.9	-1	-9.9	-1	5	3.2	5	3.1
MWIR2 cm:1	30	297	293	0.45	3.5	-0.36	3.5	-0.32	3.7	3	3.7	3
MWIR2 cm:2	38	293	292	0.48	1.9	-0.28	1.9	-0.28	4.1	3	4.1	2.9
MWIR2 cm:3	36	284	289	0.54	-4.3	-0.41	-4.4	-0.43	5.3	2.8	5.3	2.7
MWIR2 cm:4	8.2	269	282	0.58	-9	-1.3	-9.1	-1.3	5.5	3	5.4	3
wmc cm:1	32	294	294	2.7	0.1	-0.41	0.059	0.028	3.1	3	1.1	0.79
wmc cm:2	39	292	292	2.8	-0.14	-0.35	0.03	0.025	3	3	0.55	0.43
wmc cm:3	50	289	290	3	-0.19	-0.24	0.031	0.034	2.9	2.9	0.073	0.069
wmc cm:4	18	286	288	3	-0.32	-0.65	0.037	0.03	3.3	3.3	0.067	0.075
wmc MWIR2 cm:1	32	295	294	1.8	1.5	-0.41	1.8	-0.29	3.2	3	2.5	2.7
wmc MWIR2 cm:2	39	293	292	1.9	1.1	-0.35	1.5	-0.12	3.1	3	2.5	2.6
wmc MWIR2 cm:3	50	290	290	2	0.089	-0.24	0.73	0.28	2.7	2.9	2.3	2.4
wmc MWIR2 cm:4	18	287	288	2.1	-0.53	-0.66	-0.094	-0.23	3	3.3	2.5	2.6
Cld2 cm:1	31	298	294	0.93	4.3	-0.39	4.2	-0.48	3.9	3	3.7	2.7
Cld2 cm:2	39	295	292	1	3.3	-0.34	3.1	-0.43	4.3	3	4	2.7
Cld2 cm:3	49	290	290	1.2	0.33	-0.27	0.22	-0.32	5	3	4.7	2.5
Cld2 cm:4	18	285	288	2.1	-1.4	-0.65	-0.75	-0.054	4.4	3.3	3.2	1.6
MWIR2 Cld2 cm:1	30	298	293	0.76	4.1	-0.4	4.1	-0.35	3.8	3	3.7	2.8
MWIR2 Cld2 cm:2	38	295	292	0.85	3.2	-0.32	3.2	-0.26	4.3	3	4.1	2.7
MWIR2 Cld2 cm:3	48	291	290	1	0.54	-0.28	0.76	-0.14	4	2.9	3.8	2.6
MWIR2 Cld2 cm:4	18	286	287	1.6	-1.1	-0.66	-0.84	-0.41	3.6	3.3	3.2	2.7
AP=Cli Cld2 cm:1	31	299	294	1.4	4.7	-0.4	4.9	-0.22	4.1	3	4.1	3
AP=Cli Cld2 cm:2	39	296	292	1.5	3.8	-0.35	3.9	-0.2	4.7	3	4.8	3.1
AP=Cli Cld2 cm:3	49	290	290	1.7	-0.088	-0.27	-0.22	-0.34	6.5	3	6.5	2.9
AP=Cli Cld2 cm:4	18	281	288	3.7	-3.3	-0.66	-3.8	-1.4	6.4	3.3	5.8	3.4
AP=Cli MWIR2 Cld2 cm:1	31	298	294	0.9	4.3	-0.4	4.4	-0.33	3.8	3	3.9	3
AP=Cli MWIR2 Cld2 cm:2	39	296	292	1	3.5	-0.33	3.5	-0.24	4.3	3	4.4	3
AP=Cli MWIR2 Cld2 cm:3	48	291	290	1.2	0.89	-0.27	0.88	-0.31	4.8	2.9	4.8	2.9
AP=Cli MWIR2 Cld2 cm:4	18	286	288	2.5	-0.97	-0.66	-1.2	-0.93	4.4	3.3	4.4	3.3

Surface Temperature / K ; day land; 20130417; BC; Emis:20n; asc  
23.07 Z/01/15.

Figure 6-14: Summary table for surface temperature, comparing different options to deal with cloud. Top row in table shows results for the standard IR only scheme (in cloud-free scenes). Then rows show, divided by cloudiness flag value ("cm:x", where x=1-4), results from different retrieval options (all of which include fitting of emissivity and bias correction parameters), as follows: IR only scheme; MWIR scheme, IR only scheme with McNally Watts, MWIR scheme with McNally Watts; IR only with cloud retrieval; MWIR with cloud retrieval; IR only with cloud retrieval, starting from climatological prior; MWIR with cloud retrieval, starting from Climatological prior. Column headings are defined in the text.

## 7 TASK 6: RETRIEVALS WITH ONE OR MORE MISSING AMSU CHANNELS

In this task, the OEM using IASI, MHS and AMSU data in synergy is applied under the assumption that certain AMSU channels are missing. This analysis is motivated by the failure of channel 7 on the Metop-A instrument, and the increasing noise levels in channels 3 and 8. Channels are effectively omitted from the retrieval by setting the corresponding measurement errors in the OEM to very large values. Two particular configurations are studied:

- Without AMSU channel 7.
- Without AMSU channels 3,7,8.

The information loss is assessed for Metop-B so that results can be compared to the case with all channels present.

For the assessment in this task the following configuration of the retrieval scheme is considered as the baseline:

- MW+IR channels are used.
- PWLR is used as a priori (as in the Eumetsat OEM)
- IR bias correction scale parameters are retrieved.
- Emissivity is retrieved; 20 patterns are fit, with correlations between MWIR and IR channels.
- The MW bias correction and covariance derived from observation/model statistics over sea are used over both land and sea (under the assumption that the larger errors and different bias found over land are accommodated by the emissivity retrieval).
- Cloud fraction and height are retrieved, as described in section 6.2.

The impact of excluding channels is mainly considered for relatively cloud-free scenes, identified by L2 cloudiness flag 1 or 2.

## 7.1 LINEAR SIMULATIONS

Linear retrieval simulations indicating the potential loss of information associated with the missing channels are illustrated in section 6 of the plot annex. As might be expected, changes mostly affect temperature. Changes to the degrees of freedom for signal for the example scenes are summarised in Table 4. Omission of channel 7 has a very small effect. Omitting channels 3,7,8 lead to the loss of half a degree of freedom for the MW only retrieval, though only around 0.2 in the joint retrieval. Changes to the estimated errors on retrieved profiles are also small (as shown by the figures in the annex).

	MWIR			MW only		
	All channels	Excluding channel 7	Excluding channels 3,7,8	All Channels	Excluding channel 7	Excluding channels 3,7,8
<b>Mid-latitude land</b>	8.25	8.22	8.05	5.82	5.74	5.22
<b>Tropical land</b>	8.93	8.91	8.78	6.09	6.01	5.46
<b>Mid-latitude ocean</b>	8.68	8.65	8.52	6.25	6.17	5.68
<b>Tropical ocean</b>	9.10	9.08	8.94	6.37	6.27	5.73

**Table 4: Changes to degrees of freedom for signal for temperature as certain channels are excluded.**

## 7.2 GLOBAL RETRIEVALS

Results from three version of the MWIR retrieval, applied to Metop-B data on 17 October 2013, are shown in section 12 of the plot annex. Three versions of the MWIR scheme are shown: (i) with PWLR as prior, cloud parameters are not retrieved; (ii) with PWLR, cloud parameters retrieved; (iii) climatological prior constraint, cloud parameters retrieved. The third case would be expected to reveal most impact from the missing channels. (Channels which are omitted from the OEM may still contribute information via the PWLR when it is use as prior). Results from this case, considering missing channels 3,7,8 are summarised in Figure 7-1. This shows, for the 0-2, 0-6 and 6-12km layers, gridded differences between the retrieval with missing channels and that with all channels, side-by-side with the difference between retrieval and analysis (for the case with missing channels). It is clear that the differences are very small, compared to the differences between the retrievals and analysis (or estimated errors in retrieved quantites). E.g. the standard deviations in the global differences are around 0.1K for temperature and 0.5% for water vapour. Differences introduced by omitting only channel 7 are much smaller still.

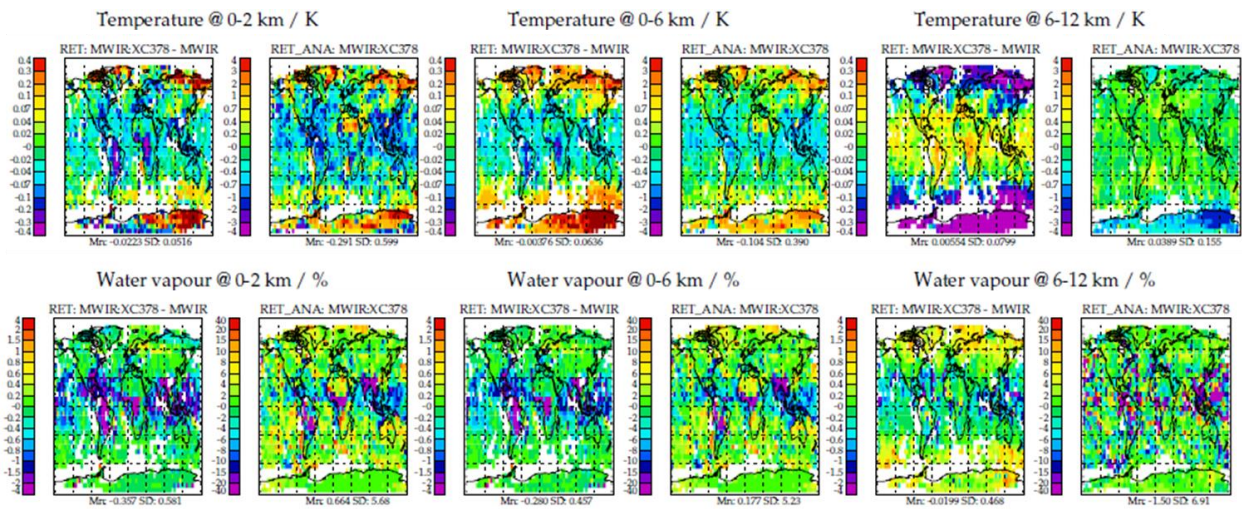


Figure 7-1: Comparison of Metop-B retrieval results with missing AMSU channels 3,7,8 to retrievals with all channels. Top row shows results for temperature; bottom row shows results for water vapour. Panels are shown in pairs for three layers (0-2, 0-6, 6-12km). In each pair, the left hand panel shows the difference between retrievals with channels 3,7,8 missing compared to those with all channels; the right hand panel shows the difference between retrieval and analysis, for comparison (though note the much larger range of the colour scale). Values under each panel indicate the mean (Mn) and standard deviation (SD) of the gridded values shown.

### 7.3 COMPARISON OF METOP-A AND METOP-B RETRIEVALS

In this task, the retrieval scheme was also applied to process data from Metop-A (for which AMSU channel 7 is not available). Results from Metop-A and Metop-B are then compared to establish their consistency. A set of results, for the three retrieval configurations discussed in the previous section, is presented in section 13 of the plot annex. Two days of Metop-A data were provided for analysis by Eumetsat: 23 March 2010 and 17 October 2013. The latter is also one of the days analysed for Metop-B, allowing nearly direct comparisons, though it should be noted that the orbit tracks of the two satellites are interleaved (~50 minutes out of phase).

Note, with the exception of channel 7, the same bias correction and measurement covariance are used for Metop-A and Metop-B. This is justified by plots presented in section 4.1 of the plot annex, which indicate similar observation-simulation departures for Metop-A (on both days) and Metop-B.

Figure 7-2 compares the Metop-A and Metop-B retrievals on the 17 October 2013. Differences in temperature are small (mean difference < 0.1K and standard deviation over the globe < 0.7K); Differences in humidity over the globe are around 5-10% which is comparable to or slightly smaller than the differences between retrieval and analysis and the ESD on individual retrievals.

The scheme has also been applied to Metop-A data on 23 March 2010. On this date it is noted that the Eumetsat cloudiness flag does not appear to detect cloud with the same efficiency as it does on other days. E.g. plots in the annex indicate the average Eumetsat cloud fraction in scenes with cloudiness flag 1 or 2 to be unusually high on this day, and the number of scenes with cloudiness flag 1 or 2 is also much larger. For this reason results for 23 March 2010 are presented (in the plot annex)

for scenes with cloudiness flag 1 or 2, and cloud fraction less than 0.1. This yields retrieval performance of broadly comparable, but still slightly degraded, quality compared to Metop-B and Metop A on 17 October 2013. The cost for MWIR (not IR-only) remains slightly higher than is the case for Metop-A or B in 2013, even when cloud is fitted. This probably indicates that the bias correction and/or measurement covariance used for Metop-A in 2010 underestimates actual errors.

It is also noted that on 23 March 2010, a region of relatively high cost is seen off the coast of North Africa, presumably caused by the presence of desert dust, which is clearly not fit well by the OEM, even when cloud and emissivity are included in the state vector.

Despite these anomalies with Metop-A data on 23 March 2010, we see no reason to suspect that the extended OEM should not be equally applicable to Metop-A and B, once issues associated with the cloudiness flag are addressed and more careful attention is given to temporal variations in the MWIR instrument errors. Certainly, the absence of channel 7 on Metop A has negligible impact on the consistency between retrievals from the two platforms.

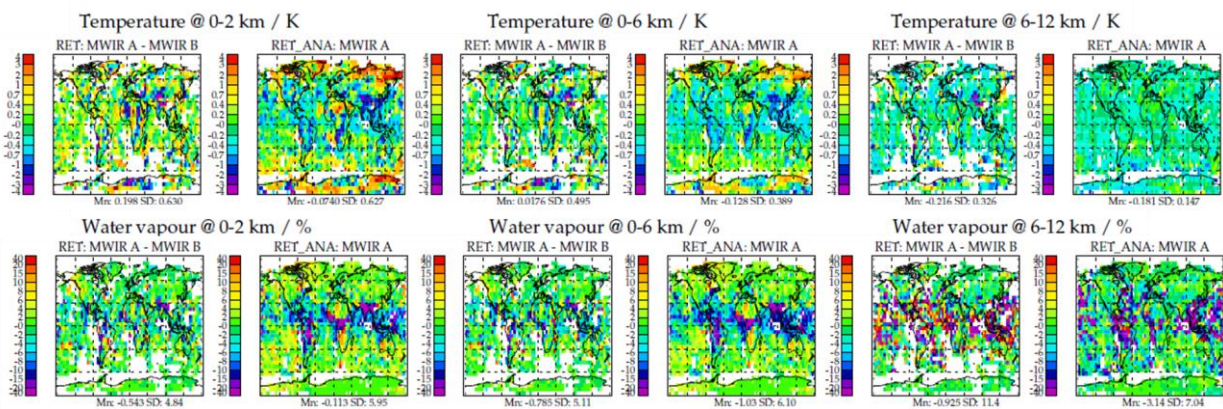


Figure 7-2: Comparison of Metop A and Metop-B retrieval results on 17 October 2013. Top row shows results for temperature; bottom row shows results for water vapour. Panels are shown in pairs for three layers (0-2, 0-6, 6-12km). In each pair, the left hand panel shows the difference between the Metop A and Metop B results; the right hand panel shows the difference between retrieval and analysis, for Metop A (same colour scale). Values under each panel indicate the mean (Mn) and standard deviation (SD) of the gridded values shown.

## 8 CONCLUSIONS

### 8.1 SUMMARY AND CONCLUSIONS

This study has explored the potential to improve on the operational IASI optimal estimation method (OEM) based retrieval by including information of the microwave sounders AMSU-A and MHS. This involved implementing the operational OEM at RAL and assessing its performance by comparison to ECMWF analyses, before proceeding to assess improvement to the scheme.

Measurement errors for the MW channels have been determined by computing observation – simulation statistics, based on using the IR only retrievals, together with RTTOV. This has resulted in a specification of the MW errors which seems quite consistent with those currently used in NWP and elsewhere reported in the literature.

The study has found that the Eumetsat OEM, and the piece-wise linear retrieval (PWLR) which is used as its prior, perform well in cloud free scenes over both ocean and land. The study extended the scheme to include the fitting of spectral emissivity and this was found to clearly improve retrievals in terms of cost (fit to measurements), and the agreement of lower tropospheric water vapour over land. The performance of the OEM for ozone was also improved over desert surfaces. The existing IR bias correction scheme was modified to include the retrieval of scale factors for the two bias correction spectra, leading to better fit costs over cold scenes in particular.

The scheme was also extended to analyse cloudy scenes, using either joint retrieval of cloud parameters or the McNally/Watts approach to select cloud-unaffected spectral channels. With either approach the coverage of the OEM can be increased to a much larger number of partially cloudy scenes, though it would appear that the retrieval of cloud retains more information on the atmospheric state.

The addition of the MW channels was found to have little impact (positive or negative) on the comparisons with analyses in cloud-free scenes (despite the potential for some gain in information being identified). However the benefit of using the MW instruments was quite clear in cloudy scenes. The impact of the missing AMSU channel 7 on the retrieval performance was found to be negligible. The absence (or degradation) of channels 3,7 and 8 is also considered to be small.

On the basis of the study findings it seems clear to recommend that the operational OEM should be extended to include fitting of spectral emissivity. The scheme could also be extended to treat cloudy scenes (with L2 cloudiness flag 3 and 4), by adding MW observations and at least using the WMC approach and possibly by the more ambitious approach of including cloud in the state vector, although it is recognised that both approaches would benefit from further optimisation (see below) prior to operational implementation.

It was found that the OEM could function quite well without the use of PWLR as the prior. Use of PWLR leads to slightly better results compared to the analyses, but the use of the climatological prior leads to results which are better represented by the associated reported errors and averaging kernels.

## 8.2 SUGGESTIONS FOR FURTHER WORK

The following points are identified for further work:

- The temperature, humidity and emissivity products by the PWLR and OEM, particularly after the extensions implemented in the study are clearly of very high quality. These products could potentially be used to improve trace gas retrievals from IASI. In particular, this potential has been recognised in a parallel study conducted by RAL to specify an OEM for methane retrievals from IASI. This scheme currently uses ECMWF analyses for temperature profiles and Wisconsin prescribed emissivity, and it is recognised that errors in these are limiting the quality of the methane retrieval in certain regions. The benefit of using the IASI(+MW) retrieved temperature and emissivity products in the methane scheme should certainly be tested. The same may be true for other trace-gas retrievals.
- Ozone is also retrieved by the OEM and the products have been compared to analyses in this study. However this is not an ideal basis for assessing the ozone as the analyses themselves (particularly in the troposphere) are of relatively poor quality, at least compared to the situation for temperature and humidity. It is also noted that comparison to analysis is particularly problematic in this case since (a) the PWLR is trained using the analysis and (b) the degrees of freedom for ozone are low, when PWLR is used as the prior constraint. The OEM is strongly constrained to PWLR, which in turn may follow spurious features of the analysis. There are indications that reasonable ozone profiles are retrieved when a relatively loose, climatological a priori is used in the OEM, indicating that the scheme is certainly capable of extracting useful ozone profile information. Obvious issues in the ozone profiles associated with arid-land surfaces are also strongly mitigated by the joint retrieval of surface spectral emissivity. It therefore seems appropriate to conduct further work to (a) optimise the prior constraint used for ozone, to avoid too much constraint to PWLR/analysis (b) test the quality of the derived profiles by comparison to independent measurements. In this case comparisons to ozone-sonde measurements over extended periods of time, complemented by intercomparisons with chemical transport model fields and / or MACC analyses, sampling the seasonal cycle, would be recommended, rather than focussing on individual days, as has proved effective for temperature and humidity.
- Although it is clear that joint retrieval of cloud improves retrievals in the presence of cloud, to the point where it makes sense to carry out the retrievals, it is also clear that product quality degrades with the amount and height of cloud. Further work would be required to establish appropriate quality control criteria for releasing profiles to users. Part of this may be to develop a proper error budget for cloudy scenes, e.g. by increasing measurement errors in cloudy scenes such that the errors reported by the OEM properly represent the differences between retrieved and true state. It is recognised however that this work would be complicated by the difficulty to unambiguously determine retrieval errors in cloudy scenes by comparison to analyses, which are themselves subject to error.
- The McNally/Watts scheme seems to provide retrievals which function in most scenes, however the cloud detection seems too conservative. If this scheme were to be implemented in practise, it would be desirable to refine the various tuning parameters to

optimise the information extracted. As a minimum the scheme should only be applied in scenes which are flagged as cloudy, as otherwise it degrades too strongly the performance in cloud-free scenes (i.e. those with cloudiness flag 1 or 2).

- The cloud model used in the retrievals is very simple. It neglects the effects of spectral structure in cloud optical properties (particularly important for ice cloud) and the effects of cloud vertical distribution on the radiative transfer. Although these effects are impossible to treat completely in a retrieval scheme of this kind, it seems probable that extending the cloud model to better represent these effects could further improve the trace-gas retrievals in currently difficult scenes. A next step would be to introduce a model for cloud which could represent the expected spectral variations in cloud optical properties, e.g. . Introducing a model like that used in Eumetsat OCA scheme and retrieving cloud phase/effective radius/optical depth/height may improve the performance of the scheme. This approach could be extended to also allow the model to represent optical properties of mineral dust aerosol, which has also been seen to affect retrievals (high cost function values caused by desert dust are seen off the coast of Africa in the Metop A results from 23 March 2010).
- The surface emissivity retrieval developed here is certainly effective, however residuals remain over arid regions, which are presumably caused by the absence of real emissivity spectral structure in the fitted patterns. Further work to study the spectral emissivity of these regions and improve the approach is needed.
- The study has only considered a few individual days. While it appears that IASI is extremely stable, it may well be that more effort is needed to deal with time dependent errors in the MW measurements. An analysis of the MWIR performance over an extended period of time should be carried out to assess the stability of the scheme and develop necessary long-term correction measures.

## 9 REFERENCES

- [Ref:1] IASI Level 1 PCC Product Generation Specification, EUM.OPS-EPS.SPE.08.0199
- [Ref:2] IASI Level 1 PCC Product Format Specification, EUM.OPS-EPS.SPE.08.0195
- [Ref:3] IASI Level 2 Product Guide, EUM/OPS-EPS/MAN/04/0033, v3B
- [Ref:4] Pre-processing of ATMS and CrIS, Section 4, NWPSAF-MO-UD-027
- [Ref:5] Hultberg and August, CANONICAL ANGLES BETWEEN THE IASI OBSERVATION AND FORWARD MODEL SUBSPACES
- [Ref:6] Hultberg and August, THE PIECEWISE LINEAR REGRESSION RETRIEVAL OF TEMPERATURE, HUMIDITY AND OZONE WITHIN THE EUMETSAT IASI L2 PPF VERSION 6
- [Ref:7] G. DESROZIERS, L. BERRE, B. CHAPNIK and P. POLI, Diagnosis of observation, background and analysis-error statistics in observation space, *Q. J. R. Meteorol. Soc.* (2005), 131, pp. 3385–3396, doi: 10.1256/qj.05.108
- [Ref:8] Niels Bormann\* and Peter Bauer, Estimates of spatial and interchannel observation-error characteristics for current sounder radiances for numerical weather prediction. I: Methods and application to ATOVS data, *Q. J. R. Meteorol. Soc.* 136: 1036–1050, April 2010 Part B.
- [Ref:9] Weston P P, W Bell and J R Eyre, 2013, Accounting for correlated error in the assimilation of high resolution sounders, Accepted by *Q J R Meteorol Soc.*, DOI: 10.1002/qj.2306.
- [Ref:10] Aires, F, C. Prigent, Frédéric Bernardo<sup>1</sup>, Carlos Jiménez<sup>2</sup>, Roger Saunders<sup>3</sup>,‡ and Pascal Brune: A Tool to Estimate Land-Surface Emissivities at Microwave frequencies (TELSEM) for use in numerical weather prediction, *Quarterly Journal of the Royal Meteorological Society*, Volume 137, Issue 656, pages 690–699, April 2011 Part A
- [Ref:11] Borbas, E. E. and B. C. Ruston, 2010. The RTTOV UWiremis IR land surface emissivity module. NWP SAF report. [http://research.metoffice.gov.uk/research/interproj/nwpsaf/vs\\_reports/nwpsaf-mo-vs-042.pdf](http://research.metoffice.gov.uk/research/interproj/nwpsaf/vs_reports/nwpsaf-mo-vs-042.pdf)
- [Ref:12] Karbou, F., E.Gérard, and F. Rabier, 2006, Microwave land emissivity and skin temperature for AMSU-A and –B assimilation over land, *Q. J. R. Meteorol.Soc.*, vol. 132, No. 620, Part A, pp. 2333–2355(23), doi :10.1256/qj.05.216
- [Ref:13] Liu, Q, F. Weng, S.J. English, An Improved Fast Microwave Water Emissivity Model, *IEEE Transactions on Geoscience and Remote Sensing* (Impact Factor: 3.47). 05/2011; DOI: 10.1109/TGRS.2010.2064779
- [Ref:14] McNally, A. P., Watts, P. D., A cloud detection algorithm for high-spectral-resolution infrared sounders, *Q. J. R. Meteorol. Soc.* (2003), **129**, pp. 3411–3423